AERODYNAMIC PERFORMANCE OF LOW ASPECT RATIO TURBINE BLADE IN THE PRESENCE OF PURGE FLOW

Thesis

Submitted in partial fulfillment of the requirements for the degree of

DOCTOR OF PHILOSOPHY

by

SUSHANLAL BABU

(ME15F14)

Under the Guidance of

Dr. ANISH S

Associate Professor

DEPARTMENT OF MECHANICAL ENGINEERING

NATIONAL INSTITUTE OF TECHNOLOGY KARNATAKA SURATHKAL, MANGALURU - 575025, INDIA

June 2021

DECLARATION
by the Ph D Reasearch Scholar

I hereby **declare** that the Research Thesis entitled **"Aerodynamic Performance of Low Aspect Ratio Turbine Blade in the Presence of Purge Flow"** which is being submitted to the **National Institute of Technology Karnataka, Surathkal** in partial fulfillment of the requirements for the award of the Degree of **Doctor of Philosophy** in **Mechanical Engineering** is a *bonafide report of the research work carried out by me*. The material contained in this Research Thesis has not been submitted to any University or Institution for the award of any degree.

Name of the Research Scholar: **SUSHANLAL BABU**
Register No.: **155047ME15F14**
Signature of Research Scholar:

Department of Mechanical Engineering

Place: NITK - Surathkal

Date: 11/06/2021

CERTIFICATE

This is to certify that the Research Thesis entitled **"Aerodynamic Performance of Low Aspect Ratio Turbine Blade in the Presence of Purge Flow"**, submitted by

Mr. SUSHANLAL BABU (Register Number: 155047ME15F14) as the record of the research work carried out by him, is *accepted* as the *Research Thesis submission* in partial fulfillment of the requirements for the award of degree of **Doctor of Philosophy**.

Dr. Anish S
Research Guide
Date: 8/10/2021

Chairman-DRPC
Date:

This thesis is
dedicated to
My beloved
Parents and family

ACKNOWLEDGEMENTS

ABSTRACT

In aero engines, purge flow is directly fed from the compressor which bypasses the combustion chamber and introduced into the disk space between blade rows to prevent the hot ingress. Higher quantity of purge gas fed through the disk space can provide additional thermal protection to passage endwall and blade surfaces. Moreover interaction of the purge air with the mainstream flow can alter the flow characteristics of turbine blade passage. The objective of the present investigation is to understand the secondary vortices and its aerodynamic behavior within a low aspect ratio turbine blade passage in the presence of purge flow. An attempt is made to understand the influence of velocity ratios and purge ejection angles on these secondary vortices. The objective is broadened by investigating the unsteadiness generated by upstream wakes over the secondary vortex formations in th presence of purge flow. Further the thesis aims to judge the feasibility of implementing endwall contouring to curb the additional losses generated by the purge flow. To accomplish these objectives, a combination of experimental measurements and computational simulations are executed on a common blade geometry. The most reliable commercial software ANSYS CFX which solves three dimensional Reynolds Averaged Navier Stokes Equations together with Shear Stress Transport (SST) turbulence model has been used to carry out computational simulations. Along with steady state analysis, in order to reveal the time dependent nature of the flow variables, transient analysis has been conducted for certain selected computational domains. The numerical results are validated with experimental measurements obtained at the blade exit region using five hole probe and Scanivalve. The experimental analysis is conducted for the base case without purge (BC) and base case with purge (BCp) configurations having flat endwalls.

In the present analysis, it is observed that with an increase in the velocity ratio, the mass averaged total pressure losses also increases. In an effort to reduce the losses, purge ejection angle is reduced to 35^0 from 90^0 with a step size of 15^0. Significant loss reduction and improved endwall protection are observed at lower ejection angles. Numerical investigation of upstream disturbances/wakes explore the interaction effects of two additional vortices, viz. the cylinder vortex (Vc) and the purge vortex (Vp). Steady state analysis shows an increase in the underturning at blade exit due to the squeezing of the pressure side leg of horseshoe vortex (PSL) towards the pressure surface by the cylinder vortices (Vp). The unsteady analysis reveals the formation of filament shaped wake structures which breaks into smaller vortical structures at the blade leading edge for stagnation wake configuration (STW). On the contrary, in midpassage wake configuration (MW), the obstruction created by the purge flow causes the upper portion of cylinder vortices bend forward, creating a shearing action along the spanwise direction. Investigation of contoured endwall geometries shows that, endwall curvature either accelerate or decelerate the flow thereby a control over the endwall static pressure can be obtained. Out of three contoured endwalls investigated, the stagnation zones generated at the contour valleys has resulted in the additional loss generation for the first two profiles. Reduced valley depth and optimum hump height of the third configuration has effectively redistributed the endwall static pressure. Moreover an increase in the static pressure distribution at the endwall near to pressure surface has eliminated the pressure side bubble formation. Computational results of URANS (Unsteady Reynolds Averaged Navier Stokes) simulations are obtained for analyzing transient behaviour of pressure side bubble, with more emphasis on its migration on pressure surface and across the blade passage.

TABLE OF CONTENTS

LIST OF TABLES

LIST OF FIGURES

xiv

xvii

NOMENCLATURE

$A1$ Attachment point

A_e Exit area of the coolant discarge pipe (m^2)

A_i Inlet area of orifice meter (m^2)

A_t Throat area of orifice meter (m^2)

C_{ax} Axial chord (m)

C_b Blade loading coefficient

C_{po} Total pressure loss coefficient

C_{ps} Static pressure coefficient

C_p Total pressure coefficient

M Velocity ratio

m_∞ Mainstream mass flow rate (kg/s)

m_c Coolant mass flow rate (kg/s)

P_s Static pressure (Pa)

P_t Total Pressure (Pa)

$P_{t\infty}$ Total pressure at mainstream inlet (Pa)

P_{tc} Total pressure at coolant inlet (Pa)

R Reattachment point

S Separation point

$S1$ Saddle point

T_c Coolant inlet temperature (K)

T_∞ Mainstream inlet temperature (K)

T_{aw} Adeabatic wall temperature (K)

U Mainstream inlet average velocity (m/s)

u Axial velocity component (m/s)

U_c Coolant inlet average velocity (m/s)

v Tangential velocity component (m/s)

w Radial velocity component (m/s)

x Axial distance (m)

y   Pitchwise distance (m)

z   Spanwise distance (m)

Greek Symbols

$=$ Mass averaged

$^-$ Pitch averaged

β Exit yaw angle (degree)

Δ Uncertainty

δ^* Displacement thickness (m)

η Film cooling effectiveness

μ_t Turbulent dynamic viscosity (Pa s)

ν_t Turbulent kinematic viscosity (m^2/s)

τ Non-dimensionalized time

τ_{ij} Principal turbelent shear stress (Nm^{-2})

θ^* Momentum thickness (m)

Subscripts

∞ Mainstream

1   Inlet

2   Outlet

aw   Adeabatic wall

c   Coolant

d   Diverted

i   Induced

Abbreviation

AC   Alternate current

BC   Base case

BCp   Base case with purge

BFR   Bleed flow ratio

BLc   Boundary layer cross flow

CSKE Coefficient of secondary kinetic energy

CV   Counter vortex

D   Distance between blade and purge slot (m)

DR   Density ratio

EC1   Endwall contour 1 (without purge)

EC1p Endwall contour 1 (with purge)

EC2   Endwall contour 2 (without purge)

EC2p Endwall contour 2 (with purge)

EC3   Endwall contour 3 (without purge)

EC3p Endwall contour 3 (with purge)

FCE   Film cooling effectiveness

HP   Horse power

HPT   High pressure turbine

HSV   Horseshoe vortex

L   Length of the purge slot (m)

LE   Leading edge

LPT   Low pressure turbine

MW   Midpassage wake

PR   Pressure ratio

PS   Pressure side

PSB   Pressure side bubble

PScv   Pressure side corner vortex

PSL   Pressure side leg of HSV

PSLd   Diverted pressure side leg vortex

PSLi   Vortex induced by the PSLd

PSv   Pressure surface vortex

PSW   Pressure side wake

PV   Passage vortex

RPM   Revolution per minute

SS   Suction side

SScv   Suction side corner vortex

SSL   Suction side leg of HSV

SSW   Suction side wake

STW   Stagnation wake

TCF   Turbine centre frame

TE   Trailing edge

TEcv   Trailing edge-endwall corner vortex

TFV   Trailing edge filament vortex

TKE   Turbulent kinetic energy (J/kg)

TSV   Trailing edge shed vortex

Vc   Cylinder vortex

VFD   Variable frequency drive

Vp   Purge vortex

W   Width of the purge slot (m)

CHAPTER 1

INTRODUCTION

1.1   Gas turbines

The human being has been intrigued by the idea of flight from ancient time. This dream has been fulfilled through the invention of jet engine. Nowadays flying is a common mode of transport and is used annually by billions of people. A steady rise in the price of oil in recent decades, directly affects the operating costs of aircrafts. In the last decades, more restrictive emission standards have been introduced to control or at least reduce the ecological consequences of the rise in air contamination specifically nitrogen oxide (NOx) emission due to the frequently increasing worldwide air traffic. One major contributing factor to this advancement was the production of more powerful at the same time environment friendly jet engines.

Gas turbine designers continuously aim for greater performance while ensuring engine reliability without sacrificing manufacturing cost. Though overall thermal efficiencies have improved considerably in industrial applications of gas turbines in recent years, the already highly efficient jet engines used in the aviation industry have shown modest gains. Industrial systems have the benefit of recovering vast quantities of waste heat for co-generation or combined cycle use. Also, they are not constrained by size and weight restrictions, thereby enabling the use of extensive inter-cooling and thermal regenerative cycles. On the other hand, restrictions on both weight and size made the jet engine designers to develop compressors and turbines of relatively high thermal efficiencies.

For this, optimized operating components and advanced combustion technologies were designed for the engines with broad bypass ratios. In addition, the engine's ther-

modynamic efficiency was improved, either by increasing turbine inlet temperatures or by increasing compressor's overall pressure ratio (PR). This has led to temperature of turbine inlets far beyond the melting point of the various turbine components. Additionally, high temperature gas from the combustion chamber can also cause serious damage to engine. In the process of rising inlet temperatures in gas turbines for better efficiency gains, components must be protected from overheating by providing additional efficient cooling techniques.

One of the regions that can be gravely affected by the hot gas is the surface of the turbine disk which holds the stator and rotor blades. The exposure of these components to hot ingress can reduce their material properties and durability. The probable ingress can be counteracted by incorporating two methods: the installation of rim seals and the supply of purge air. However while designing the rim seal, it should be recalled that, thermal expansion coefficient exhibited by the materials used for the manufacturing of various components are different and depending on the frequently changing thermal conditions, the expansion rate can also be different. Hence the safe handling and operation of the engine, this rim seal has to maintain optimal clearance between rotor and stator disk. However hot ingress can takes place through this optimum clearance. For instance, space between rotating and stationary components are purged with cold air directly fed from the compressor to prevent hot gas from entering the wheelspace.

1.2   Flow behaviour in turbine blade passage

In axial gas turbines losses can be classified as frictional losses, secondary losses, tip leakage losses, cooling losses and blockage losses (Hennecke and Wörrlein (2000)). Viscous force and pressure induced forces are the two major factors responsible for these losses. According to Thole (2006), secondary losses generated within the first stage itself corresponds to 30% of the total pressure loss generated through a whole turbine stage. Because of this major impact on total losses, secondary flows have been given great importance in the gas turbine production. Ingram (2004) describes sec-

ondary flow as a minor disruption to a primary flow where the primary flow is the main two-dimensional flow. Secondary flow can also be defined as the flow which is deflected away from the primary flow and possess three dimensional nature under the influence of inlet boundary layer (Figure1.1). In the following section detailed explanation of three primary vortex structures (horseshoe vortex. passage vortex and induced vortices) and its development are discussed.
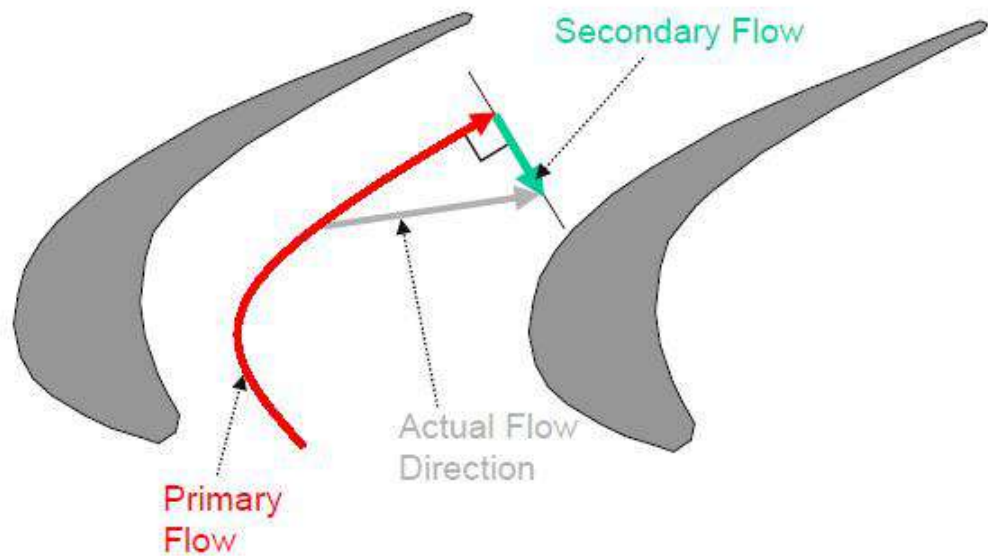
Figure 1.1: Simple definition of secondary flow (Ingram 2004).

1.2.1   Horseshoe Vortex

Strong cross flow and transverse pressure gradient dominates the hub endwall region of the blade passage. The resulting endwall flow field is complex and features strong secondary flows and roll-up vortices. The streamline distribution just above the endwall shown in Figure 1.2 reveals some salient characteristics of the incoming endwall boundary layer. These characteristic features are distinguished from one another with the help of zero incidence line and separation lines. When the zero incidence line reaches the saddle point, it bifurcates and separation lines are formed. Saddle point is the location which represents least frictional velocity and highest total pressure. Simultaneously when the free stream approaches the blade leading edge the static pressure increases in

the direction away from the endwall and normal to the free stream flow. Static pressure generated by the free stream will be higher than that generated by the boundary layer fluid because of the velocity deficit developed due the viscous effect. Under the influence of this radial pressure gradient, vortex rolls are generated at the leading edge - endwall junction. This vortex is called as horseshoe vortex (HSV). The horseshoe vortex splits across the leading edge and propagates downstream of the blade passage. The branch which deflect towards the pressure side is named as pressure side leg vortex (PSL) and that which flows along suction surface is named as suction side leg vortex (SSL). Both legs have sense of rotation opposite to each other. The dominant boundary layer pitch wise pressure gradient drives the pressure side leg from the leading edge to neighboring blade suction side. The suction side leg remains close to the suction surface along the separation line as observed in Figure 1.2. As both vortex legs propagates downstream of the blade passage, they merge together to form a single vortex structure named passage vortex (PV) with sense of rotation similar to pressure side leg vortex. Until merging, both legs of horseshoe vortex remains close to the hub endwall.

1.2.2   Passage Vortex

The single vortex structure formed by the merging of both legs of horseshoe vortex, approximately half way downstream of the blade passage is termed as passage vortex. As the direction of passage cross flow is from pressure side to suction side, the strength of pressure side leg is higher than suction side leg vortex. After the merging of both legs, the passage vortex also inherit the same rotational direction as that of stronger pressure side leg vortex. During its course towards the blade exit region, the size of the passage vortex gradually increases and shift upwards under the action of spanwise pressure gradient present within the suction surface boundary layer. The movement of passage vortex away from the endwall tempts the endwall boundary layer to rise upwards along the suction surface and wraps around the passage vortex. As a result close to the suction surface, the endwall boundary layer gets skewed and becomes thicker. Another key observation made by (Acharya and Mahmood 2006) is the wrapping behavior of suction

4
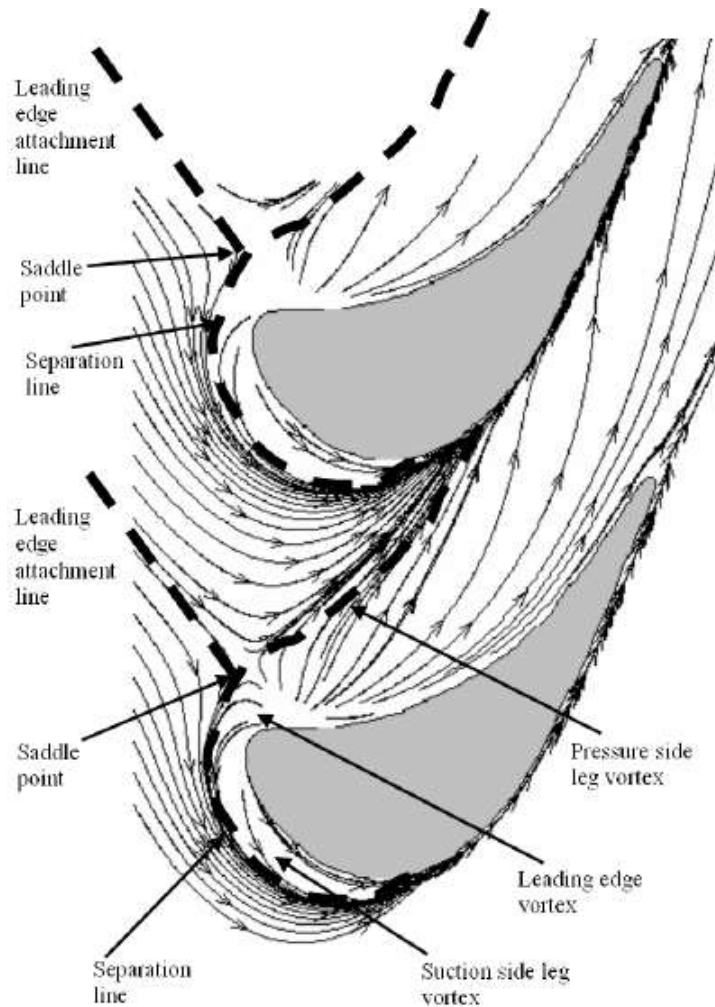
Figure 1.2: Endwall streamlines showing separation lines and horseshoe vortex legs (Acharya and Mahmood 2006).

side leg around the passage vortex. The suction side leg vortex which was observed just above the passage vortex at the location of merging seems positioned at bottom of the same at the passage exit region. This was earlier confirmed by (Wang *et al.* 1995) with the help of laser light sheet technique (Figure 1.3).

1.2.3 Induced Vortices

Experimental analysis conducted by Wang *et al.* (1995) within a linear turbine cascade using smoke trails illuminated by laser light sheet has obtained a clear picture of different induced vortices. The vortex which is induced by the passage vortex is named
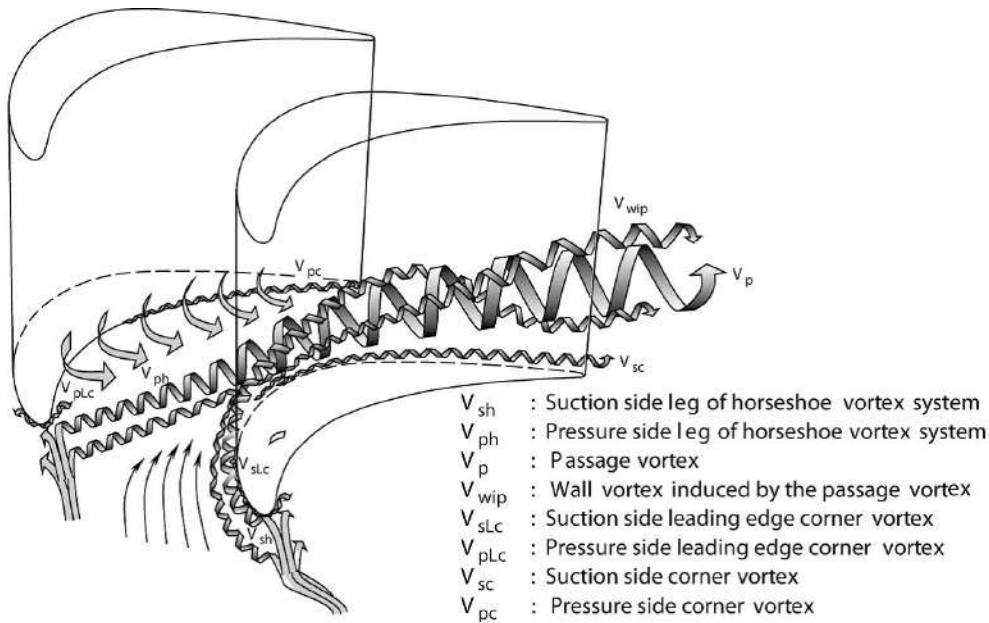
Figure 1.3: Secondary Flow Structures by Wang *et al.* (1995).

as wall vortex (WV). Like suction side leg vortex, it will not wrap around the passage vortex, rather it remains close to the suction surface above the passage vortex till blade trailing edge. Once it exits the blade trailing edge it tends to move with the passage vortex and later merges with the trailing edge wake region. It has the rotational sense opposite to that of passage vortex. At the leading edge-endwall junction, horseshoe vortex has induced small corner vortices which travel along the pressure and suction side. Wang *et al.* (1995) has named both vortices as pressure side leading edge vortex and suction side leading edge vortex. Furthermore, two additional corner vortices are identified at the junction of both pressure side and suction side with the endwall. They are named as pressure side corner vortex and suction side corner vortex. Both vortices possess rotational direction same as that of suction side leg of horse shoe vortex.

1.3   Secondary flow control techniques

The secondary vortices are the major cause of aerodynamic losses. Existence of passage vortex plays an important role in the non-uniform distribution of exit flow angles and it can significantly alter the flow aerodynamics of the subsequent blade rows. So in

recent years, the researchers as well as turbine engine designers have applied so much efforts to develop various active and passive techniques to cut down the secondary flow losses within a blade passage. In active techniques, control over secondary vortices are achieved either by momentum addition or momentum subtraction within the endwall or blade surface boundary layers. Usually active techniques have limited benefits. Investigation made by Sturm *et al.* (1992) and Biesinger (1993) on boundary layer blowing has exhibited limited mixed loss reduction. However Behr *et al.* (2008) achieved a considerable tip leakage loss reduction through a controlled coolant ejection from the turbine casing. The advantages of active flow control technique like tip injection is that it can easily adjust with the actual flow and significantly reduce the tip leakage losses (Christophel *et al.* 2005; Hamik and Willinger 2007; Li *et al.* 2008). Similarly the application of same cold air injection technique over the hub endwall through tiny holes is far more challenging because of the existence of endwall secondary flow structures. The coolant injecting out of the holes located upstream and close to the separation line have the tendency to lift off with the secondary vortices, leaving the endwall exposed to the hot gas (Acharya and Mahmood 2006). Therefore the researchers and designers are more interested in developing effective passive techniques which can effectively mitigate secondary flow structures and subsequent losses without any additional power input. Examples of such passive techniques are leading edge modifications, leading edge filleting, boundary layer fencing and endwall contouring.

1.3.1 Blade profile modifications

Harrison (1990) demonstrated the influence of three dimensional blade profile modification on secondary loss generation. He investigated three set of leaned blade: first one, unleaned: second simple leaned and third compound leaned (bowed with convex pressure side and concave suction side). The inference made was, simple lean structure did not exhibit any net gain because when loss reduction was observed at one endwall, the same increased at the opposite endwall. The compound lean structure exhibited endwall secondary loss reduction but it was compensated by the increase in the midspan

profile losses. However the compound lean structure has made the exit flow angle more uniform which substantially improved the flow aerodynamics of the succeeding blade rows. Han *et al.* (2002) compared the performance of three blade profiles: conventional straight, positively curved, negatively curved with various tip clearances, on the vortex formations at the blade tip as well as suction side corner. The conclusion made was, with the increase in the relative tip clearance, more interaction between tip leakage vortex and upper passage vortex happens and leads to higher energy losses. Reverse compound lean blade structure similar to negatively curved design, analyzed by Bagshaw *et al.* (2005) obtained an overall loss reduction of 11%. However non uniformity observed in exit yaw angle distribution for the compound lean design may lead to downstream mixing loss enhancement. DIppolito *et al.* (2011) analyzed the sensitivity of blade lean angle on secondary vortex formations and loss generation with the help of both straight and annular cascade. Recently Giovannini *et al.* (2019) has introduced a novel profile modification at blade endwall region which opposes the exit angular deviation and there by generating more uniform exit flow angle without much aerodynamic penalty.

1.3.2 Leading edge modification

The objective of leading edge modification is to control or curb the horseshoe vortex formation by adding fillet or bulb designs at leading edge-endwall corner. Several literatures have proposed different fillet designs with varying thickness (Becz *et al.* 2003, 2004). Thickness of the fillet gradually reduced to the minimum, once it merges either with the endwall or with the blade surface or with endwall-blade surface corner when it extends within the passage. The maximum height of the fillet is determined with respect to the incoming boundary layer thickness. The aim of fillet bulb profile proposed by Sauer *et al.* (2001) was to obstruct the direct impingement of pressure side leg of horseshoe vortex by strengthening the suction side leg vortex. With the help of laser doppler velocitymetry, Zess and Thole (2002) has explained the effective elimination of horseshoe vortex by leading edge fillet. Similarly weakening of passage vortex and

8

related total pressure loss reduction by leading edge fillet are put forward by Mahmood *et al.* (2005). Mank *et al.* (2014) noticed an increase of secondary losses by 10% and radial migration of passage vortex by 2.5% of span when the fillet of radius 16% of axial chord is imposed around the blade. They suggested that over all performance could be improved by adjusting the pitch spacing to adapt fillets of different radii.

1.3.3 Boundary layer fence

Fences are installed to control the trajectory of secondary flow structures so that its strength and related losses can be reduced. Kawai (1994) has used boundary layer fence on both endwall and blade surfaces and achieved a considerable reduction in the passage mass averaged losses. Moon and Koh (2001) analyzed effects of endwall fence of varying height on secondary loss reduction. He suggested, inlet boundary layer thickness as characteristic length for determining the fence height. Investigation made by Govardhan and Maharia (2012) stated that, maximum secondary loss reduction can be obtained by the fence of height, one third of inlet boundary layer thickness. Chung *et al.* (1991) reported improved cooling performance and reduced secondary losses within a cascade equipped with triangular endwall fence. Further investigation conducted by Chung and Simon (1993) concluded that at high free stream turbulence levels, fence is capable of reducing the passage vortex strength. Camci and Rizzo (2002) analyzed the endwall heat transfer and aerodynamic performance of different endwall fences within a 90^0 turning square duct. Throughout the turning duct all fence configurations achieved endwall heat transfer enhancement. Half height fence has produced pair of counter rotating vortices while full height fences which acts as blades, generates two separate passage vortices near the endwall. Some of the researchers have used the fence in steam turbines and axial fan casing to breakdown the secondary flow vortices. Han *et al.* (2019) investigated the effects of heating intensity and position of endwall fences over the aerodynamic performance of the cascade. At lower heating intensity, aerodynamic performances of all fence cases are better compared to base case whereas at higher heating intensity the formation of trailing edge shock waves by steam congestion deteriorates

the overall aerodynamic performance.

1.3.4   Endwall contouring

Instead of flat surfaces, in contoured cases, the solid endwall surfaces are comprised of curvatures of different heights. The intention behind the curvatures is to control the secondary vortex formations through locally accelerating or decelerating the boundary layer fluid while flowing over the combination of hump and valleys respectively. Depending on the surface curvature, endwall contouring can be categorized as axisymmetric and non-axisymmetric. In axisymmetric endwall contouring, the surface curvature will be symmetric with respect to the axial direction. The "Russian Kink" model, in which the annulus seems converged from leading edge to trailing edge, was the one recognized as the first axisymmetric endwall design. The investigation of this model by Deich *et al.* (1965) and Warner and Tran (1987) explored the concept "turn then accelerate" meaning, reduced velocity at higher turnings and then accelerate towards the trailing edge. Since then many researchers have suggested various axisymmetric endwall models with different success rates (Kopper *et al.* 1981; Boyle and Haas 1982; Moustapha and Williamson 1986).

On the contrary, for non-axisymmetric endwall contouring in both pitchwise and axial direction, the curvature height variation can be observed. The main objective of streamline curvature is to locally accelerate or decelerate the flow where ever required. For example by providing a hump region close to the pressure surface the local static pressure distribution can be reduced by locally accelerating the flow. Similarly within the valley region, the velocity reduces and static pressure increases and a uniform pressure distribution can be obtained all over the endwall. As a result the boundary layer cross flow will be reduced. Detailed literature review of various non-axisymmetric endwall models tested are explained in the chapter 2.

1.4 Purge flow

A section of the turbine which illustrates the wheelspace is shown in Figure 1.4. Wheelspace is the region enclosed by rotor discs and stationary parts beneath the stator vane. The interstage seals which separate different wheelspaces, restricts the purge flow that bypasses the main annulus underneath the stationary disk. The seal gap between the rotor and stator platform is essential for the smooth rotation of rotor blades.
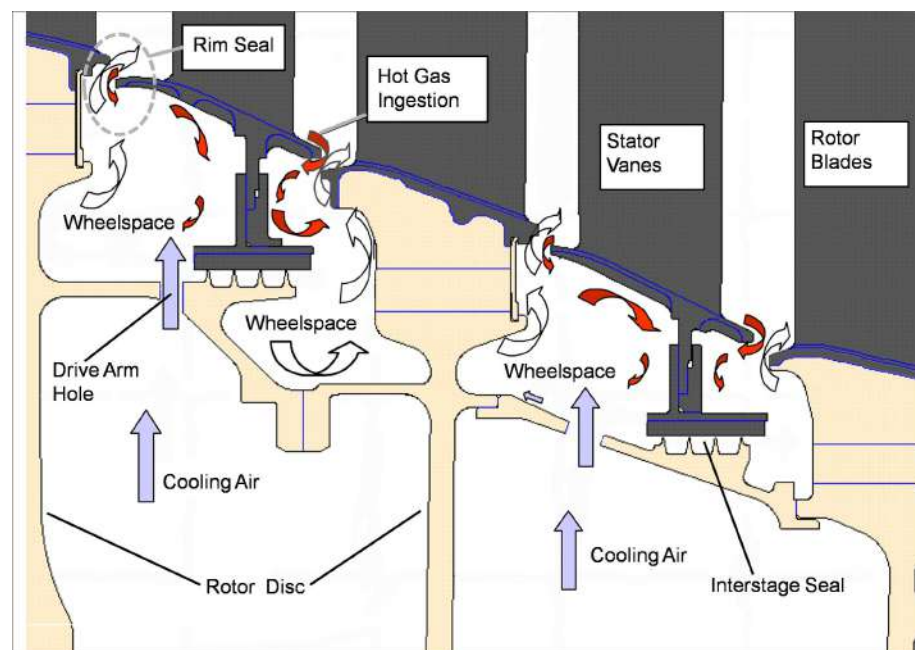
Figure 1.4: Illustration of a rotor-stator wheelspace with adjacent blades; adapted from Dixon *et al.* (2012).

Through the seal gap hot ingress will takes place. To restrict the hot ingress, compressor bleed air is directly fed through the wheelspace. Quantity of this bypassed purge air should be minimized since the interaction of purge flow with the secondary flow vortex structures of the subsequent blade rows can cause detrimental effects on the turbine efficiency. When the purge flow re-enters the main annulus, it interacts with the incoming hot mainstream flow. This changed the endwall boundary layer aerodynamics and usually results in increased secondary losses. Furthermore, additional quantity of purge air used obviously caused increase in the overall weight of the engine. This

scenario is more reflective in aviation industry where the additional weight of the excess fuel burned can have deleterious effects on the turbine efficiency enhancement. One possible way to overcome this situation is to reduce the number of engine components. Reduction in the number of turbine stages or number of blades in each row will leads to continuous increase of blade loading and lift coefficients. However, increase in the blade loading has disadvantages. Usually the increased loading is followed by increased secondary flow losses. The three dimensional complex boundary layer flow close to the endwall are responsible for these losses. Although a decline in purge flow is often needed, there is a threshold in general, as the purge flow is often used to protect the engine components from hot mainstream flow. As a result deep knowledge of the flow mechanisms within the blade passage is crucial to optimize the required quantity of purge flow and its detrimental consequences on the main flow aerodynamics. Hence, methods for minimizing secondary losses are therefore of great importance for enhancing aerodynamic and thermal efficiency of turbine. The research carried out here concentrate on the secondary flow inside the high pressure turbine (HP). HP turbines are exposed to full burden of hot high pressure gas ejecting out of combustion chamber, expanding at relatively high Mach number. Additionally, because HP turbines have relatively lower aspect ratios than low pressure (LP) turbines, the impact of secondary flow losses are greater than LP turbines. Of this reason, several studies on the injection of purge flow have been carried out over the last decades. While some consequences are well explained, however, others still need more special consideration to gather further information. This report provides a detailed literature review on this topic and illustrates several effects which are stimulated by injection of purge flow.

CHAPTER 2

LITERATURE REVIEW

2.1 The secondary flow structure in turbine blade passage

In a low aspect ratio turbine blade profile, secondary flow losses comprises of 30% to 50% of total aerodynamic losses (Sharma and Butler 1987). Sieverding (1985) and Langston (2001) provide detailed overviews of these secondary flow structures. These two literatures revealed the basics of three-dimensional nature of secondary flow structures, especially leading edge horseshoe vortex and the importance of viscous effects within the turbine blade passages. Langston (2001) outlined horseshoe vortex (HSV) formation and its separation into pressure side (PSL) and suction side legs (SSL) between leading edge and saddle point. Due to the separation, normal vorticity processed by the incoming mainstream was transformed into streamwise vorticity with in the blade passage. The pressure side leg was traversed across the blade passage under the influence of cross passage pressure gradient. The location at which the pressure side leg meets the suction side leg of adjacent blade was considered as the point of formation of passage vortex (PV). When both legs merge near the suction surface, the suction side leg lifted off from the endwall and according to Sieverding (1985), the rotational strength of passage vortex determined the trajectory of the suction side leg.

The secondary vortex model explained by Goldstein and Spores (1988) indicated the existence of suction side leg of horseshoe vortex above passage vortex. The observation obtained by Wang *et al.* (1995) supported the above findings, with the help of multiple smoke wires flow visualization and a laser light sheet techniques. They investigated the unsteady and periodically fluctuating nature of leading edge horseshoe vortex system.

The multi-vortex system related to the pressure side leg, slowly converted to single vortex pattern once it merged with the suction side leg. The merging of both legs caused the formation of passage vortex which was accounted as the major source of cascade total pressure loss. The suction side remained as a branch of passage vortex while it wrapped itself around the same. Wang *et al.* (1995) model clearly explained the formation of wall vortex on the suction surface at the point of merging of both legs of horse shoe vortex, through naphthalene mass transfer measurement. Gregory-Smith *et al.* (1988) investigated streamwise vorticity generation and secondary losses inside blade passage. Due to strong cross passage pressure gradient, more low momentum boundary layer fluid entrained into the passage vortex. Towards the downstream side of the passage, corner vortex displaced the passage vortex, a little away from the suction surface. As the vortex size increased, the line which separated the passage vortex and suction side leg of horseshoe vortex shifted upwards along the suction surface. Because of viscous dissipation, reduction in the strength of passage vortex had been observed at downstream of trailing edge. The influence of inlet boundary layer thickness was seen to affect the intensity of secondary vortex formations, but with little change to their location.

In general, at the inlet of a turbine rotor, the incoming boundary layer was skewed in the direction opposite to the cross passage pressure gradient. As a result, negative incidence induced at the endwall region enhances the secondary flows. In this context Walsh and Gregory-Smith (1989) investigated the fundamentals of inlet skew (negative, collateral & positive skew) and also examined the authenticity of certain widely used correlations. They observed that, the addition of negative skew at the inlet resulted in a higher level of flow overturning relative to the one experienced in the collateral case. In contrast to this, addition of positive skew results in the obvious elimination of the overturning to give a more uniform flow appearance. In the negative skew case, enhancement of secondary flow structures was observed due to the earlier merging of both pressure side and suction side leg of horse shoe vortices. Towards the aft portion of the passage, regions of positive vorticity were observed over the endwall and blade

wake region in all skew cases. The enhanced vorticity at the inlet was especially seen to result in a greater passage vortex loss core at the outlet of the blade passage. Positive skewness substantially reduced the strength of passage vortex when compared with other situations.

2.2 The aerodynamic behaviour of purge flow

Burd and Simon (2000) investigated the effects of slot bleed cooling flow introduced upstream of the blade passage through an inclined slot. The impact of pitchwise static pressure difference at the coolant slot exit had resulted in the skewing of slot exit velocity profile. For higher bleed flow ratio (BFR), streamwise momentum to the inlet boundary layer reduces the size and strength of secondary vortices. McLean *et al.* (2001) analysed the effect of coolant injection on Axial Flow Turbine Research Facility (AFTRF) of the Pennsylvania State University. They investigated the impact of coolant injection on turbine aerodynamic performances for root, radial and impingement cooling in a stationary frame of reference. Root injection exhibited strongest effects on all flow parameters. Radial and impingement cooling did not exhibit any variation on exit angle. For 1% cooling flow, tangential velocity component had showed strongest changes during root injection. Radial and impingement cooling energized the inlet boundary layer which resulted in the radial shifting of passage vortex but the strength remains unchanged. Impingement cooling caused reduction of total to total efficiency and root injection caused increase in total to total efficiency.

Paniagua *et al.* (2004) experimentally investigated interaction between hub endwall cavity flow and mainstream flow on transonic high pressure turbine. The entrainment of cavity flow into the passage vortex was noted and found that the static pressure was increased by 6% for 1.5% ejection of sealant flow. Blockage caused by the sealant ejection was the root cause of static pressure rise. Cold flow ejection also affected the Degree of Reaction. Static pressure variation at the vane exit got smoothened with sealant ejection. Reduction in the vane exit Mach number leads to better relative in-

cidence angle to the rotor. Reid *et al.* (2006) investigated the effects of purge flow on turbine performance at various seal gas flow rates. Efficiency measurements and rotor exit flow data were obtained. Unsteady wake–sealant flow interaction was also investigated. Increasing sealant mass fraction by keeping swirl velocity constant leads to more disturbances at upstream of rotor and stronger secondary losses. The tangential velocity of coolant was increased from 0% to 60% of rim speed and it was found that increasing coolant fraction leads to decrease in efficiency. Increased mixing leads to increase in negative incidence which inturn enhanced downstream disturbances.

Schuepbach *et al.* (2010) experimentally analyzed the unsteady interaction of injected purge flow with mainstream flow across a rotor blade on a 1.5 stage high work axial turbine. A 0.6% reduction of total-to-total efficiency had been detected for enhancement of purge injection rates from -0.14% to 0.9%. Though the peak vorticity values of the rotor passage vortex had reduced with the injected purge flow, rotational strength of the combined passage vortex and purge flow had enhanced. With injected purge flow, vortex strength of passage vortex and trailing edge shed vortex had enhanced by 10% and 30% respectively. Further to this they analysed the influence of purge flow on axisymmetric endwall base line case and two non-axisymmetric profiled endwall cases on the same experimental set up (Schüpbach *et al.* 2011). They focused on the detrimental effects of rim seal purge flow in the presence of profiled endwalls. They found that base line axisymmetric endwall case showed efficiency decrease of 0.6% per percentage of purge air injected. First and second non-axisymmetric endwall case shows efficiency decrease of 1.2% and 0.7% per percentage of purge injection respectively. As the purge flow turned around the rotor leading edge, streamwise vortices were predicted up to 35% of axial chord which again merges with rotor passage vortex. The first endwall design leads to the strongest pressure fluctuation at the rim seal exit which leads to high blowing and more mixing losses. For the second endwall design, due to uniform pressure distribution at the rim seal exit, sensitivity towards purge flow had reduced.

Experimental investigation of Schrewe *et al.* (2013) confirmed the observations made by Schuepbach *et al.* (2010) & (Schüpbach *et al.* 2011). Schrewe *et al.* (2013) conducted experimental analysis in a 2 stage large scale turbine test rig. They found that turbine efficiency was decreased by 0.6% when the injection rate varied from -0.28% to 1.5%. Blockage effects generated by the purge air, intensification of secondary vortex structures, variation in the angle of incidence were the major reasons identified for the efficiency decrease. Variation in the velocity magnitude between purge flow and main annulus flow enhanced mixing losses and ingress of stagnation pressure field into the seal gap leads to the need of high purging rates.

Various coolant injection rates of -0.1%, 0.8% and 1.2% had been investigated by Regina *et al.* (2015) on the same test rig used by Schuepbach *et al.* (2010). Most noticeable change adopted was the increased axial spacing between the first stage stator and rotor blade rows. They found that for each percentage of purge injection, isentropic total-to-total efficiency had decreased by 0.8%. For injection rate of 1.2% the passage vortex loss core had shifted 7% radially along the span of blade. Analysis at off-design conditions concluded that, negative variations in the incidence on rotor blades had made favourable impacts on stage efficiency and rotor passage vortex evolution. Cui and Tucker (2017) numerically analysed the effects of purge flow and incoming secondary flows with shedding wakes over mainstream flow. The authors stated that 1% purge flow can enhance the secondary loss generation by 10%. Incoming wakes together with secondary vortices can further increase the loss generation by 20%.

2.3   The thermal behaviour of purge flow

The complex secondary flow structures had made the endwall region of blade passage significantly difficult to cool. Blair (1974) experimentally quantified the influence of secondary vortices on endwall heat transfer and film cooling effectiveness (FCE) distribution. The formation of horseshoe vortex had resulted in heat transfer enhancement at the blade leading edge. The continuous transfer of injected coolant from blade pressure

surface to suction surface had reduced FCE distribution towards blade pressure surface. Increase in the boundary layer thickness due to coolant ejection leads to reduction of heat transfer. Vane corner vortex formed between the suction surface and endwall had strong effects on endwall heat transfer rate at trailing edge region. Coolant ejection did not have much impact on corner vortices.

Burd and Simon (2000) experimentally studied thermal performance of bleed injection through an inclined slot kept before stator blade. Test was conducted on a high pressure turbine linear cascade comprised of two blade passages: one with flat endwall and another with contoured endwall. They concluded that, secondary flows had huge influence on endwall and suction surface film cooling. Measured quantity of bleed air was supplied through the inclined slot upstream of the nozzle guide vane passage. At the lowest bleed flow rates, coolant was convected across the contoured endwall surface to accumulate near the suction surface. Numerical predictions by Roy *et al.* (2000) accurately predicted the formation of secondary vortex structures and its impact on the blade passage endwall heat transfer distribution. Numerical simulations had shown good quantitative agreement with the experimentally measured values. Laser light sheet-smoke visualization technique clearly identified suction side leg and pressure side leg of horseshoe vortex. In the baseline case (without upstream slot injection), high heat transfer distribution was observed at the region close to the leading edge and aft portion of the blade passage. In the presence of upstream slot injection, high heat transfer regions had diminished. It was attributed that slot injection prevents corner vortex formation close to the leading edge and pressure surface.

With the intention of protecting the aft portion of the blade endwall passage particularly near to pressure surface Wright *et al.* (2008) introduced discrete film cooling holes of cylindrical cross section at downstream half of the blade passage in addition to the upstream purge flow. The introduction of discrete film holes, reduced the quantity of coolant ejected through the purge slot. Clear demonstration of coolant entrainment by the endwall secondary flow vortices were obtained with pressure sensitive paint (PSP)

technique. With higher blowing ratios, the coolant exhibited a tendency to lift-off from the surface and minimize thermal protection. Though the direction of coolant ejection through discrete holes were oriented towards the pressure side, the trail of the coolant had followed the passage vortex. A good improvement in the endwall thermal protection was observed for the combined upstream slot and downstream discrete film hole configuration. Another significant analysis by Wright *et al.* (2009) includes the investigation of dependence of upstream disturbances on the film cooling effectiveness distribution. Upstream disturbances were generated by keeping cylindrical rods and delta wings at different pitchwise locations. They concluded that wake passing effects did not alter cooling effectiveness much but the vortex formed by delta wings had a major influence on the cooling effectiveness distribution. At higher flow rates, intense vortex formation from the delta wing had generated more turbulent mixing and the coolant was forced to separate from the endwall. Based on the inferences obtained from the previous analysis (Wright *et al.* 2008), Gao *et al.* (2009) introduced fan shaped laid back holes instead of cylindrical holes. The fan shaped holes generate broader film coverage and greater performance than the cylindrical holes. The efficacy of the shaped holes enhanced with an increase in the mean blowing ratio. Also, it exhibited total pressure loss reduction at the exit when compared with cylindrical holes. Another inference made was, variation in the hole layouts did not affects the film cooling effectiveness distribution. However, the authors identified the location of peak thermal stress and hotspots by analysing hole layouts.

Papa *et al.* (2012) performed mass transfer analysis on endwall and blade suction surfaces in the presence of purge flow at different blowing ratios of 0.5, 1 and 1.5. Naphthalene free and naphthalene saturated air was used to simulate the effects of purge flow emerging from the upstream inclined slot. From oil dot visualization it was understood that, a recirculation region was developed upstream of leading edge, which modified the growth of passage vortex. For blowing ratios of 0.5 and 1, the coolant was entrained into the passage vortex and moved up along the suction surface because of the transverse pressure gradient within the passage. However, at higher blowing ratio, the

coolant ejecting out of the purge slot possessed enough momentum to overcome traverse pressure gradient and resulted in the enhanced cooling effectiveness towards aft portion of the blade passage and pressure surface. The continuation of this investigation was conducted by Papa *et al.* (2017) and they focused on the numerical simulations to find the compatibility of shear stress transport (SST) transition model with experimental results. On the endwall and suction surface, where flow was highly three dimensional, transition model had shown good agreement with the experimental results.

Aizon *et al.* (2013) numerically investigated aerodynamic performance of turbine cascade with purge endwall cooling.They concluded that purge flow significantly affected the secondary flow fields within the blade passage. Even for a lower ejection of 0.75% of mass flow ratio (MFR), higher losses near the blade suction side was observed. An approximate expansion of 40% - 50% of loss core was captured. Highest loss was obtained for mass flow ratio of 2.24%. The newly generated vortical structures with higher swirling strength contributed more to the additional secondary losses. Measurement showed that the passage vortex loss core had shifted slightly towards midspan with increase in the mass flow ratio.

Barigozzi *et al.* (2006) observed that fan shaped film holes on flat endwall provided better endwall cooling than cylindrical holes at low coolant ejection rates. Formation of horseshoe vortex made significant difficulty in cooling, regions close to leading edge and pressure surface since the coolant ejected had been entrained by the cross flow from pressure to suction surface. Moreover, the coolant ejected from the holes located on the line of separation of secondary vortices had shown a tendency to lift-off from the surface. Inference made from the analysis of combined influence of contoured endwall and discrete film cooling holes was that, on contoured endwall, reduction in the aerodynamic loading at the upstream portion of the blade passage resulted in more uniform distribution of local blowing ratio through out the first row of holes provided in front of leading edge (Barigozzi *et al.* 2010). Introduction of traverse trench at first two rows of cooling holes resulted in film cooling effectiveness enhancement at the up-

stream blade passage at higher blowing ratios. Higher turbulent mixing generated due to coolant-mainstream interaction within the trench that caused the coolant to spread more laterally with little separation from the solid surface (Barigozzi *et al.* 2012*a*).

Many other design variations had been reported by Barogozzi *et al* to improve the FCE distribution without generating much thermodynamic penalties. The use of fins in the purge slot provided more tangential velocity component to the coolant ejecting out of upstream slot. The inference made was, more the tangential component higher would be the loss generation (Barigozzi *et al.* 2014). Findings made was similar to the explanation made by Walsh and Gregory-Smith (1989) with inlet boundary layer skew. As a continuation, along with the fins, Barigozzi *et al.* (2013) analyzed the impact of interface seal gap geometry on aerothermal performance of rotor cascade. A misalignment between the rotor and stator endwall platform was generated and its influence on FCE distribution was obtained. The conclusion made was, seal gap geometry variation had little effect on secondary loss generation, but a marginal improvement of tangential distribution of the coolant was achieved over the endwall. Apart from endwall cooling, a detailed experimental analysis of pressure side cut back, together with discrete cooling holes on the blade trailing edge was conducted by Barigozzi *et al.* (2012*b*). Coolant ejecting out of the slot remains attached to the cut back section and provides additional momentum to the boundary layer fluid. As a result, even at low coolant ejection rate, reasonable trailing edge thermal protection can be achieved without any aerodynamic penalties.

Sangan *et al.* (2014) experimentally investigated the performance of datum double rim seal and another with a series of additional radial fins. In gas turbines, rim seals are used to attenuate circumferential pressure gradient radially across the wheel space disk cavity. This circumferential variation of pressure was the root cause of hot ingress. Radial finned seals were more capable of reducing pressure asymmetry by generating solid body rotation inside the wheel space. From the sealing effectiveness calculation, it was observed that quantity of sealing air could be reduced for finned double seal

configuration. Distribution of swirl was almost similar for both rim seals at various seal flow rates inside the inner wheel space.

Song *et al.* (2017) investigated the effect of purge flow on film cooling and aerodynamic characteristics of the endwall using three-dimensional Reynolds-averaged Navier-Stokes equations coupled with the k-ω turbulence model. In this paper both geometry of upstream slot and flow conditions of the purge flow were considered. They concluded that increase of coolant ejection angles reduced cooling effectiveness and decreased heat transfer coefficient of endwall. When the purge exit angle was varied from 30^0 to 90^0, 53.4% reduction of endwall averaged film cooling effectiveness was observed at MFR 1.5%. For the same variation of coolant ejection angles, heat transfer coefficient at leading edge was increased by 18.89%. The purge flow can increase the horseshoe vortex intensity and can cause separation vortex to enhance the local heat transfer coefficient of the endwall.

Zerobin *et al.* (2017) analyzed the generation of unsteady pressure patterns by the stator-rotor interaction on a one and half stage experimental test facility consisting of high pressure turbine (HPT), turbine centre frame (TCF) and low pressure turbine (LPT) vane. In another comprehensive study, the author analyzed the effects of individual tip and hub purge flow on TCF aerodynamics and concluded that, total pressure loss of TCF can be effectively lowered by proper reduction of purge flow rate (Zerobin *et al.* 2018*b,a*). Li *et al.* (2019) simulated non-uniform inlet temperature profile and swirl distribution in between the combustor and high pressure vanes and stated that non-uniformity in the heat load influenced axial temperature distribution between the successive blades while swirl orientation dominated radial temperature distribution.

2.4   The role of upstream wakes

The purge flow cooling became more challenging with the presence of an upstream disturbances/wakes. Few researchers had studied this effects by simulating the wakes by stationary or rotating cylinders (Ou *et al.* 1994; Mehendale *et al.* 1994). Effect of

unsteady wakes on film cooling effectiveness distribution over a fully-cooled turbine blade surface was conducted by Mhetras and Han (2006). Influence of progressing wake was analyzed by changing the location of stationary rods. Wake progression close to leading edge and suction surface, exhibited detrimental effects on the film cooling effectiveness distribution particularly on suction surface.

Park *et al.* (2014) experimentally investigated the influence of unsteady wakes on endwall heat/mass transfer with naphthaline sublimation technique. Influence of unsteady wakes were evaluated by conducting the experiment at different Strouhal numbers. Presence of thin inlet boundary layer and high turbulent intensity enhanced the heat transfer over the region between pressure side corner vortex and passage vortex and this phenomenon increased with increase in Strouhal number.

Unsteady heat transfer analysis by Hwang *et al.* (2016) revealed the impact of periodic nature of upstream wakes on the temperature distribution over the succeeding blade surfaces. Choi *et al.* (2017) investigated the effects of wake on flow and thermal endwall characteristics at different Strouhal numbers. The disturbed secondary vortices induced by the wake made heat transfer distribution over the endwall more uniform compared to non-wake case.

Zhou and Zhou (2018) found that, periodic interaction of unsteady upstream passage vortex reduced the minimum axial length of tip leakage vortex breakdown by 15% which improved the overall aerodynamic performance. Influence of different wake profiles on boundary layer transition and suction side separation were numerically explained by Hammer *et al.* (2018). He observed that, weaker wakes lead to the generation of large and long lasting separation bubbles and increased profile losses.

2.5   The endwall contouring

Over the past decade, numerous researchers had widely studied endwall contouring as an important method for controlling secondary flow and reducing aerodynamic losses.

The distinction between axisymmetric and non-axisymmetric geometries can be rendered for endwall contours. The latter offer the possibility of having a highly effective influence on the secondary flow. Morris and Hoare (1975) and Atkins (1987) non-axisymmetric designs showed modest improvement. For example, Morris and Hoare (1975)'s endwall design created a large loss reduction in the half-span adjacent to the flat wall but significantly increased the losses near the contoured endwall. With the goal of controlling static pressure distribution at the inter-stage axial distance, Rose (1994) introduced tangential (or non-axisymmetric) endwall contouring which showed promising outcomes. In the following years, thorough research work was carried out to use this method to minimize secondary flows. In particular, Yan *et al.* (1999); Hartland *et al.* (1998, 2000); Hartland and Gregory-Smith (2002); Harvey *et al.* (2000); Ingram *et al.* (2002); Ingram (2003); Ingram *et al.* (2005); Gregory-Smith *et al.* (2001) had obtained detailed results of secondary loss reduction with non-axisymmetric endwall contouring on Durham Cascade.

Effective transfer of blade profile from Durham to Rolls Royce Trent series (Brennan *et al.* 2001; Rose *et al.* 2001; Harvey *et al.* 2002) and the application of non-axisymmetric endwall contouring in the new design resulted in the reduction of secondary losses and stage efficiency improvement of 0.9% had been reported. Using a low speed linear cascade experimental test facility running at design incidence and inlet Reynolds number of 126000, Knezevici *et al.* (2010) assessed the efficiency of a contoured endwall generated using gradient-based optimization algorithm. Praisner *et al.* (2007) extended this work numerically on a conventional lift and two high lift airfoil designs with separate individual optimum endwall designs and observed 10% reduction of total pressure loss for endwall contoured Pack B case. Germain *et al.* (2008) demonstrated the numerical analysis of a tangential endwall contouring for the hub and the first stator shroud as well as the rotor hub. The design was based on Nagel and Baier (2003). The authors commented a major efficiency gain that was experimentally calculated by Schüpbach *et al.* (2008) as $1\% \pm 0.4\%$. In the wake of the first stator the increase in output was accomplished by lower losses. A second design by Schuepbach

et al. (2009) resulted in a 0.3 per cent efficiency gain, based on a loss-reduced rotor flow.

Denton and Xu (1999) offered an exhaustive description of the physical effects of blade lean. In a linear cascade Harrison (1992) investigated both straight and composite lean blade profiles. He found that compound lean reduced the spanwise variation in the yaw angle, that would lead to an increase in turbine efficiency. Dunn *et al.* (2009) showed that endwall cross flow reduction can be accomplished by modifying the endwall shape to influence the radial pressure gradient. Experiment was conducted in a 1.5 stage low speed turbine at design level and a considerable increase in the turbine stage efficiency was achieved. Saha and Acharya (2008) performed three dimensional numerical simulations of a non-axisymmetric endwall configuration to reduce total pressure loss and compared the results of the heat transfer with the standard endwall. The area-averaged Nusselt (Nu) number was reduced by 8% at the endwall. One of the key findings includes 3.2% reduction in the overall pressure loss at the downstream of the blade passage.

Torre *et al.* (2011) tried to control the flow dynamics of horseshoe vortex, besides controlling endwall cross passage flow both experimentally and numerically. Significant reduction in the product of secondary kinetic energy and helicity was observed from the experimental analysis. This finding was reflected in the numerical analysis, even though it overestimated the secondary flows for contoured endwall and underestimated for planar case. Obaida *et al.* (2019) numerically analyzed the performance of an optimized groove over upstream stator hub which captures the pressure side leg of horseshoe vortex effectively. The experiment was performed in a 1.5 stage axial turbine at three different operating conditions. At part-load operating condition an increase of stage isentropic efficiency by 1.03% was predicted. Similarly at design condition, 1.60% and at chocking point, 1.16% improvement was observed. Qu *et al.* (2019) numerically evaluated the combined effects of upstream wakes and endwall contouring on an efficient endwall static pressure distribution and reduction of secondary losses was

achieved. The influence of Reynolds number was also discussed. In the presence of upstream wakes the contoured endwall reduced the strength of passage vortex loss core by 59% and that of counter vortex by 73%. Effects of blade profiling investigated by Eric Lyall *et al.* (2014) and Sangston *et al.* (2017) explored the reduction in the turbulence production as a result of reduction in the turbulent stresses and velocity gradients. Blade profiling was achieved by combining high staggered-front loaded blade profile at midspan and its low staggered version at the endwall. The new profile eliminated the induced shear layer which caused the migration of passage vortex towards blade suction side.

Poehler *et al.* (2015) and Niewoehner *et al.* (2015) conducted research on a 1.5 stage test turbine using various tangential endwall contour (TEWC) designs which displayed an overall increase in turbine output. The losses in the stator increased, while losses in the passage of the rotor were lower than those for the system without the TEWC. Similar findings were also established by Zimmermann *et al.* (2017).

Abraham *et al.* (2012) and Panchal *et al.* (2012) presented experimental and numerical analysis on a transonic turbine cascade with two different contoured endwalls specifically designed for optimizing aerodynamic and heat transfer performances. At downstream of the trailing edge, a 3% drop in area averaged losses was achieved with the aero-optimized contoured endwall while the loss reduction exhibited by heat-transfer optimized contour remained comparable with the baseline case (flat endwall). From the heat transfer point of view, the authors concluded that both the aero-optimized (AO) and the heat-transfer-optimized (HTO) geometries resulted in a major performance improvement for the high turning, high exit Mach number passage analysed. Dependence of heat transfer coefficient on the trajectory of the passage vortex was also revealed. Using the same experimental facility Roy (2014) explained the net heat flux reduction with aero-optimized endwall contouring in the presence of both upstream slot and mateface gap leakage flow.

Schüpbach *et al.* (2011) conducted experimental and numerical analysis on a 1.5

stage high work axial turbine and presented the influence of purge flow on non axisymmetric contoured endwalls imposed on both stator and rotor endwalls. They concluded that, when purge quantity was increased, the non-axisymmetric endwalls drop some of their advantage relative to the base case having axisymmetric endwalls. In the subsequent study Jenny *et al.* (2012) used shrouded rotor with thinner airfoils which resembles low pressure turbine. He stated that, with the increase in the purge flow, the size of the pressure side bubble also increased. With the help of particle tracking, the author revealed the trajectory of pressure side bubblw (PSB) towards the hub endwall and across the blade passage.

Okita and Nakamata (2008) found that the cross flow in the blade passage was decreased with endwall contouring, which caused the film cooling effectiveness distributions to be more uniform in pitchwise direction and the pitchwise average film cooling effectiveness values to be greater compared to flat endwall. Similar inferences were also reported experimentally by Rezasoltani *et al.* (2014) on a three stage turbine facility. However, findings made by Lynch *et al.* (2011) by placing discrete film holes near airfoil pressure side shows that the coolant transfer from the airfoil pressure to suction side were prevented due to a decrease of the cross flow by endwall contouring. The pitchwise distribution area of the coolant has been reduced. Mensch and Thole (2016) rearranged the orientation of the film holes along the direction of streak lines on both flat and contoured endwall (designed by Praisner *et al.* (2007)). While film cooling effectiveness enhanced with contouring, the internal impingement effectiveness deteriorated because the varying distance between the impingement plate and film hole inlet.

In recent literatures, Chen *et al.* (2020) used multi-objective optimization technique to identify an optimum contoured endwall profile which can exhibit improved heat transfer as well as aerodynamic performance. He revealed the non-monotonic nature of total pressure loss coefficient and film cooling effectiveness with increasing mass flow ratio (MFR) values. The appropriate range of MFR was found to be between 1.0% < MFR < 1.5% to achieve higher adiabatic cooling performance and lower aerody-

namic losses. In another numerical study he explained the impact of streamwise and radial pressure gradient on film cooling effectiveness at different blowing ratios in the presence of contoured endwall.

2.6 Motivation

The detailed literature review presented in this chapter reports various turbine blade passage flow parameters influenced by the purge flow. Most of the literatures on purge flow have focused on blade endwall thermal protection and overall passage aerodynamics specifically at blade exit regions. However some factors are explained clear-cut, but some still need more consideration. Features such as evolution of vane trailing edge wakes (upstream wakes) and its interaction with purge and mainstream flow are neglected and needs more attention. From the available literatures related to upstream wakes, it is well understood that its influence on secondary flow and losses could not be avoided. The dependency of wake structure or its geometrical appearance on time as well as space needs to be quantified. That means further computational or experimental investigations are imperative to expand the general understanding of upstream wakes interaction with the mainstream as well as blade profile in the presence of purge flow.

Despite the maximum productivity of modern gas turbines, the continuously increasing fuel price and strict emission standards pushed the designers to develop more efficient engines where a minute improvement are precious. Hence effective loss reduction technique such as non-axisymmetric endwall contouring has to be implemented in order to compensate for the aerodynamic penalty generated by the purge flow. The majority of the investigations performed on this topic had concentrated on designing various endwall geometries with minimum secondary losses. Although most of the current literatures addressed the advantages of endwall contouring from an aerodynamic efficiency perspective, the studies that describe the efficiency of contouring in the presence of purge flow are limited. Moreover greater turning and increased blade loading may cause the boundary layer on the blade pressure surface to separate and pressure

side bubble (PSB) has been generated even at design conditions. The existence of pressure side bubble has been reported by some literatures, but they failed to put forward an effective way to attenuate it. However these limited literatures concluded that influence of PSB on secondary flow and losses could not be neglected. Hence, an indepth analysis is required to bring forward an effective contoured endwall design which can mitigate the pressure side bubble formation and reduce blade exit secondary losses.

2.7   Objectives of the study

The research aims at obtaining a better understanding of fundamental vortex formations within a linear turbine cascade, specifically the flow physics related to upstream purge flow has been given importance. Further a detailed investigation of unsteady interaction between the upstream wakes and purge flow are formulated. With the perspective of reducing the deleterious effects of purge flow, research objectives are expanded to the field of non-axisymmetric endwall contouring.

The present investigation has the following specific objectives.

1. To understand the effect of velocity ratio (M) and purge ejection angle (α) on the loss coefficients in a linear turbine cascade.

2. To investigate the influence of upstream wakes on the secondary flow losses in the presence of purge flow.

3. To study the formation and evolution of upstream wakes with respect to time and its interaction with purge flow.

4. To explore the effect of contoured endwall on purge flow in the presence of pressure side bubble (PSB).

5. To investigate the transient behaviour of pressure side bubble formation and its effective mitigation by contoured endwall in the presence of purge flow.

CHAPTER 3

RESEARCH METHODOLOGY

Primarily, numerical investigations are carried out to achieve the objectives. Few experiments have also been carried out to validate the numerical results. This chapter details the methodologies adopted for both experimental and numerical studies.

3.1 Experimental Methodology

3.1.1 The cascade wind tunnel

The experimental investigations are carried out on a low speed blowing type cascade wind tunnel available at the Turbomachinery Laboratory of National Institute of Technology, Karnataka (Figure 3.1). Air is fed to the cascade test section by means of axial fan. The 5 KW AC motor which drives the fan, is equipped with a variable frequency drive (VFD) which can control the fan speed over a range of 0 to 2880 RPM. At the circular entrance of the wind tunnel, mesh type safety screen is provided to protect the fan and related components from loose objects. The air then flows through a series of screens and settling chamber before emerging through a contraction cone region, into the test section. The contraction cone region linearly accelerate the air. To homogenize the incoming mainstream, honeycombs are installed within the settling chamber. A turbulence grid is provided upstream of the test section to minimize the turbulence intensity within 5%.

3.1.2 The test section

The linear turbine cascade chosen for the present analysis is equipped with high pressure low aspect ratio turbine blades. The cascade consists of five blades and the blade

Figure 3.1: Blowing type subsonic cascade wind tunnel.

profiles are designed with aerodynamic similarity (Figure 3.2). The cascade blades have an axial chord (C_{ax}) length of 100 mm and span of 120 mm which gives the blade an aspect ratio of 1.2. Aspect ratio can be defined as the ratio of blade span to axial chord distance. In order to obtain an optimum periodic condition, head boards and tail boards are provided upstream and downstream of the cascade respectively. The purpose of providing headboard is to control the incoming mass flow rate while tail board is installed to direct the exit flow. To maintain the flow conditions as close as possible to constant velocity within the test section against day by day varying atmospheric conditions, small air speed changes are made with the help of VFD. Inlet velocity is measured at 1.06% of C_{ax} upstream of the center blade with the help of pitot static tube. Inside the test section, the blades are screwed to 5 mm thick acrylic sheet which serves as smooth endwall. The complete test section is mounted on height adjustable rectangular frame made of mild steel. Turbine blade parameters and specifications are described in Table 3.1 and the test section is shown in Figure 3.3.
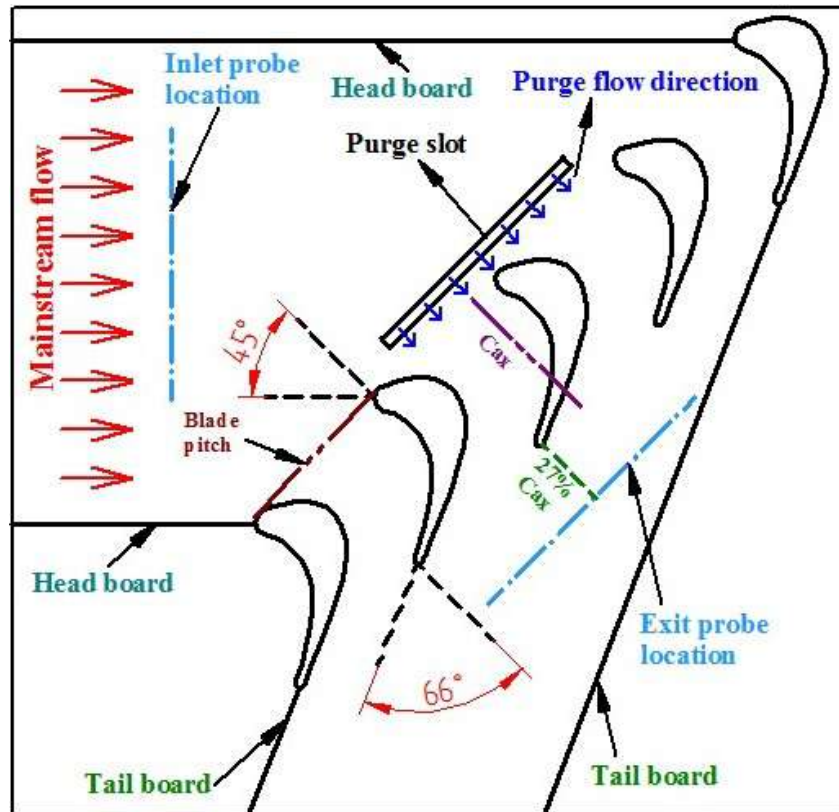
Figure 3.2: Schematic diagram of cascade test section.

3.1.3 The five hole probe

The experimental facility consists of a five hole pressure probe (tip diameter of 2.05 mm) (Figure 3.4) with a traverse mechanism at the downstream of the blades. Ease of implementation, robustness, reliability and simplicity in working principle makes application of conventional 5 hole probe more acceptable. Out of the five holes, the hole which is more aligned with the flow reads higher pressure. Readings from the left and right holes provides yaw angle while measurements obtained from top and bottom holes indicates pitch angle. The difference between the pressure readings from each holes depends on the size of the individual probe head. In the absence of direct analytical solution to measure pressure difference between each holes, the common procedure followed is, calibrating the probe in advance by rotating it through a range of fixed angular intervals in both pitch and yaw directions. The information thus obtained is saved in
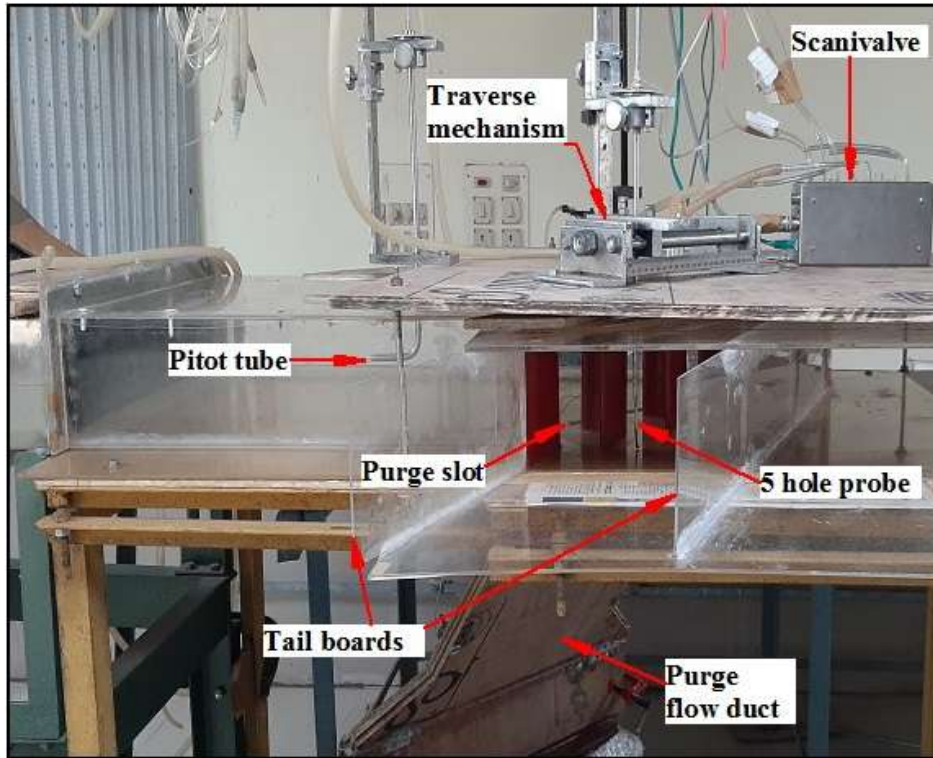
Figure 3.3: Linear cascade test section.

a matrix format, generally named as calibration data, from which, the required pressure coefficient and angular coefficients can be calculated (Reichert and Wendt 1994; Pisasale and Ahmed 2002; Nowack 1970; Ostowari and Wentz 1983). Several literatures have proposed calibration algorithm which can accurately predict the three dimensional flow field parameters such as total pressure, static pressure, yaw angle, pitch angle as well as three components of resultant velocity vector (Georgiou and Milidonis 2014; Town and Camci 2011; Gündogdu and Çarpinlioglu 1998; Ligrani *et al.* 1989; Treaster *et al.* 1979).

In the present analysis, probe calibration has been done over a range of +/- 30^0 in both pitch and yaw angle. The pre-calibrated probe has been moved in the spanwise and pitchwise directions in steps of 1 mm near to endwall and 5 mm away from endwall. The stem of the pressure probe has been kept along the spanwise direction and probe tip was aligned with the blade exit design angle.

Table 3.1: Turbine blade parameters

Inlet flow angle	45^0(from axial direction)
Blade exit angle	-66.3^0(from axial direction)
Total blade turning angle	118.3^0
Blade axial chord length	100 mm
Blade pitch	112 mm
Blade span	120 mm
Aspect ratio	1.2
Re	2×10^5
Zweifel loading coefficient	1.18

Figure 3.4: Conventional five hole probe.

3.1.4 The traverse mechanism

The traverse mechanism which carried five hole probe is shown in Figure 3.5. The vertical limb which carry the five hole probe is bolted to the horizontal limb and the entire traverse mechanism is mounted on a rectangular plywood sheet of thickness 12 mm. A rectangular slot of length 20 cm and width 1 cm, is provided on the plywood for

the smooth movement of the five hole probe so that it can cover 1.8 times pitch distance over a full span range at the cascade exit (127% C_{ax}).
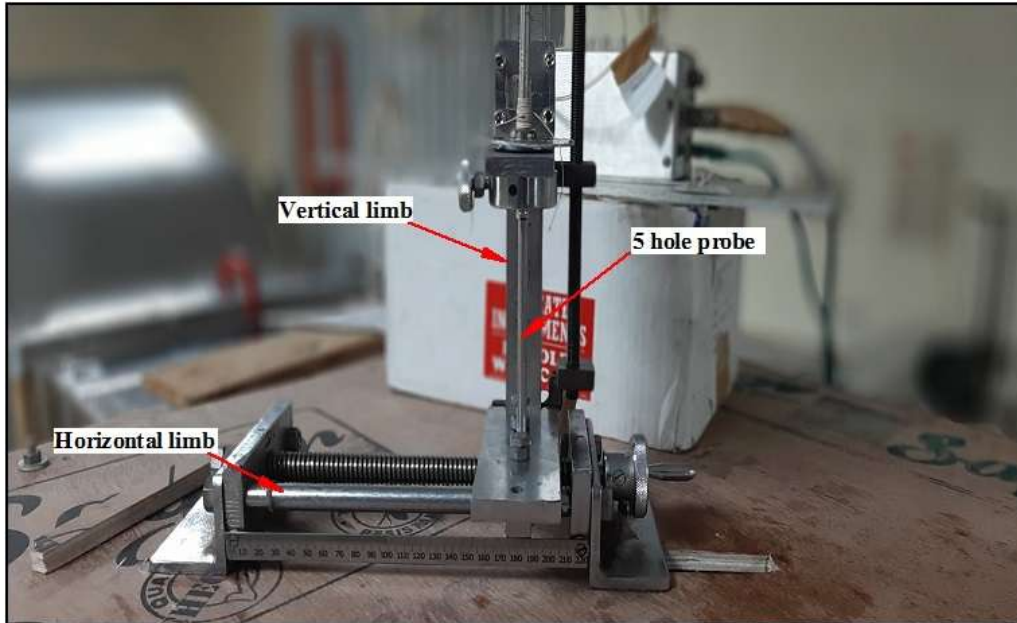
Figure 3.5: Traverse mechanism with five hole probe.

3.1.5   Boundary layer measurement

The fluid region which bounds any solid surface where viscous effects are significant can be defined as boundary layer. The general definition of boundary layer thickness is the distance from the solid surface to the location at which local velocity of the viscous stream becomes equal to 99% of the freestream velocity. The virtual distance that the solid surface has to be displaced in order to compensate for the velocity deficit within the boundary layer can be called as displacement thickness. Similarly, momentum thickness implies the virtual distance displaced by the solid surface to compensate for the momentum deficit within the boundary layer. Boundary layer thickness directly measured from the inlet pressure profile is 12.48 mm. The functional relationship obtained for the velocity, inside the boundary layer is expressed in Equation 3.1. Similarly, displacement thickness and momentum thickness calculated using Equations 3.2 and 3.3 are 0.94 mm and 0.79 mm respectively.

$$u = 2852317.42z^3 - 104556.91z^2 + 1276.37z + 12.85 \tag{3.1}$$

$$\delta^* = \int_0^\delta (1 - \frac{u}{U_\infty})dy \tag{3.2}$$

$$\theta^* = \int_0^\delta \frac{u}{U_\infty}(1 - \frac{u}{U_\infty})dy \tag{3.3}$$

In the present work, at the upstream side of the blades, a boundary layer rake (Figure 3.6) is kept to measure the incoming pressure profile (Figure 3.7). The boundary layer rake consist of 20 stainless steel tubes of internal diameter 0.25 mm and it can cover a spanwise distance of 34.5 mm. To get the finest profile, all tubes are oriented with appropriate inclination towards the endwall. Out of 20 tubes, signals from 16 tubes can be measured at a time using the Scanivalve pressure transducer. The spanwise position of each tubes are provided in Table 3.2. The incoming boundary layer profile measured using rake is represented in terms of total pressure coefficient (C_p). Total pressure coefficient can be defined as the ratio of total pressure to inlet dynamic pressure (Equation 3.4).

$$C_p = \frac{P_t}{0.5\rho_\infty U^2} \tag{3.4}$$

Figure 3.6: Boundary layer rake.
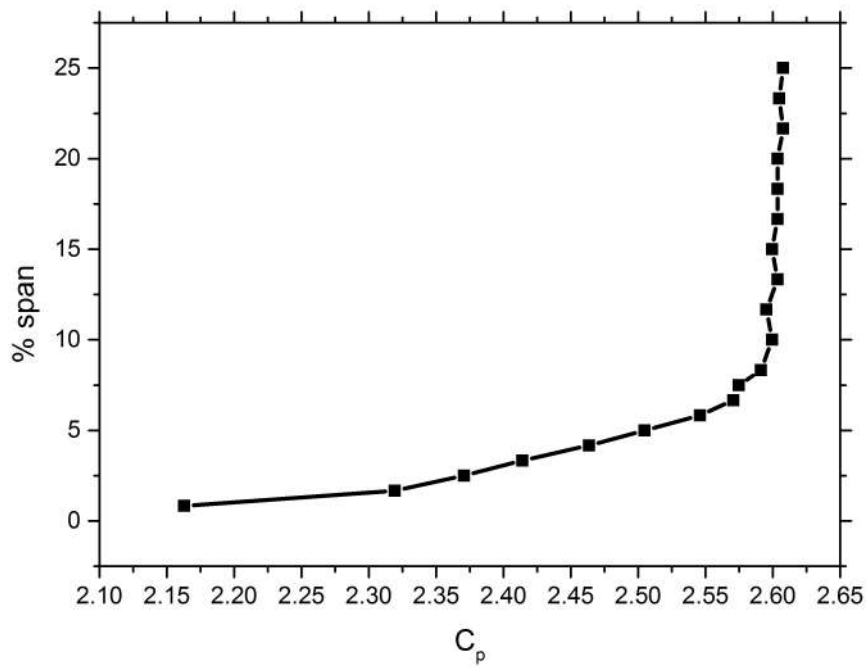
Figure 3.7: Inlet pressure profile.

Table 3.2: Spanwise location of rake tubes

SS tube number	Spanwise distance (mm)
1	0.5
2	1
3	2
4	3.5
5	4
6	5.5
7	7.5
8	9
9	11
10	13
11	14.5
12	16
13	18
14	20
15	22
16	24
17	27
18	28
19	31
20	34.5

3.1.6 The pressure transducer

Pressure fluctuations are measured using a digital pressure transducer (DSA3217), which can simultaneously accept 16 individual pneumatic inputs (Figure 3.8). The Scanivalve-DSA3217 module has an operational range of 15 psi absolute and has a power requirement of 28±8 V dc at normal operating conditions. Accurate measurement and simple operation made the use of Scanivalve pressure transducer widely acceptable. In DSA3217 module, the pneumatic ports are arranged in two rows and each row consists of 8 sensors. To each sensor, discrete piezoresistive pressure sensors, an A/D converter and a microprocessor are attached. The data received are saved to a EEPROM (electronically erasable programmable read-only memory) memory and it permits the module to

provide corrected output in desired engineering units. The pneumatic sensors are connected to the pressure tapings and five hole probe through flexible tubings of internal diameter 1.6 mm. All pressure signals were sampled for 0.1 sec at a frequency of 2000 Hz. The obtained readings are used to derive the flow parameters including flow angle and the total pressure. Uncertainty of pressure signals obtained from the Scanivalve-DSA3217 module is estimated to be less than $\pm 0.05\%$.

Figure 3.8: Digital sensor array - 16 channel pressure transducer (Scanivalve DSA3217).

3.1.7 The static pressure measurements

At the midspan of center airfoil, a series of holes of diameter 0.7 mm, have been drilled perpendicular to the blade surface to measure the static pressure. To obtain the endwall static pressure, a measurement grid is designed which consists of twelve equally spaced rows in the axial direction between leading and trailing edge over the hub endwall (Figure 3.9a). Each row contains minimum 18 to 22 miniature holes of diameter 1 mm and they are kept dense towards adjacent blade surfaces so as to capture a better resolution of boundary layer region. To each of these holes, stainless steel (SS) tubes of same outer diameter (1 mm) are glued to ensure 0% leakage between the SS tube and acrylic sheet (Figure 3.9b). The size of the holes are kept minimum to avoid measurement uncertainties. Scanivalve connected to the pressure taps directly measures the surface

static pressure. The measurement using five hole probe and surface pressure holes have an uncertainty of $\pm 0.5\%$ and the measured yaw angle has an uncertainty of $\pm 0.5^0$.

(a)

(b)

Figure 3.9: Endwall static pressure measurement setup a) miniature holes of 1 mm diameter drilled over the acrylic sheet b) stainless steel tubes glued to the miniature holes.

3.1.8 Purge flow arrangement

When the mainstream enters the cascade test section at room temperature, the secondary air (purge flow) ejected upstream of the cascade is fed at an elevated temperature of 55^0C, resulting in the density ratio of 0.93 (Barigozzi *et al.* (2014); Roy *et al.* (2000); Schobeiri *et al.* (2015)). The overall secondary purge flow arrangements are shown in Figure 3.10. Purge slot of width 7 mm kept 11% Cax upstream of the center blade leading edge covers nearly 1.5 times the blade pitch. A centrifugal blower driven by 5 HP AC motor is used to feed the purge air at a constant velocity ratio (M) of 0.13, where velocity ratio is defined as the ratio of coolant inlet average velocity (U_c) to the mainstream inlet average velocity (U). The purge flow is fed through a secondary flow line where the volume flow rate can be controlled with the help of a control valve and measured by a pre-calibrated orifice meter integrated within the secondary flow system. A pitot tube and thermometer are installed to measure velocity and temperature. The pitot tube can also be used to measure the pressure profile at the blower inlet. Pressure tapings are provided across the orifice meter and at blower inlet to measure pressure difference. The secondary air then flow through a heat exchanger where the temperature is raised before it is ejected through the purge slot. The heated air flows through a plenum chamber equipped with flow straightener. The purge slot has an angular inclination of 45^0 with the axial chord. This is achieved by installing a rectangular flow channel inclined at 45^0, over the plenum chamber. The outlet of the inclined rectangular channel exactly matches with the area of the upstream purge slot. K type thermometers having measurement accuracy of 0.1^0C and pressure tapings were provided inside the inclined channel to ensure uniform distribution of temperature and static pressure of the purge air.

3.1.9 The centrifugal blower for secondary air supply

Purge air is supplied with a centrifugal type single stage blower and it is driven by 5HP AC motor (Figure 3.11). When the impeller rotates, air is sucked through the
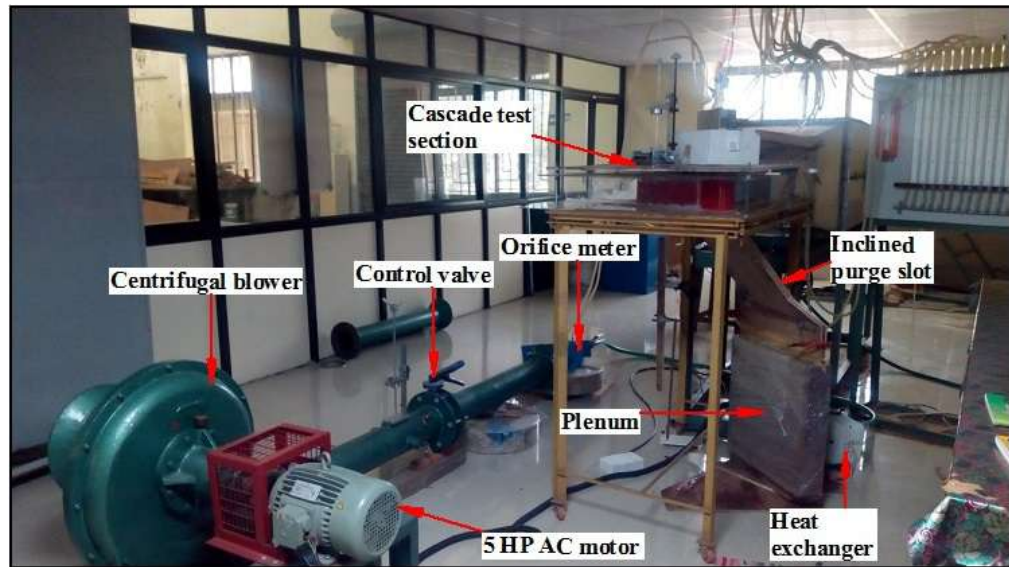
Figure 3.10: The secondary purge flow supply system.

blower inlet. While passing through the impeller, due to the centrifugal action, air get accelerated and exits with high velocity. The air then flows through the blower casing, where it is diffused out and converts a portion of the kinetic energy gained to pressure energy, before it emerges out from the outlet.

Figure 3.11: The centrifugal blower.

3.2 Numerical Methodology

3.2.1 Different configurations analyzed

The computational domains designed, which can complement the experimental set up as far as possible, could provide a better insight into the blade passage flow characteristics where experimental data extraction becomes difficult. In the initial phase of the numerical study, effect of velocity ratio and purge ejection angle on the loss coefficient and the film cooling effectiveness are analyzed. Later the effect of upstream wakes and its interaction with the purge flow is analyzed. The upstream wake is generated by a cylinder and its relative position with respect to leading edge of the blade is varied to obtain four different configurations (SSW, MW, PSW and STW). In the latter part of the numerical study three different endwall contours are designed (EC1, EC2 and EC3) and their influence on the loss parameters are studied with and without the purge flow. More detailed information about each of these configurations are given in the respective chapters. An overview of all simulation models are provided in the Table 3.3. A general outline of the computational domain, solver details and flow physics setup are discussed in this section.

Table 3.3: Computational configurations

SL No	Objectives	Fixed Parameters	Parameters / configurations investigated
1	Effect of velocity ratio	$\alpha = 90^0$	$M = 0.2, 0.4, 0.6, 0.8, 1.0$
2	Effect of purge ejection angle	M = 0.6	$\alpha = 30^0, 45^0, 60^0, 75^0, 90^0$
3	Effects of upstream wake	M = 0.6 & $\alpha = 45^0$	SSW, MW, PSW, STW
4	Effect of contoured endwall without purge	No purge	BC, EC1, EC2, EC3
5	Effect of contoured endwall with purge	M = 0.6 & $\alpha = 45^0$	BCp, EC1p, EC2p, EC3p

3.2.2 Computational domain

In all the configurations that are selected for this study, the computational domain consists of a single blade passage with periodic boundary conditions at side walls (Figure 3.12a). The domain inlet is kept at 1.5 times the axial chord distance (C_{ax}) upstream of the blade leading edge where experimentally obtained inflow conditions are applied. The outlet plane is located at two times the axial chord distance downstream from the blade leading edge. The purge slot having a width of 7 mm, length 50 mm and inclination 45^0, is located at 11% C_{ax} upstream of the blade leading edge (Barigozzi *et al.* (2014)) (Figure 3.12b). Purge flow ejects at a velocity ratio (M) of 0.6.

3.2.3 The solver details

Numerical evaluation of all configurations are carried out by commercially available finite volume solver ANSYS CFX. For its excellent precision, robustness, pace and cost effectiveness, CFX is extensively used in industrial applications specifically in turbomachinery field. ANSYS CFX uses a coupled solver, which solves the three dimensional Navier Stokes equations (for velocity and pressure) as an implicitly coupled single system. The coupled solver requires less number of iterations before convergence compared to segregated solver but the disadvantage of this is the longer time requirement for each iteration since it solves the three momentum equations and pressure based continuity equation simultaneously. CFX follows vertex centered method during discretization. In vertex centered method, values of the unknown variables solved are stored in the vertex and space surrounding the vertex constitutes the control volume.

3.2.4 Turbulence model

In general, flow around any complex irregular geometries are turbulent in nature. In CFD simulations, the flow turbulence can be dealt with different approaches. Where ever the CFD simulation fails to fully solve the length and time scales of a turbulent
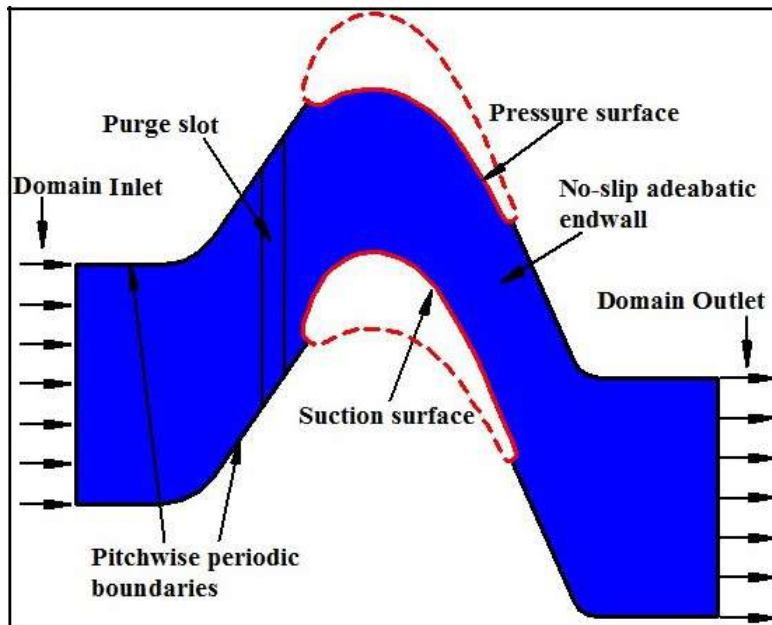
(a) BCp
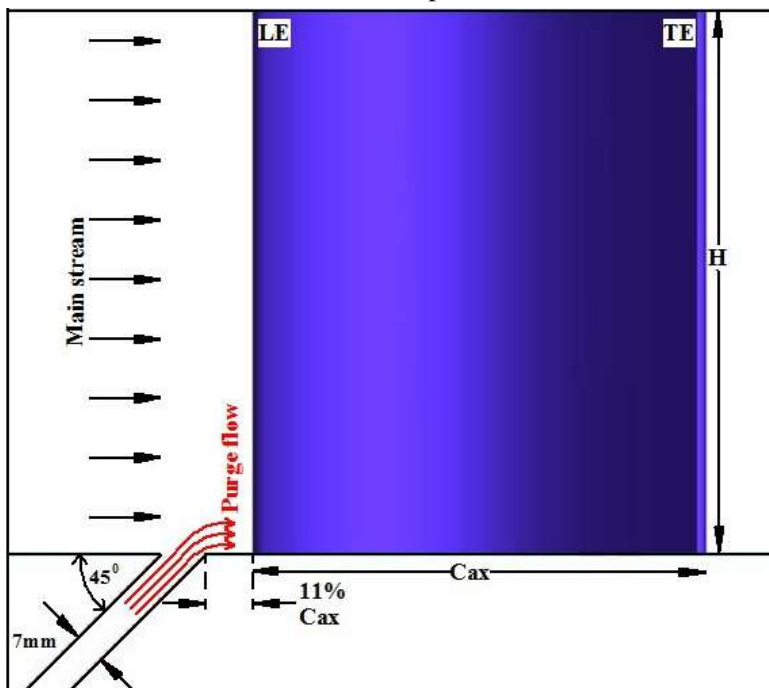
(b) BCp

Figure 3.12: a) Computational domain (Base case with purge - flat endwall) and b) Sketch of purge slot relative to blade position (Base case with purge - flat endwall).

flow, the requirement of various turbulence models emerge. The application of time averaging approach has reduced the high resolution demand of classical Navier Stokes equations and the equation thus formed is known as RANS, Reynolds Averaged Navier Stokes equation. However the time averaging process resulted in the formation of additional unknown fluctuating quantities which represents turbulent or Reynolds stresses. To solve these quantities additional informations are required and it is the responsibility of the turbulence model to provide these informations to achieve "closure". The term "closure" means sufficient equations are available to solve all unknowns including the Reynolds stress terms. The turbulence models can be classified as algebraic models, one equation models, two equation models and Reynolds stress models. The development of one equation turbulence models depends on one transport equation usually eddy viscosity. Basically two equation models consist of two additional transport equations which characterizes turbulent properties such as length and velocity scale. The Shear stress transport two equation turbulence closure model which follows characteristics of k-ω model in near endwall regions and that of k-ϵ model away from the solid walls and in free shear regions, has been adopted in the present work. In order to activate the benefits of both k-ω model and k-ϵ model together, Menter (1994) has designed a blending function F_1 whose value switch between 0 (free shear layer) and 1 (viscous sublayer) appropriately. The capability of SST turbulence model for simulations related to turbine cascade, has already been established in several literatures (Choi *et al.* (2017); Dunn *et al.* (2009); Turgut and Camcı (2011); Kiran and Anish (2017); Schobeiri *et al.* (2015)). The two transport equations of SST turbulence model in conservative form is expressed below (Equation 3.5 and 3.6).

Turbulence Kinetic Energy:

$$\frac{\partial(\rho k)}{\partial t} + \frac{\partial(\rho u_j k)}{\partial x_j} = P - \zeta^* \rho \omega k + \frac{\partial}{\partial x_j}\left[(\mu + \sigma_k \mu_t)\frac{\partial k}{\partial x_j}\right] \quad (3.5)$$

Specific dissipation rate:

$$\frac{\partial(\rho\omega)}{\partial t} + \frac{(\rho u_j \omega)}{\partial x_j} = \frac{\gamma}{\nu_t}P - \zeta\rho\omega^2 + \frac{\partial}{\partial x_j}\left[(\mu + \sigma_\omega\mu_t)\frac{\partial\omega}{\partial x_j}\right] + 2(1-F_1)\frac{\rho\sigma_{\omega2}}{\omega}\frac{\partial k}{\partial x_j}\frac{\partial\omega}{\partial x_j}$$

$$(3.6)$$

where

$$P = \tau_{ij}\frac{\partial u_i}{\partial x_j} \tag{3.7}$$

$$\tau_{ij} = \mu_t\left(2S_{ij} - \frac{2}{3}\frac{\partial u_k}{\partial x_k}\delta_{ij}\right) - \frac{2}{3}\rho k\delta_{ij} \tag{3.8}$$

$$S_{ij} = \frac{1}{2}\left(\frac{\partial u_i}{\partial x_j} + \frac{\partial u_j}{\partial x_i}\right) \tag{3.9}$$

$$\mu_t = \frac{\rho a_1 k}{max(a_1\omega, \Omega F_2)} \tag{3.10}$$

Closure Coefficients and Auxilary Relations are

$$\phi = F_1\phi_1 + (1-F_1)\phi_2 \tag{3.11}$$

$$F_1 = \tanh(arg_1^4) \tag{3.12}$$

$$arg_1 = \min\left[\max\left(\frac{\sqrt{k}}{\zeta^*\omega d}, \frac{500\nu}{d^2\omega}\right), \frac{4\rho\sigma_{\omega2}k}{CD_{k\omega}d^2}\right] \tag{3.13}$$

$$CD_{k\omega} = \max\left(2\rho\sigma_{\omega2}\frac{1}{\omega}\frac{\partial k}{\partial x_j}\frac{\partial\omega}{\partial x_j}, 10^{-20}\right) \tag{3.14}$$

$$F_2 = \tanh(arg_2^2) \tag{3.15}$$

$$arg_2 = \max\left(2\frac{\sqrt{k}}{\zeta^*\omega d}, \frac{500\nu}{d^2\omega}\right) \tag{3.16}$$

$$\Omega = \sqrt{2W_{ij}W_{ij}} \tag{3.17}$$

$$W_{ij} = \frac{1}{2}\left(\frac{\partial u_i}{\partial x_j} - \frac{\partial u_j}{\partial x_i}\right) \tag{3.18}$$

where ρ is the density, d is the distance between field point and nearest wall, F_2 is a function similar to that of F_1 and Ω represents absolute vorticity.

The constants are:

$$\gamma_1 = \frac{\zeta_1}{\zeta^*} - \frac{\sigma_{\omega1}k^2}{\sqrt{\zeta^*}} \tag{3.19}$$

$$\gamma_1 = \frac{\zeta_2}{\zeta^*} - \frac{\sigma_{\omega2}k^2}{\sqrt{\zeta^*}} \tag{3.20}$$

$\sigma_{k1} = 0.85$, $\sigma_{\omega1} = 0.5$, $\zeta_1 = 0.075$, $\sigma_{k2} = 1.0$, $\sigma_{\omega2} = 0.856$, $\zeta_2 = 0.0828$ $\zeta^* = 0.09$, k = 0.41,

3.2.5 Mesh generation

The computational modeling and grid generation are carried out using ICEM CFD commercial software. Fully structured hexahedral elements are used for the grid generation (Fig. 3.13). To capture the boundary layer regions, mesh refinement around the blade surface, cylinder surface and endwalls are achieved by implementing a combination of

O grid and H grid respectively. O-grid around the blade and cylinder surface consists of 55 node points with an exponential growth rate of 1.2 (Fig. 3.14). For all computational domains, y+ value of first grid point near to any solid surface is maintained below 1 except at small regions over leading edge and suction surface where it is observed to be 2.8 (Fig. 3.15). To get the desired y+ value, a near wall grid distance of 0.03 mm has been maintained all through out the domain. Air as an ideal gas which represents compressible viscous flow, is used as the working fluid.
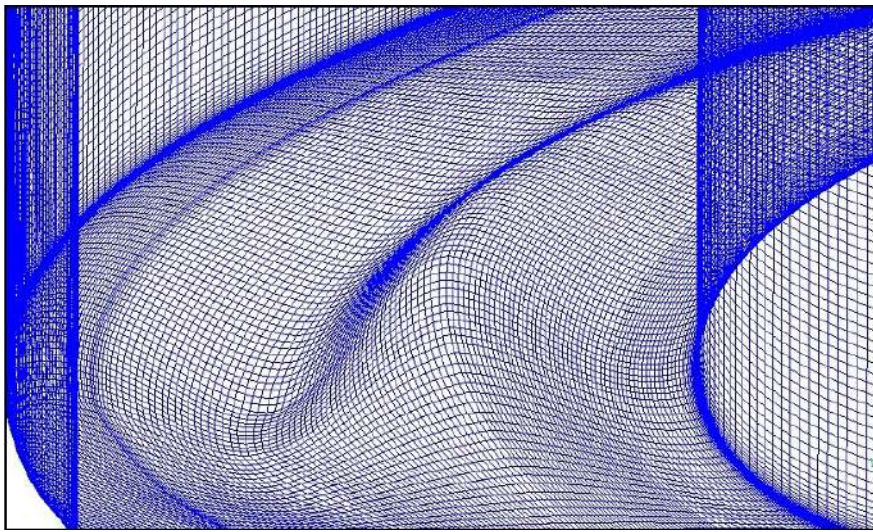
Figure 3.13: Structured mesh over the contoured endwall.
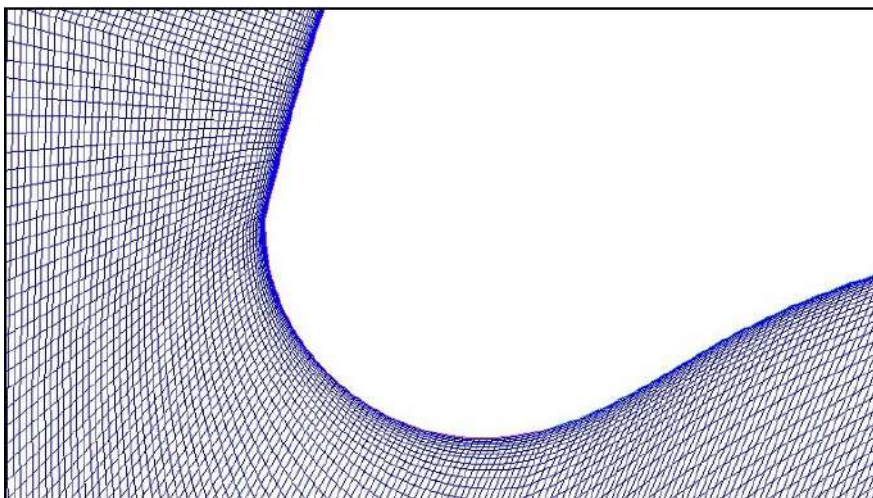
Figure 3.14: O-grid around blade leading edge.
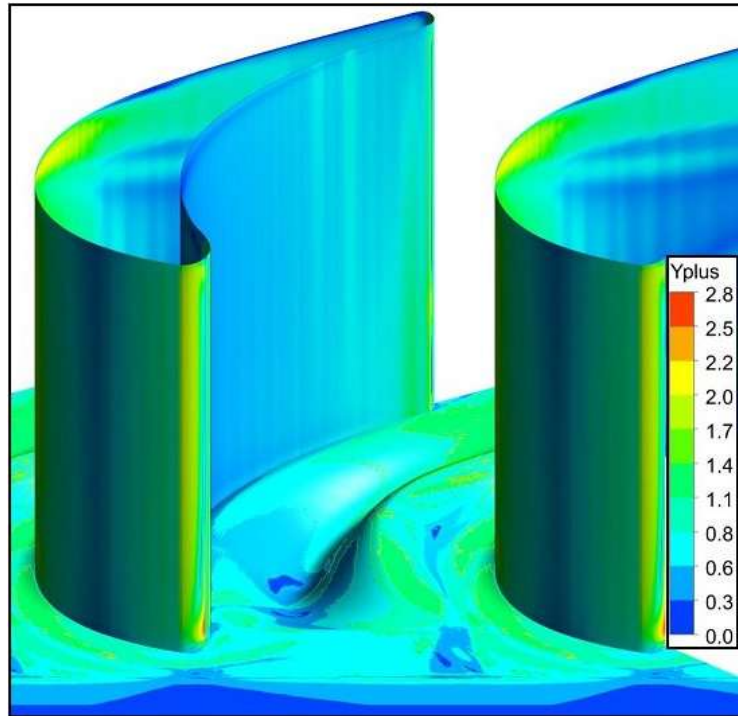
Figure 3.15: Y plus distribution over the contoured endwall and blade surface.

3.2.6   Boundary conditions

At the inlet, total pressure profile obtained from the experiment and 5% turbulence intensity obtained with the help of DANTEC 1D wire probe hot wire anemometer are specified. While at the outlet, fixed mass flow rate is applied. Inlet velocity of 10.73 m/s is specified at purge inlet. Accordingly the mass averaged total pressure and volume flow rate calculated at purge inlet are 391.85 Pa and 0.008416 m^3/s respectively. At one pitch distance translational periodic boundary conditions are applied. Adiabatic no slip boundary condition was applied for all solid surfaces. The mainstream flow is blown at room temperature whereas the secondary air enters at higher temperature (55^{0}C), resulting in a density ratio as 0.93.

3.2.7 The transient analysis

For transient analysis governing equations are solved at regular interval of time (time step). The size of the time step is a crucial parameter and its value should be small enough to sort out the time dependent features of a fluid flow. Larger time steps generally leads to the misinterpretation of true solution and exact flow behavior cannot be solved out. At the beginning of the transient simulation, a converged steady state solution is used for initialization. Due to the approximate initial guess, for the first few time steps the residuals may exhibit larger fluctuations and it can be disregarded till periodic behavior is observed (Figure 3.16). A time step value of smaller size can maintain the stability of the solver during this initial time period. For discretization, advection terms of momentum equations are evaluated using second-order accurate and bounded high-resolution scheme whereas for diffusion terms, shape functions are used to evaluate spatial derivatives. High resolution scheme uses a second order scheme as far as possible and blends to a first order scheme to maintain boundedness. It contains far less numerical diffusion. Also discretization of temporal term is achieved by unbounded, implicit, conservative time stepping Second Order Backward Euler scheme.

For the present analysis, the average time required for fluid to travel the full blade passage from leading edge to trailing edge is chosen as one period (one cycle). This time period is resolved with 55 time steps (τ) and each time step (τ) duration is 0.0001 seconds (Schneider *et al.* (2014)). A time independent study has been conducted and the minimum time step value of 0.0001 seconds that can accurately predict the wake propagation is chosen for the final transient simulation. The simulations are carried out for several cycles (16 time periods) and the results are taken from the last cycle. A series of inner loop iterations were carried out after each time step until convergence is achieved in order to correct the non-linearities for the output of that given time. During the simulations, variation of velocity at six locations (three before leading edge and three after trailing edge) are monitored with respect to time to ensure the numerical stability and the convergence is acquired when steady periodic velocity fields are observed
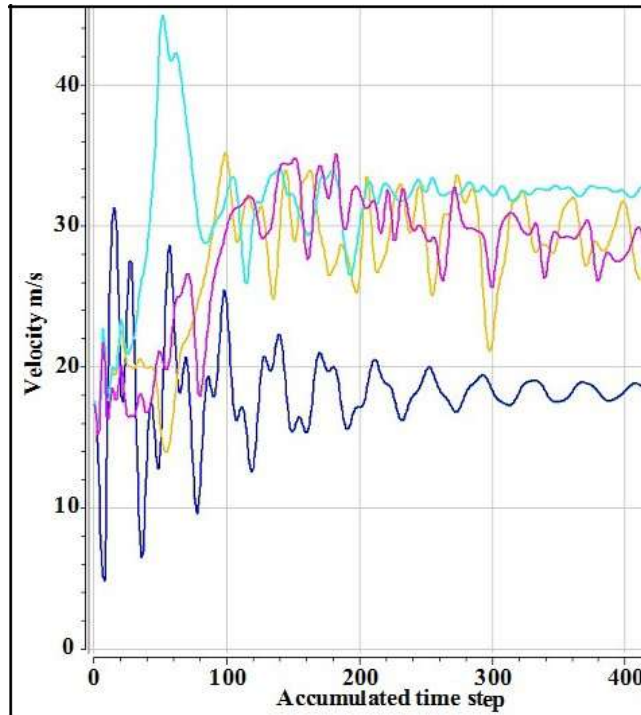
Figure 3.16: Time dependent behavior of velocity at different monitoring points.

at the monitoring points located at downstream of trailing edge. Residual values of the order of 10^{-6} is selected as the criteria for convergence.

3.2.8   Grid sensitivity study

Grid sensitive study has been carried out for all the configurations to identify the optimum number of grid elements. Figure 3.17a depicts the grid sensitivity analysis for base case (without purge). Different mesh sizes selected for baseline case are 2.95 million, 3.16 million, 3.37 million, 3.58 million, 3.79 million and 3.95 million. No significant difference has been observed in the results with 3.58 million, 3.79 million and 3.95 million. Based on the results obtained, 3.58 million mesh elements are chosen for the base case domain. At 3.58 million mesh elements, difference in the mass averaged total pressure loss coefficient with the finest mesh (3.95 million) is merely 0.36%. Different grid sizes selected for BCP configuration are 3.05 million, 3.26 million, 3.44 million, 3.59 million, 3.74 million, 3.89 million and 4.05 million (Figure 3.17b). Mesh size

of 3.74 million is chosen as the optimum mesh that can provide accurate results with minimum resource requirements (for example, minimum computational time). Increasing the mesh size above 3.74 million elements does not have any significant change in the flow parameter. In comparison to the finest mesh size (4.05 million), the variation in the mass averaged total pressure loss coefficient ($\overline{\overline{C_{po}}}$) of optimum mesh selected is 0.11%. For the profiled endwall configurations the same optimum mesh size of 3.58 million (without purge) and 3.74 million (with purge) are adopted for computational analysis. Similarly optimum mesh size selected for purge with cylinder configuration is 4.13 million.

3.2.9 Verification and Validation

The validation of numerical results has been carried out for the base case (BC), base case with cylinder in stagnation line (BC-STW) and base case with purge (BCp). The parameters considered for the validation are static pressure coefficient (C_{ps}) distribution around the blade midspan at different inlet velocities (14.42 m/s, 19.23 m/s, 24.04 m/s), pitch averaged exit yaw angle deviation at 127% C_{ax} (for BC, BC-STW & BCp) and local total pressure loss coefficient (C_{po}) distribution at 127% C_{ax} (for BC, BC-STW & BCp). The Static pressure coefficient (C_{ps}) is obtained from the static pressure ports provided at blade midspan. Pitch averaged yaw angle deviation and total pressure loss coefficient are obtained from measurements through the five hole probe at cascade exit. The static pressure and total pressure loss values are normalized with respect to inlet dynamic pressure to obtain the C_{ps} (Eq. 3.21) and C_{po} (Eq. 3.22) respectively. Figure 3.18a shows that static pressure coefficient predicted through numerical simulations are quantitatively and qualitatively matching well with the experimental results. Similarly the exit yaw angle deviation (Fig. 3.18b) and the total pressure loss coefficient (Fig. 3.19) are also compared with the experimental results.

$$C_{ps} = \frac{P_s}{0.5\rho_\infty U^2} \qquad (3.21)$$
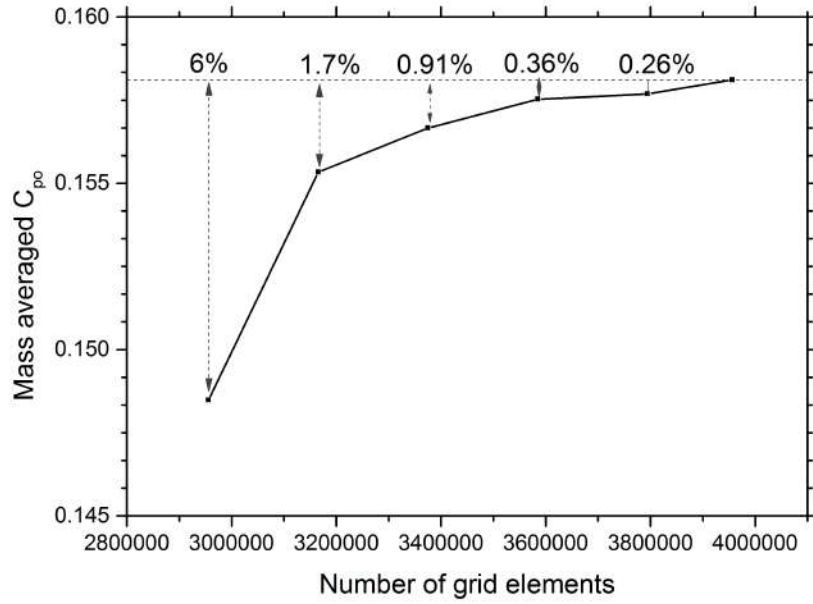
(a)
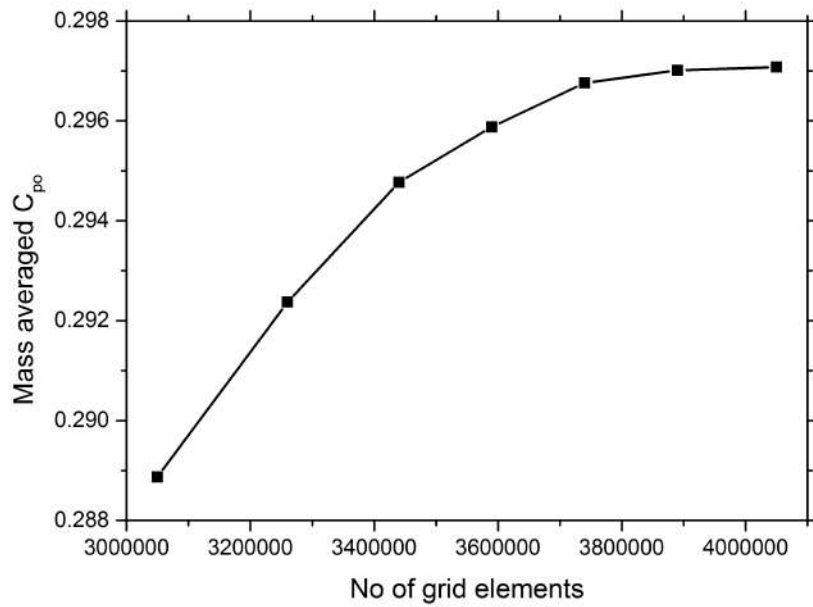
(b)

Figure 3.17: Grid Independence study for a) Base case without purge (BC) and b) Base case with purge (BCp).

$$C_{po} = \frac{\frac{m_\infty}{m_\infty + m_c}\overline{\overline{P_{t\infty}}} + \frac{m_c}{m_\infty + m_c}\overline{\overline{P_{tc}}} - P_t}{0.5\rho_\infty U^2} \qquad (3.22)$$

It is well understood that the total pressure loss coefficient values are the most crucial and difficult parameter to get a closer match with RANS simulations. Hence the local values of loss coefficient at 127% C_{ax} is plotted in the form of a contour and compared with the experimental results. The obvious exit loss regions such as endwall loss region, passage vortex and trailing edge wakes are observed in all figures (Figure 3.19). Near the hub endwall, the 5 hole probe is not able to capture the entire endwall loss region because of the distance between endwall and probe center at the first measurement point (1.6% of span). A better match is observed at majority of the regions including near the endwall. At loss core regions, numerical simulation is found to be slightly over-predicting (maximum deviation of 14.2% is noticed). However, a RANS simulation predicts the mean flow behavior with reasonable accuracy (Schobeiri *et al.* (2015); Marini and Girgis (2007); Aizon *et al.* (2013); Asghar *et al.* (2014); Ni (1982); NI and BOGOIAN (1989); Davis *et al.* (1996)) and it is very useful in predicting the overall performance analysis of the turbine blade.
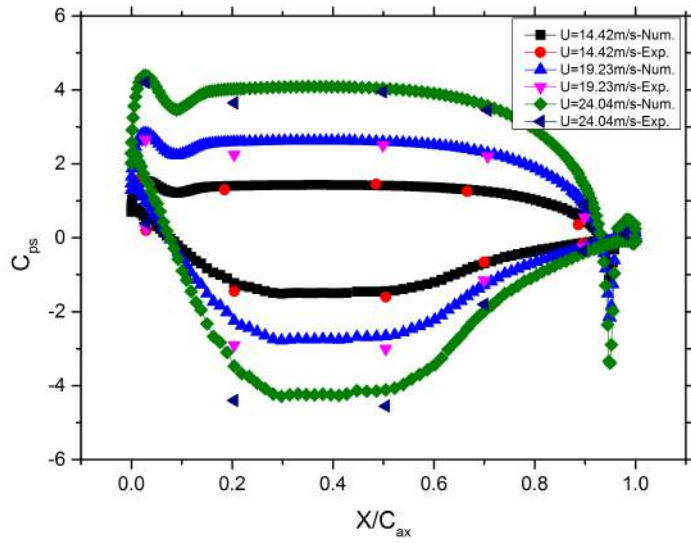
(a)
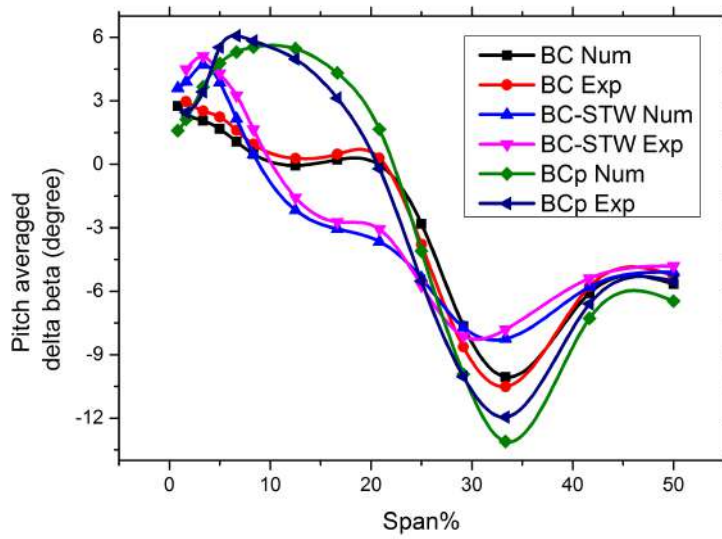
(b)

Figure 3.18: Validation of numerical results using Static pressure coefficient distribution at blade midspan (Base Case) and pitch averaged exit yaw angle deviation at 127% C_{ax} (Base case (BC), Base case-stagnation wake (BC-STW) & Base case with purge (BCp)).

(a) BC Experimental

(b) BC Numerical

(c) BC-STW Experimental

(d) BC-STW Numerical

(e) BCp Experimental
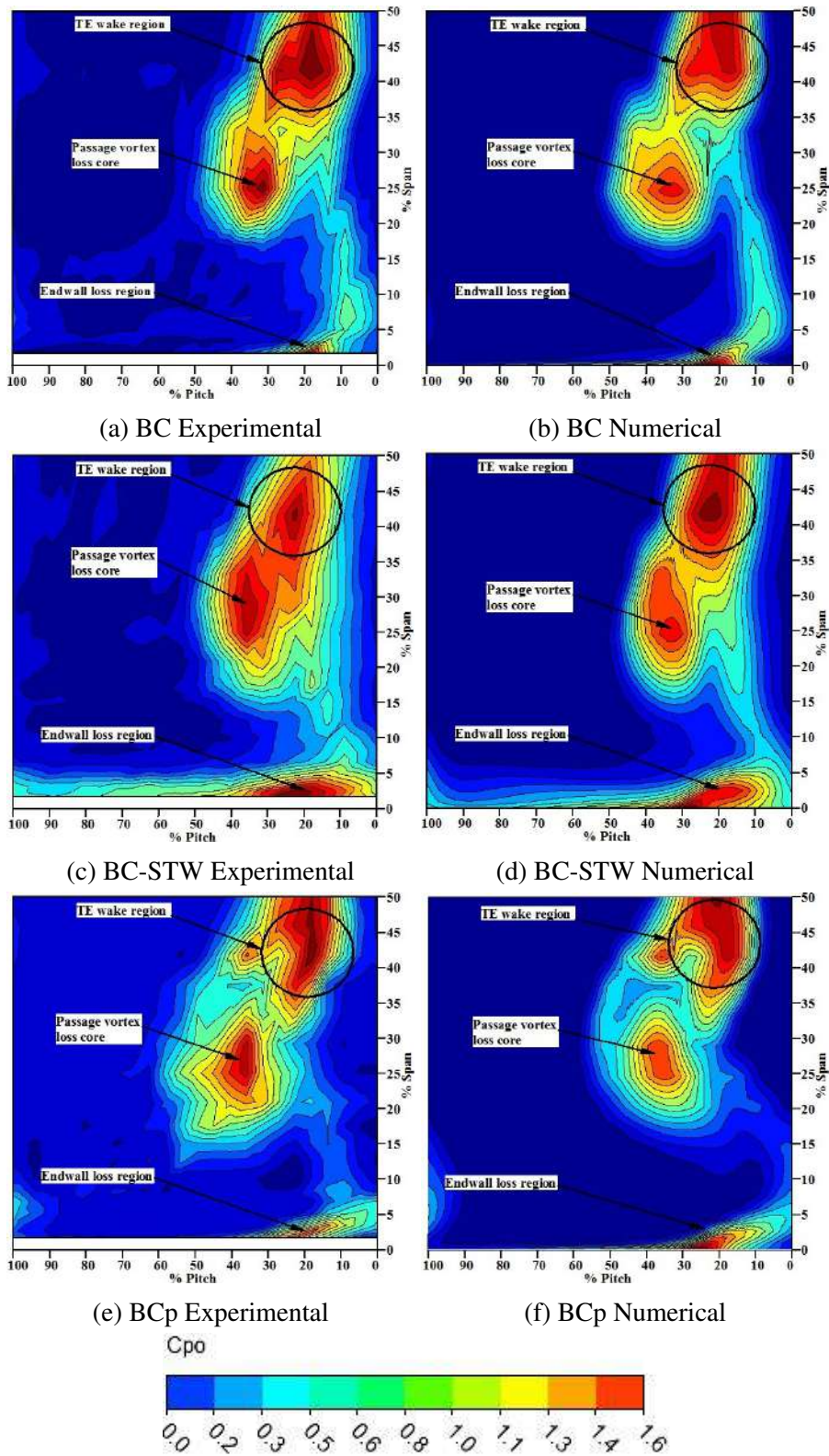
(f) BCp Numerical

Figure 3.19: Validation of numerical results using local total pressure loss coefficient at 127% C_{ax}.

CHAPTER 4

EFFECT OF VELOCITY RATIOS AND PURGE EJECTION ANGLES

4.1 Effect of velocity ratio

4.1.1 Overview

In the subsonic flow regime, density ratio has little impact on the final conclusive results. In this aspect, velocity ratio plays vital role and computational investigations are carried out to understand the effect of velocity ratio (M) on the flow characteristics and the film cooling effectiveness. The velocity ratio (M) is defined as the ratio of purge flow velocity (Uc) to the main stream velocity (U) (Rozati and Tafti 2007). The purge flow rate is increased gradually and the simulations are carried out for different values of M (0.2 to 1.0 in steps of 0.2). Accordingly, the blowing ratio (B = density ratio of the two streams (DR) x velocity ratio (M)) and pressure ratio (ratio of total pressure at coolant inlet ($P_t c$) to total pressure at mainstream inlet ($P_{t\infty}$) are also different for each of these simulations (Rezasoltani *et al.* 2014; Mensch and Thole 2014; Suryanarayanan *et al.* 2010). The typical values of blowing ratio (Table A.1) and pressure ratio (Table A.2) are provided in the appendix for reference.

4.1.2 Effect on total pressure loss coefficient

Figure 4.1 shows mass averaged total pressure loss coefficient ($\overline{\overline{C_{po}}}$) distribution within the blade passage along the axial direction (Eq. 4.1). At each axial location total pressure is mass averaged over the measuring plane and it accounts for total losses in the blade passage including the mixing effects of purge flow with mainstream flow. It is ob-

served that the loss coefficient is increased by 17.2% at the exit for $M = 0.2$ compared to the base case (BC). With an increase in the value of M, the rate of increase of loss coefficient also increases. This is evident from the variation of slope of each curve. The disturbances created by the purge flow is quite evident from these plots. Near to trailing edge (TE) mixing of passage vortex with trailing edge wake regions makes the flow more disturbed which leads to a rapid increase in the loss coefficient particularly after 90% C_{ax}. The percentage variation of $\overline{\overline{C_{po}}}$ with increasing velocity ratios at each axial locations inside the blade passage decreases upto $M = 0.6$ and then increases up to $M = 1.0$. The recirculation regions developed as a result of coolant lift-off from endwall may be the reason behind the increase in $\overline{\overline{C_{po}}}$ beyond $M = 0.6$.

$$\overline{\overline{C_{po}}} = \frac{\frac{m_{\infty}}{m_{\infty}+m_c}\overline{\overline{P_{t,\infty}}} + \frac{m_c}{m_{\infty}+m_c}\overline{\overline{P_{t,c}}} - \overline{\overline{P_t}}}{0.5\rho_{\infty}U^2} \tag{4.1}$$
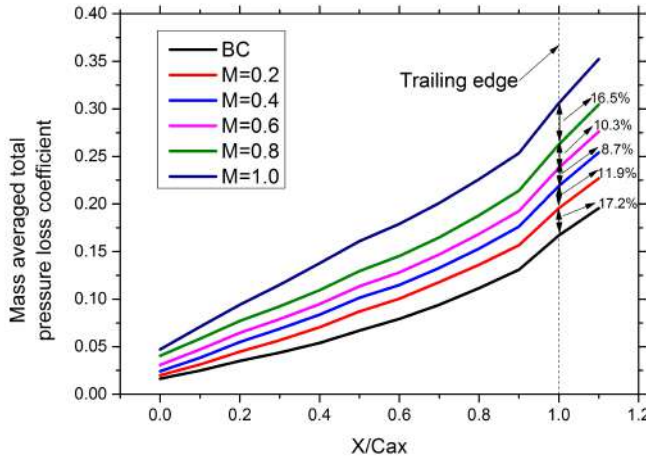
Figure 4.1: Variation of mass averaged total pressure loss coefficient ($\overline{\overline{C_{po}}}$) distribution along axial direction for 90^0 purge at different velocity ratios.

Pitch averaged total pressure loss coefficient ($\overline{C_{po}}$) distribution along the span of blade at 120% C_{ax} is calculated and is shown in Figure 4.2 (Eq. 4.2). The loss coefficient is evaluated from the hub endwall to full span of blade. Total five loss regions are recognized and mentioned as endwall loss regions at hub and shroud (regions 1 & 5),

passage vortex (PV) loss region at hub and shroud (regions 2 & 4) and counter vortex (CV) loss region (region 3). Both passage vortex and counter vortex loss core regions shifted tangentially with increasing velocity ratio. Ligrani *et al.* (2017) pointed out the passage vortex as pressure side leg of horseshoe vortex (HSV), traversed from pressure to suction side of the blade as a result of boundary layer cross flow (BLc). Counter vortex loss core is the suction side leg of HSV dragged into the near by blade passage with opposite rotational direction as of passage vortex. It is observed that the value of loss coefficients rapidly decreases from the endwall up to a span of 10 %. The purge flow cases are showing lower losses than base case near the endwall. Inside the boundary layer more energized coolant ejecting out of purge slot eventually leads to lower losses compared to base case (Cui and Tucker (2017)). For purge flow cases the losses significantly increases after a spanwise distance of 15%. The peak loss coefficient occurs at 20% to 40% of span and from then onwards there is a decrease in the value of loss coefficient. Beyond $M = 0.6$, passage vortex peak values (region 2) changes drastically both tangentially and radially due to the generation of stronger secondary vortices inside the blade passage at high velocity ratios. This indicates that more efficient velocity ratio lies below 0.6. Scattered peak values at region 4 shows the impact of purge flow above blade midspan. These variations suggest that the presence of purge flow has enhanced the passage vortex eventhough it decreases the losses near the endwall.

$$\overline{C_{po}} = \frac{\frac{m_\infty}{m_\infty + m_c}\overline{\overline{P_{t,\infty}}} + \frac{m_c}{m_\infty + m_c}\overline{\overline{P_{t,c}}} - \overline{P_t}}{0.5\rho_\infty U^2} \tag{4.2}$$

4.1.3 Effect on Underturning and Overturning

Underturning and overturning has a significant effect on the total secondary flow losses. For better understanding pictorial representation of underturning and overturning has been provided in the appendix (Figure A.1). Reduction in both underturning and overturning improves performance of successive blade rows. Figure 4.3 shows the pitch averaged yaw angle deviation for 90^0 purge case along the spanwise direction at 120%
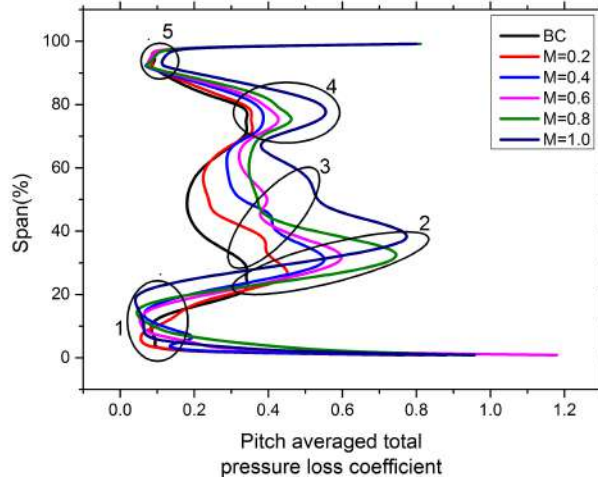
Figure 4.2: Variation of pitch averaged total pressure loss coefficient ($\overline{C_{po}}$) distribution at 120% C_{ax} for 90^0 purge at different velocity ratios.

C_{ax}. The exit yaw angle (β) shows significant variation within the boundary layer. The peak values of overturning lies between 10% and 25% of span. The change in yaw angle is caused by the large variation in the tangential velocity. At the endwall, for all velocity ratios, the deviation of yaw angle from designed angle has increased significantly. For base case, near to endwall, yaw angle is reducing up to a span of 6% and then starts increasing upto 10%. On the contrary, for purge cases, this reducing trend gradually changes and yaw angle starts increasing within the boundary layer. Boundary layer cross flow might be the reason behind rapid changes in the endwall region. At higher velocity ratio ($M = 1.0$), the flow is underturned and increases steadily upto a span of 25%. However, farther away from the endwall, large variation in yaw angle has been observed. The base case exhibits underturning throughout the span except near the endwalls. Whereas the purge flow cases show significant overturning upto a span of 35%, before they enter into underturning at 90% of span. The percentage variation of peak values of underturning from design angle for velocity ratios of 0.6, 0.8, 1.0 are 17.5%, 18.6%, 25.26% respectively.
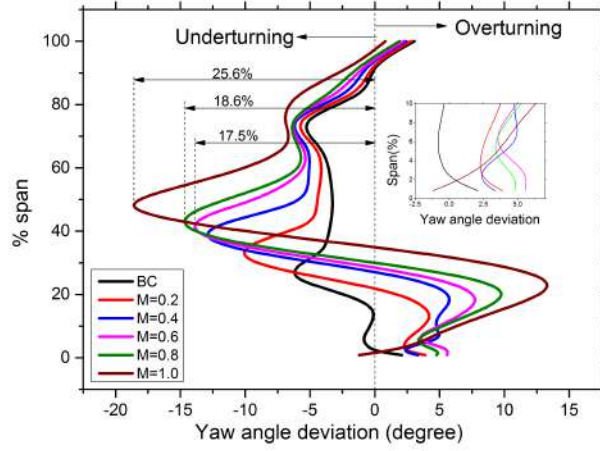
Figure 4.3: Distribution of pitch averaged exit flow angle deviation along the span at 120% C_{ax} for 90^0 purge at different velocity ratios.

4.1.4 Effect on Film Cooling Effectiveness

Figure 4.4 shows the direct comparison of pitch averaged film cooling effectiveness (FCE) for 90^0 purge with different velocity ratios. Pitch averaging of the effectiveness along the blade passage starts at the blade leading edge and ends at trailing edge. The definition of FCE has been given in Equation 4.3

$$\eta = \frac{T_\infty - T_{aw}}{T_\infty - T_c} \tag{4.3}$$

where T_∞, T_{aw} and T_c represents mainstream inlet temperature, adiabatic wall tempera-ture and coolant inlet temperature respectively. Near the blade leading edge, at positions X/C_{ax} = 0.0, for velocity ratios 0.2 and 0.4, cooling effectiveness shows comparatively minimum and almost similar values. At these low velocity ratios, a portion of the low momentum fluid is pushed inward into the purge slot by the mainstream flow. Also low momentum coolant is unable to overcome the cross flow and it is quickly carried away by secondary vortices. Beyond 0.4 velocity ratio, the cooling effectiveness is quite high. This indicates that coolant ejecting out of the upstream slot is able to overcome the cross flow and can provide better protection around the blade leading edge near the

63

endwall. $M = 1.0$ exhibits a drastic reduction in Film cooling effectiveness (FCE) distribution between $0.1 < X/Cax < 0.6$ because of the coolant lift-off from the endwall. Due to stronger recirculation regions, coolant detached from the endwall, flows along the suction surface along with passage vortex and reattaches at endwall near trailing edge. Compared to other velocity ratios, $M = 1.0$ is showing higher FCE at upstream of trailing edge because of the coolant reattachment.
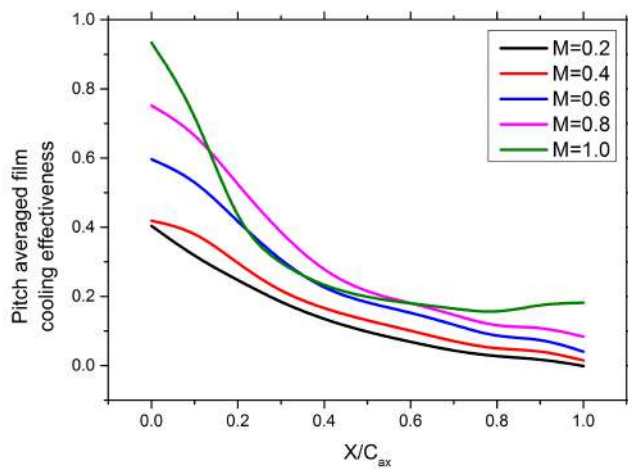
Figure 4.4: Pitch averaged film cooling effectiveness for 90^0 purge at different velocity ratios.

FCE contours (Figure 4.5) over the blade suction surface reveals the presence of coolant at different velocity ratios for 90^0 purge. Direction of mainstream is from leading edge to trailing edge (right to left) (Figure 4.5a). With the increase in the velocity ratio coolant start detaching from the endwall and climbs up the suction surface along with the passage vortex. Coolant lifting from the endwall can be confirmed by observing 3-D streamlines that have originated from the purge inlet. At low velocity ratio, number of streamlines attached to the blade surface is less. With the increase in the M value, FCE distribution over the blade surface increases gradually and a sudden increase is observed for $M = 1$. The unexpected increase in the FCE distribution for $M = 1$ (Figure 4.5e) is due to the entrainment of coolant separated from the endwall by the passage vortex. At the blade leading edge, horseshoe vortex is getting more strengthened by
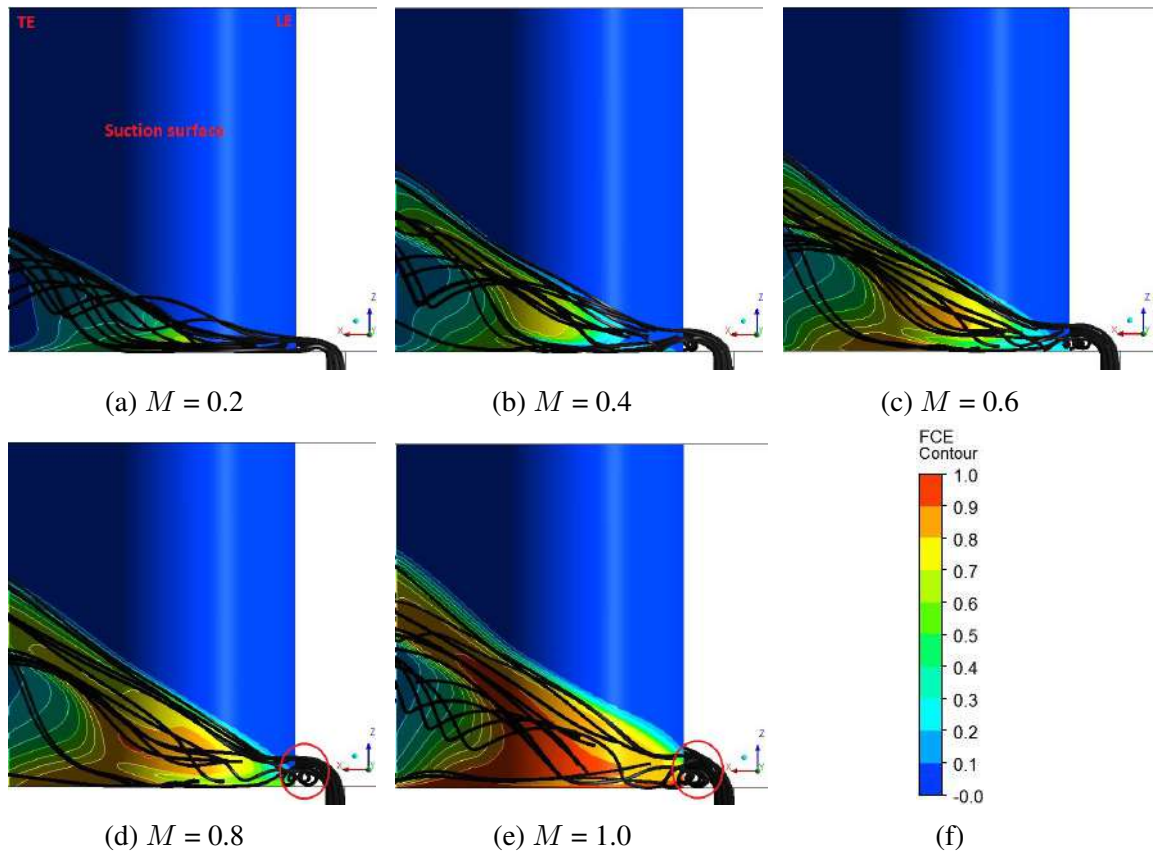
Figure 4.5: Film cooling effectiveness distribution on blade suction surface along with 3-D streamlines for 90^0 purge at different velocity ratios.

the increase in the velocity ratio (Figure 4.5d & 4.5e). Strong vortex formation at leading edge is the reason behind the additional secondary losses and further reduction in endwall protection.

4.2 Effect of purge ejection angles

4.2.1 Overview

This section consider the effects of geometric parameters of purge slot on passage secondary loss generation. In an effort to reduce losses, different purge flow ejection angles (90^0, 75^0, 60^0, 45^0, 30^0) are studied (Figure 4.6). Various flow parameters such as total pressure loss coefficient, exit yaw angle and film cooling effectiveness are analyzed.

(a) $\alpha = 30^0$ (b) $\alpha = 45^0$

(c) $\alpha = 60^0$ (d) $\alpha = 75^0$

(e) $\alpha = 90^0$
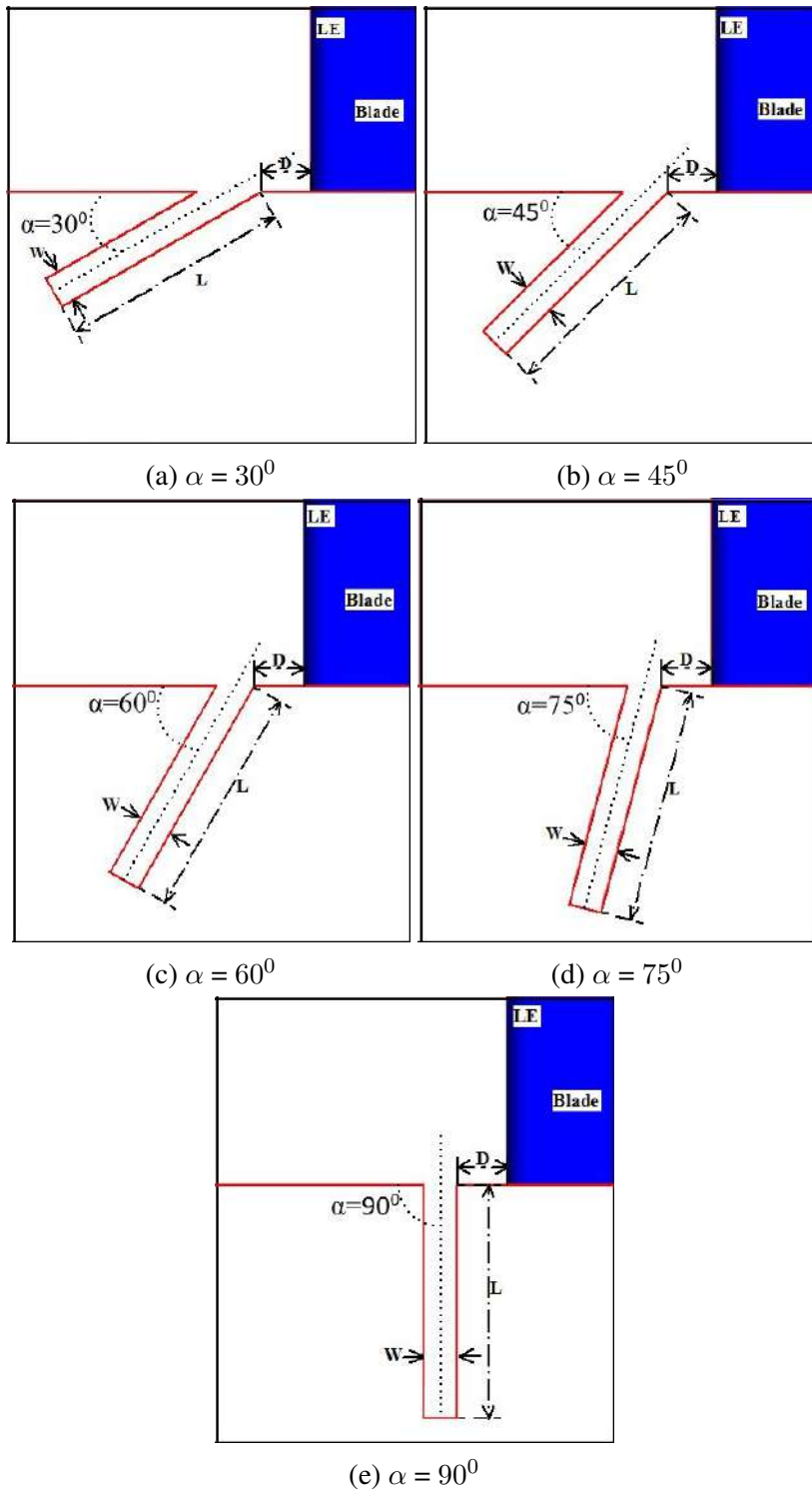
Figure 4.6: Configuration of different purge ejection angles.

4.2.2 Effect on total pressure loss coefficient

Axial distribution of mass averaged total pressure loss coefficient ($\overline{\overline{C_{po}}}$) for different purge angles from 30% C_{ax} to 110% C_{ax} are shown in Figure 4.7. The distribution of $\overline{\overline{C_{po}}}$ for all cases shows qualitative similarity. In purge cases, slope of $\overline{\overline{C_{po}}}$ curve increases after 90% C_{ax}, indicating higher losses at downstream of blade passage compared to base case. After 90% C_{ax} base case shows slight increase in losses. Comparing all purge cases, 30^0 and 45^0 ejection angles exhibit smaller losses, indicating more favorable configuration lies between these two purge angles. On the other hand, higher losses are observed for the 90^0 purge, all through out the domain. At 50% C_{ax}, value of $\overline{\overline{C_{po}}}$ is slightly higher (shown in circle) for 90^0 purge compared to preceding angle 75^0, indicating the presence of additional recirculation regions emerged as a result of coolant lift-off. The percentage variation of 90^0 purge with base case at 50% C_{ax} is 88.6%. Meanwhile percentage variation for 30^0 and 45^0 purges are 23.8% and 35.5% respectively.
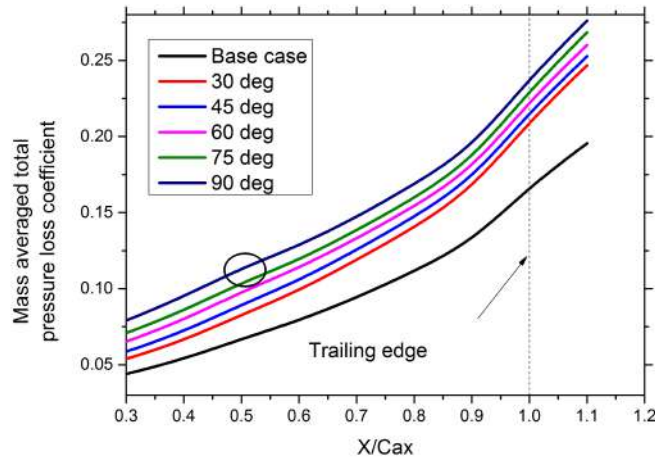
Figure 4.7: Variation of mass averaged total pressure loss coefficient ($\overline{\overline{C_{po}}}$) distribution along axial direction for various purge angles at $M = 0.6$.

Figure 4.8 explains the variation of pitch averaged total pressure loss coefficient ($\overline{C_{po}}$) for different purge ejection angles at $M = 0.6$. As observed in Figure 4.2, here

also various loss core regions are identified. They are endwall loss core regions, passage vortex loss core regions and counter vortex loss core regions. Reduction of purge ejection angle from 90^0 to 30^0 has specific influence over the shifting of passage vortex and counter vortex loss core regions. Both loss core has shifted tangentially and radially. Compared to 30^0 & 45^0, 90^0 ejection angle has shown 35.9% & 15.9% increase in passage vortex loss core. For ejection angle of 90^0, 75^0 & 60^0 counter vortex loss cores peak values are well below the passage vortex loss cores. However for 30^0 ejection angle, the purge flow reduces the passage vortex loss core peak value by 16.8% compared to counter vortex loss core. No significant effects of peak variations are observed for 45^0 ejection angle. Reduction in the ejection angle has provided higher momentum to the boundary layer fluid which inturn leads to the reduction of secondary losses. For higher purge ejection angles, the purge flow behaves like a jet ejecting out of the surface rather than forming thin film over the endwall and blade surfaces. The separation of purge flow from the endwall surfaces will cause higher drag. The higher drag by the purge flow will cause the mainstream boundary layer shifted upwards and additional roll up vortices are generated at the blade leading edge. As a result, the axial momentum possessed by the incoming boundary layer will be reduced and it becomes more vulnerable to the cross passage pressure gradient. The entrainment of more low momentum boundary layer fluid due to strong cross passage pressure gradient, will leads to the formation of strong passage vortex for higher ejection angles.

4.2.3 Effect on Underturning and Overturning

Figure 4.9 shows the variation of yaw angle deviation at 120% C_{ax} for different purge ejection angles at velocity ratio of 0.6. In general all ejection angles follow the same trend. Comparing the different ejection angles, profound variations are visible below 35% span. As stated earlier, purge flow has shifted both underturning and overturning values drastically compared to base case. Variations in ejection angles do not have much influence over under turning. Eventhough the trend remains similar, increase in ejection angle from 30^0 to 90^0 have enhanced the peak values of overturning steadily. Compared
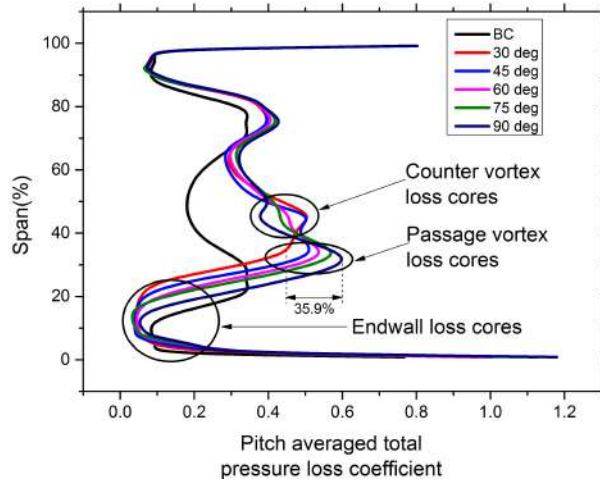
Figure 4.8: Variation of pitch averaged total pressure loss coefficient ($\overline{C_{po}}$) distribution at 120% C_{ax} for various purge angles at $M = 0.6$.

to 90^0 purge, 30^0 and 45^0 are effective in reducing the overturning and making it more close to design angle.
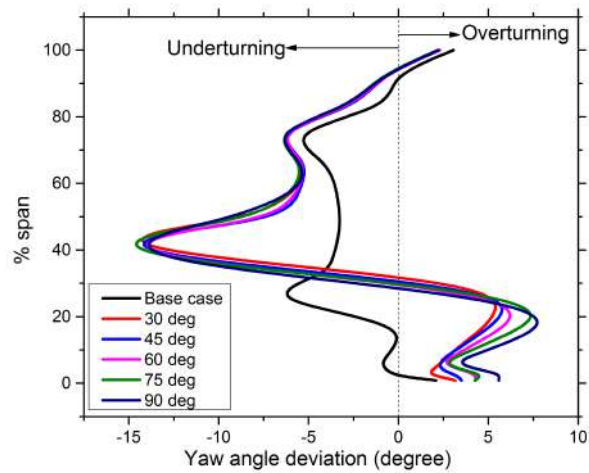
Figure 4.9: Pitch averaged yaw angle deviation at 120% C_{ax} for various purge angles at $M = 0.6$.
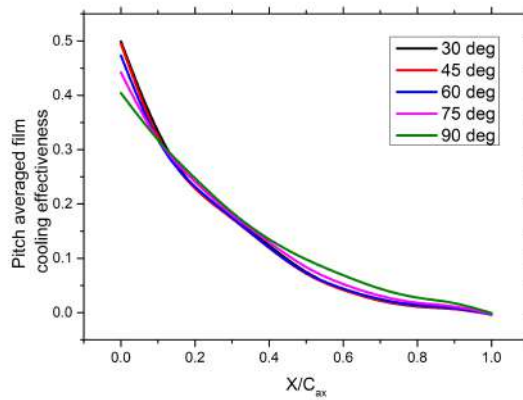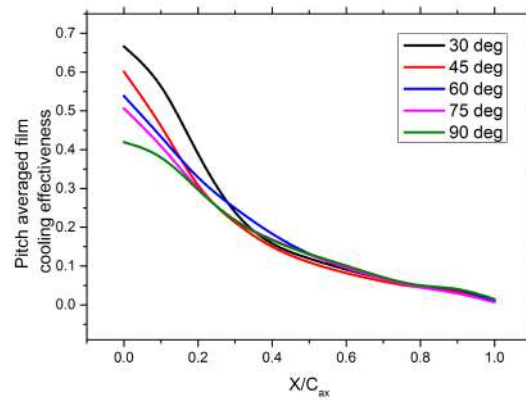
(a) $M = 0.2$ (b) $M = 0.4$
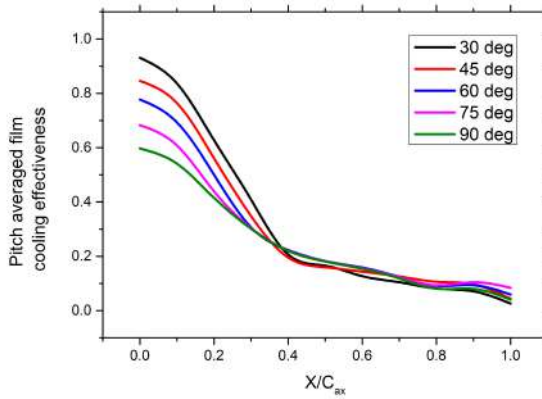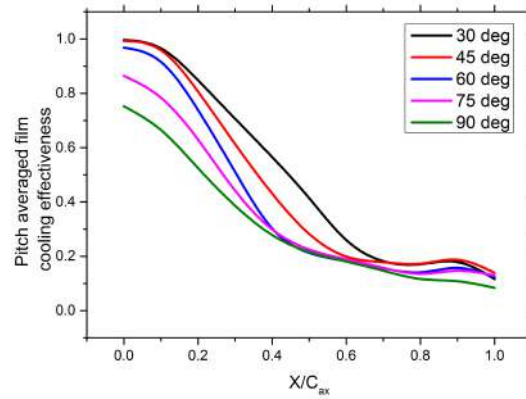
(c) $M = 0.6$ (d) $M = 0.8$

Figure 4.10: Axial distribution of pitch averaged film cooling effectiveness on the end-wall.

4.2.4 Effect on Film Cooling Effectiveness

Figure 4.10 presents pitch averaged film cooling effectiveness distributions on the end-wall at different velocity ratios (M) and purge ejection angles (α). The coolant ejecting out of purge slot can provide better endwall protection for $X/C_{ax} < 0.5$. Endwall FCE distribution can be enhanced by increasing the velocity ratio. However, effectiveness of film cooling is limited beyond $X/C_{ax} = 0.5$. The influence of purge ejection angle (α) is not significant for lower velocity ratio ($M = 0.2$). At higher velocity ratio, FCE is a major function of purge angle. At low velocity ratios purge air flows closer to endwall

rather than climbing up along suction surface. Film cooling effectiveness increases with decrease in α. The increase of pitch averaged FCE at leading edge is as high as 55.8% when the purge ejection angle α is reduced from 90^0 to 30^0 for $M = 0.6$. Also reduction of α to 45^0 from 90^0 has increased the FCE by 41.7% for velocity ratio of 0.6.

Figure 4.11 shows the distribution of film cooling effectiveness on the hub endwall. For all cases, highest film cooling effectiveness value is observed over the upstream region, particularly around the leading edge of the blade. Cross flow from pressure side to suction side leads to the entrainment of coolant leaving most of the pressure side of blade surface unprotected. Secondary vortices near the endwall are responsible for the cross flow. Interaction between purge flow and mainstream flow enhances the mixing losses and also strengthens the horseshoe vortex, which leads to the reduction of film cooling effectiveness. At higher velocity ratios as well as lower ejection angles, the purge flow provides a better thermal protection on the endwall. At higher velocity ratio, fluid momentum will be more to overcome the effect of passage cross flow. However simultaneous secondary loss generation with the increase in the velocity ratio cannot be neglected. In addition, for velocity ratio less than 0.4, coolant distribution at the purge slot outlet is nonuniform, especially when $M = 0.2$, coolant ejection from the slot is limited due to the back pressure from the blade leading edge (Figure 4.11-a).

(a) $M = 0.2$

(b) $M = 0.4$

(c) $M = 0.6$

(d) $M = 0.8$

(e) $M = 1.0$
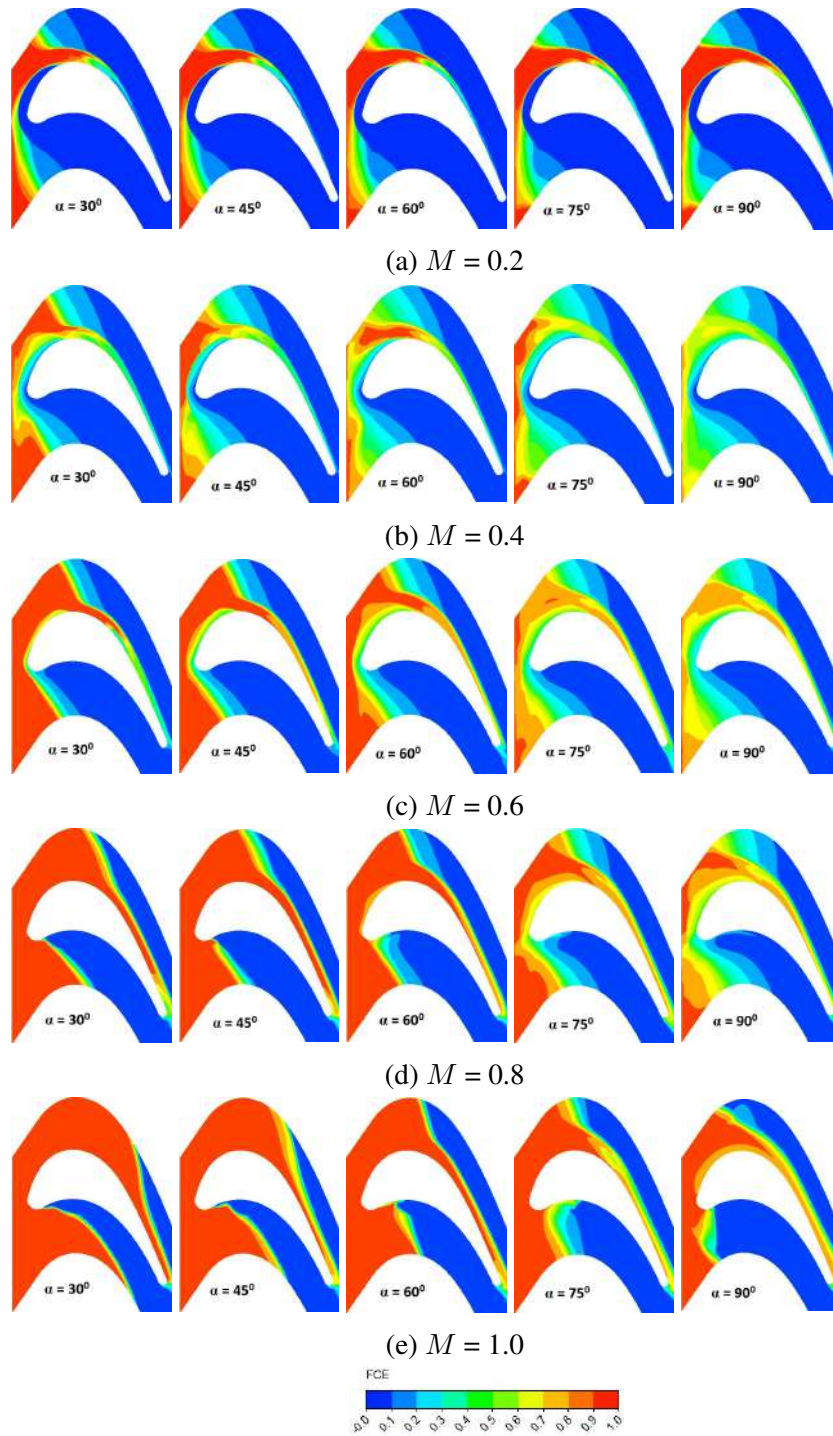
Figure 4.11: Film cooling effectiveness distribution on the endwall.

Mass averaged total pressure loss coefficient based on different velocity ratios and purge ejection angles are shown in Figure 4.12. Total pressure loss coefficient for all cases are measured at 120% C_{ax}. Mass averaged C_{po} at the inlet of base case is considered as reference value. Effects of α is negligible for low velocity ratios (0.2 & 0.4). At higher velocity ratios significant changes are observed and losses are amplified for $\alpha > 45^0$. With the increase in the velocity ratio, slope of the loss curves increases continuously for ejection angle greater than 45^0. However for $\alpha = 45^0$ and $M = 0.6$, growth rate of losses has been diminished compared to higher purge ejection angles and velocity ratios. In general, it can be observed that lowering the purge ejection angle is advantageous to minimize the aerodynamic losses and to enhance the FCE distribution. However, incorporating very small angle is difficult and the practical difficulty may eclipse over the aerodynamic benefits derived from it.
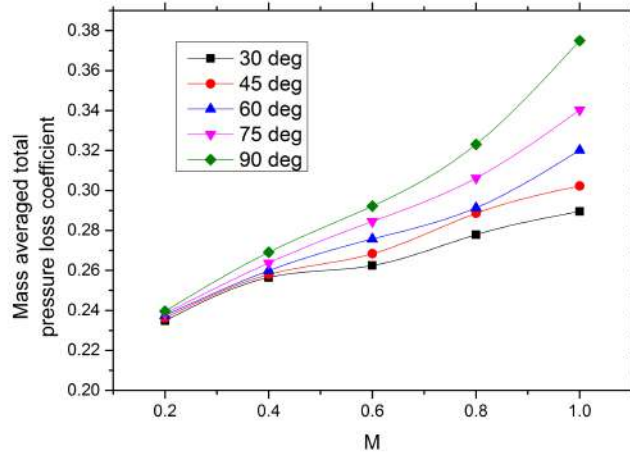
Figure 4.12: Mass averaged total pressure loss coefficient distribution at 120% C_{ax} for different purge ejection angles and velocity ratios.

4.3   Summary

- Blockage effects generated by the perpendicular purge ejection ($\alpha = 90^0$) has strengthened the boundary layer cross flow.

- At low velocity ratios, low momentum purge is pushed inward into the purge slot due to the stagnation pressure upstream of blade leading edge.

- At higher velocity ratios, enhanced mixing between both purge and mainstream, modified the exit yaw angle distribution all through out the spanwise direction.

- The entrainment of purge flow by the passage vortex at low velocity ratios and lift-off tendency exhibited by the purge flow at higher velocity ratios have shown detrimental effects on the endwall film cooling effectiveness (FCE).

- From the above inference, velocity ratio of 0.6 has been chosen as the favorable M value for further analysis. With the objective of reducing secondary losses, different ejection angles are investigated at $M = 0.6$.

- Variation in the purge ejection angles has profound influence only over the endwall region. The midspan region remains unaffected.

- At higher ejection angles, increased discrepancy existing between the velocity vectors of purge and mainstream flow caused higher aerodynamic losses.

- At lower ejection angles, the higher momentum generated inside the boundary layer has resulted in the reduced boundary layer cross flow as well as enhanced endwall FCE distribution.

- Lower ejection angle of 45^0 and velocity ratio of 0.6 have been considered as the beneficial design parameters for the further investigation.

CHAPTER 5

INTERACTION OF UPSTREAM WAKES WITH PURGE FLOW

5.1 Overview

The flow modifications caused by the interaction of upstream wake with the purge flow are analyzed in this section. This interaction leads to the formation of additional vortices in the blade passage. These additional vortices are identified and their influence on the blade loading, exit yaw angle and turbulence kinetic energy are discussed in the initial part of this section. At the latter part, detailed unsteady analysis are shown to understand the transient behavior of these vortices and their influence on the loss coefficients. Upstream wakes are generated by keeping circular cylinders of diameter 6 mm, which represents the blade trailing edge, at 35% C_{ax} upstream of blade leading edge (LE) at four different locations obtained by dividing the blade passage into quarters (Choi *et al.* (2017); Wright *et al.* (2009)). Position of the cylinders with respect to stagnation line of mainstream flow are shown in Figure 5.1 and these configurations are named as Suction side wake (SSW), Midpassage wake (MW), Pressure side wake(PSW) and Stagnation wake(STW).

5.2 Effect on the general flow behavior

In order to understand the flow modifications caused by the interaction of upstream wake and purge flow, iso-surface Q-criterion (superimposed with streamwise vorticity distribution) inside the blade passage is analyzed (Figure 5.2). Rotational direction of suction side leg (SSL) and pressure side leg (PSL) of horseshoe vortex can be identified as clockwise (positive sense of rotation) and counter clockwise (negative sense of ro-
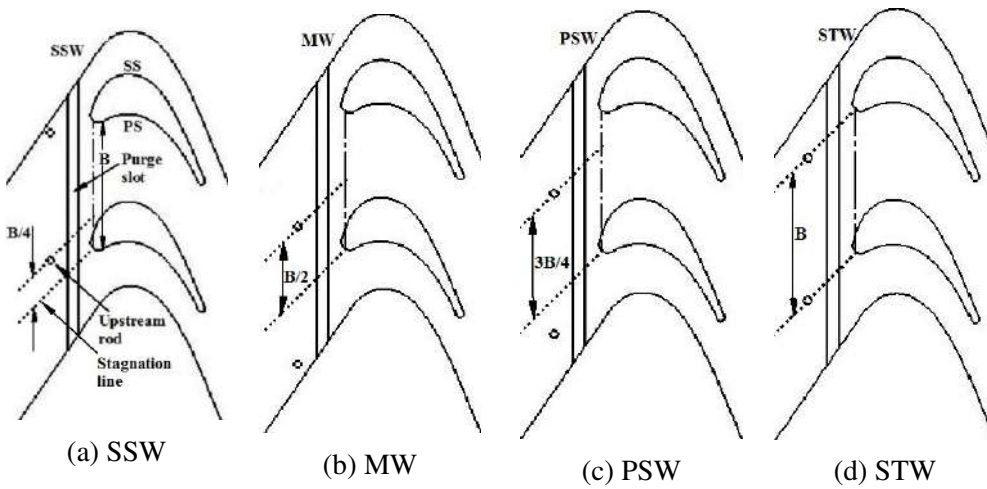
Figure 5.1: Computational domain with upstream cylinders at different locations.

tation) respectively. Apart from the horseshoe vortex (HSV) and passage vortex (PV), four more additional vortices can be identified. They are pressure surface vortex (PSv), pressure side corner vortex (PScv), purge vortex (Vp) and cylinder vortex (Vc). It is observed that for all the configurations the purge vortex (Vp) is dragged towards the suction surface due to the transverse pressure gradient. In SSW configuration, cylinder vortex (Vc) merges with suction side leg vortex (SSL) just downstream of leading edge and later both combines with the pressure side leg vortex (PSL) at the aft part of suction surface (Figure 5.2c). As the cylinder position shifts towards the pressure side, the strength of Vc increases. When the cylinder is near the stagnation region of the blade (Figure 5.2f), the cylinder vortex (Vc) pushes the PSL towards the pressure surface making the flow more attached to the pressure surface near to endwall. The formation of pressure surface vortex (PSv) may be attributed to the increased spanwise pressure gradient caused by the purge flow. The spanwise pressure gradient causes the rolling up of low momentum fluid inside the pressure side bubble (PSB) to generate the PSv. Detailed explanation of PSB and PSv formations are given in Chapter 6. In STW configuration, cylinder wakes (Vc) suppresses the pressure side bubble formation which results in the reduction of spanwise pressure gradient over the pressure surface and leads to the upward movement of PSv (Figure 5.2f).

76

(a) Base case

(b) 45 deg purge

(c) Suction side wake

(d) Midpassage wake

(e) Pressure side wake

(f) Stagnation wake
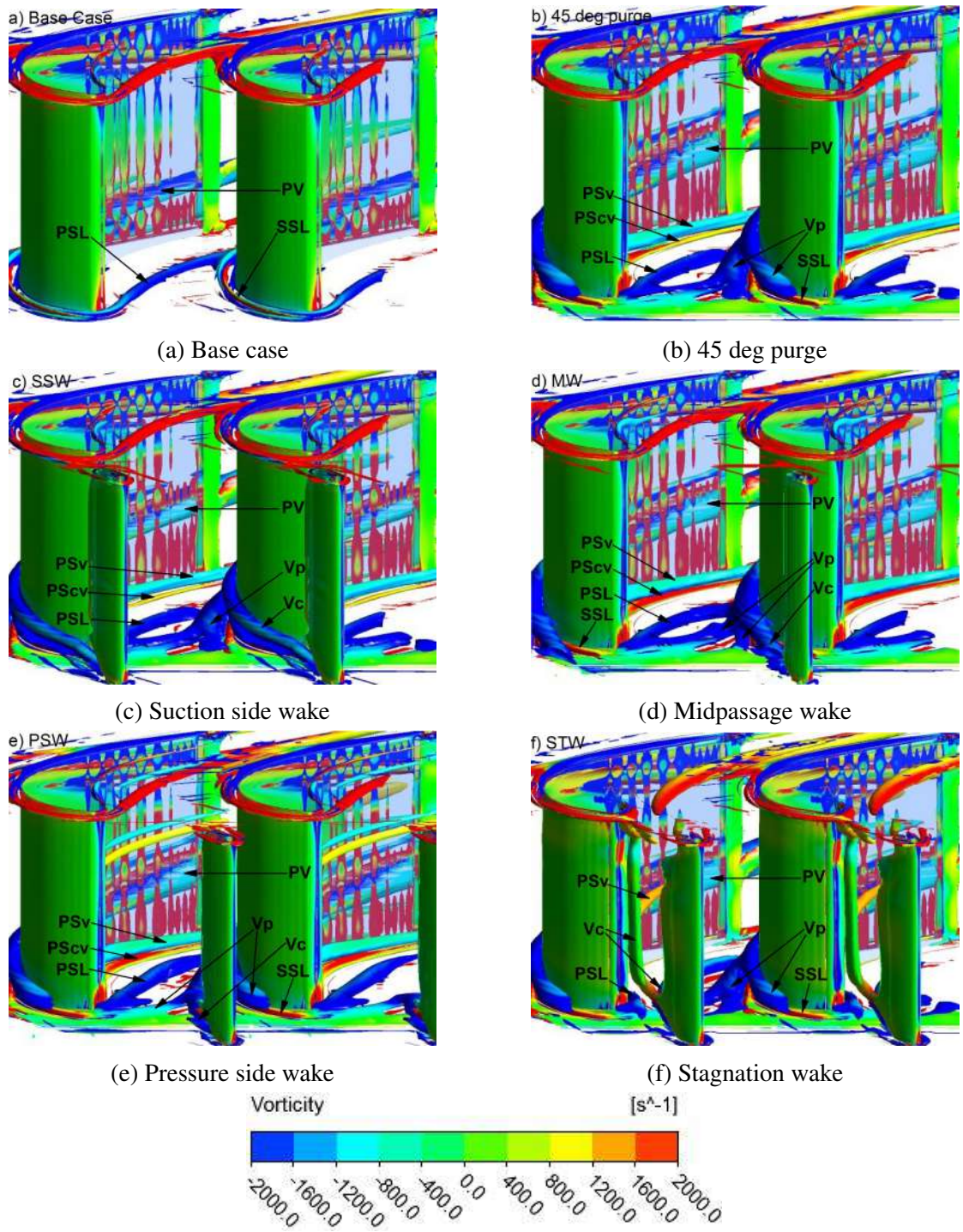
Figure 5.2: Leading edge vortex formations for different configurations using Q criterion.

5.3   Effect on the blade loading

In order to understand the effect of upstream wake and purge flow on blade load-ing, the static pressure coefficient (C_{ps}) has been plotted at 4.1% and 50% span (Eq. 5.1).   The results have been presented along normalized axial chord (X/C_{ax}) for all the configurations.   At midspan strong acceleration on the suction side of the blade is responsible for the rapidly decreasing value of C_{ps} till X/C_{ax} = 0.3 (Figure 5.3a). Further to this location, the static pressure coefficient remains relatively constant until X/C_{ax} = 0.5. This trend is common for all the configurations except for STW. It can be seen the static pressure coefficient droops significantly down on blade suction surface ($0.2 < X/C_{ax} < 0.6$) for STW configuration. The cylinder wakes in STW configura-tion, come in direct contact with the blade leading edge, splits into smaller filaments and move along the pressure and suction surfaces. This is evident from the unsteady anal-ysis detailed in section 5.5. On the other hand, for other configurations, cylinder wake does not interact directly with the leading edge and hence no splitting up into smaller filaments. Instead, they move towards the suctions surface, under the action of passage cross flow, and slows down the flow near the suction surface. The static pressure coeffi-cients for different cylinder positions near the endwall are shown in Figure 5.3b. Static pressure reduction for purge cases remains constant and uniform until X/C_{ax} = 0.15 on suction surface. After that significant variation of C_{ps} value can be observed for base case and purge cases upto blade midpassage. At X/C_{ax} = 0.22, for base case, there is a minimum value of C_{ps} = -1.5, as compared with the 45^0 purge case, showing just a small region having a minimum value of C_{ps} = -0.1. This is due to the strong recirculation zones generated by the deceleration of endwall boundary layer by the purge flow. For all configurations, varying C_{ps} values are obtained in between $0.2 < X/C_{ax} < 0.5$ on the suction surface because of more disturbed secondary flows formed at the merging point of additional vortices (Vp and Vc) with the SSL. As cylinder shifts from suction to pressure side, the static pressure distribution over suction surface has decreased and the merging point of Vp and Vc with SSL has shifted downstream. Blade loading co-

(a) C_{ps} Midspan

(b) C_{ps} Endwall

(c) Span averaged blade loading coefficient (C_b)
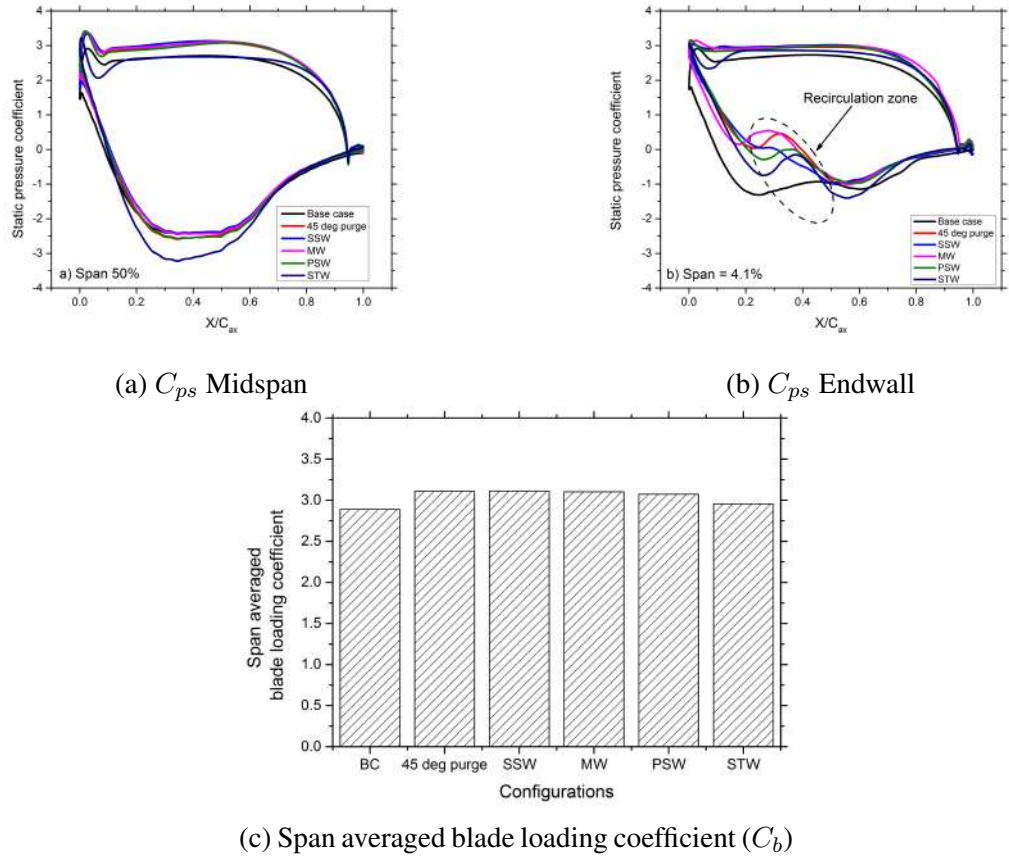
Figure 5.3: Static pressure coefficient (C_{ps}) and span averaged blade loading coefficient (C_b) on the blade surface for different configurations.

efficient (C_b) of all configurations are quantitatively compared in Figure 5.3c. C_b is calculated as the difference between the static pressure coefficients (C_{ps}) over blade pressure surface and suction surface. Compared to base case C_b has marginal increase by the introduction of purge flow as well as upstream wakes. Comparing the upstream wake configurations, STW configuration exhibits the lowest C_b because of the slight but considerable reduction of C_{ps} (Figure 5.3a) throughout the pressure surface due to the presence of cylinder vortices. In rest of the upstream wake configurations the cylinder vortices are carried towards the suction surface by the cross flow without disturbing the pressure surface.

$$C_{ps} = \frac{P_s}{0.5\rho_\infty U^2} \qquad\qquad (5.1)$$

The influence of upstream cylinder positions on blade exit yaw angle is explained in Figure 5.4. The yaw angle deviation is calculated with respect to exit blade angle and is plotted as contours on a streamwise plane at 120% C_{ax}. As explained by Qi *et al.* (2012) secondary flow vortices exist as closed concentric contours above and below and as series of circumferential contours. Passage vortex (PV) exhibits overturning near the endwall and underturning towards midspan. It is observed that at the downstream of the trailing edge, the PV occupies a smaller area, roughly between 15% and 30% of span, for the base case (Figure 5.4a). The introduction of purge flow enhances the passage vortex which grows in size, both in the spanwise and pitchwise direction. The overturning near the endwall is enhanced by additional purge vortex (Vp) (Figure 5.4b). STW configuration exhibits maximum overturning and underturning at about 20% and 40% span respectively. However PSW and STW configurations are capable of pushing secondary flow more close to the endwall. The passage vortex shifts 4% towards the endwall in STW and PSW configurations compared to MW configuration (Figure 5.4e & 5.4f). The stretching of the passage vortex causes an increase in the underturning towards the midpassage region for STW configuration. This is due to the increased interaction of the cylinder vortices with the pressure surface of the blade.

5.4 Analysis through limiting streamlines

The formation of additional flow structures by purge flow and upstream cylinders significantly influence the turbulent kinetic energy (TKE) distribution near to endwall. Figure 5.5 shows the turbulent kinetic energy distribution superimposed with limiting streamlines for base case and purge flow with different upstream cylinder locations. Horseshoe vortex and additional upstream vortices generated by purge flow (Vp) are the major causes for high turbulent kinetic energy at fore part of the blade passage. The low momentum purge flow acts as a blockage to the mainstream flow and difference in the
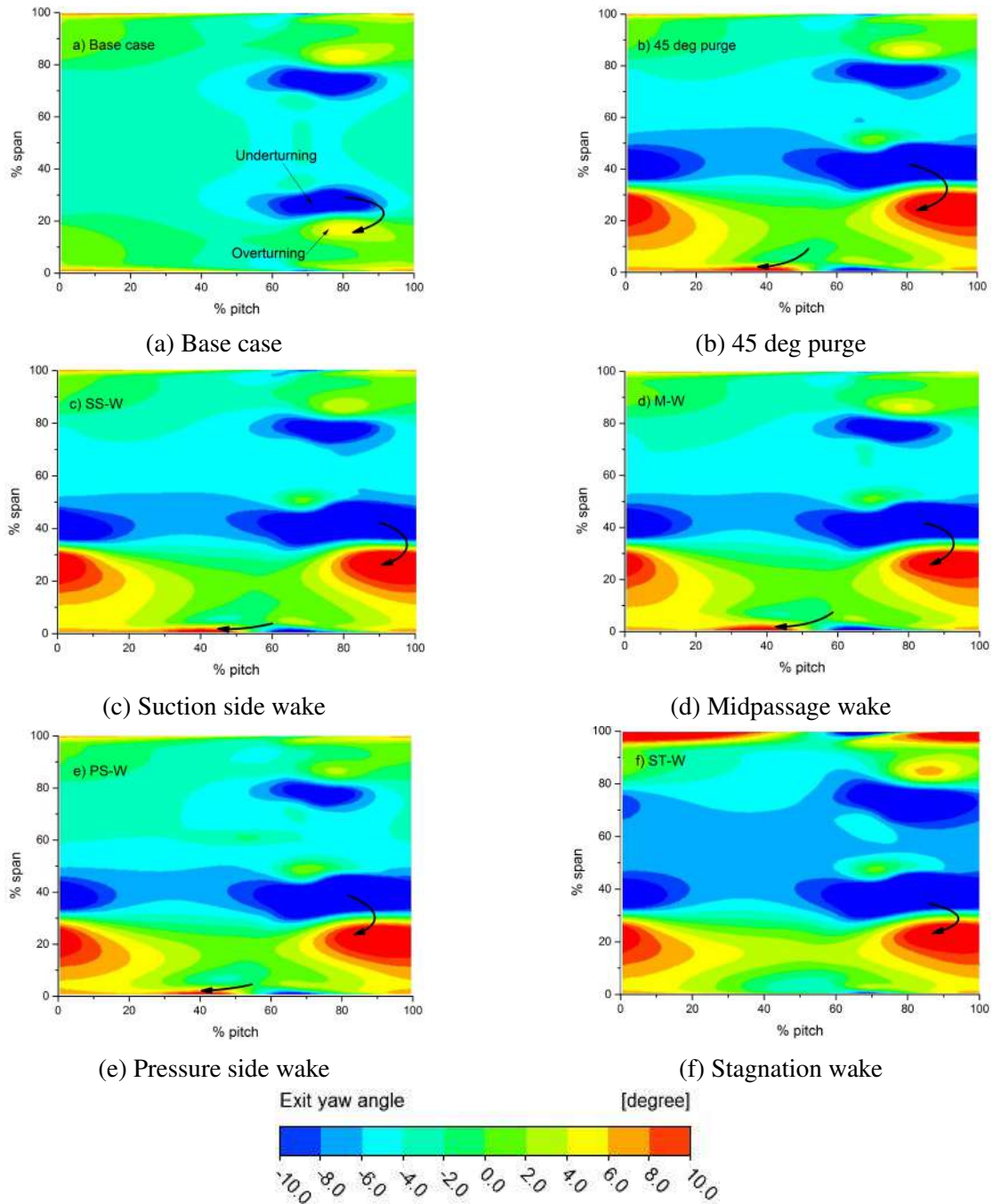
Figure 5.4: Exit yaw angle deviation at 120% C_{ax} for different configurations.

velocity magnitudes between both streams shifted the saddle point (S1) towards suction side from leading edge (Figure 5.5b). Attachment point (A1) of passage cross flow on suction surface is pulled upstream by the additional roll-up vortices generated by purge

flow (Figure 5.5b). In SSW configuration, purge flow drags the endwall boundary layer partially into the purge slot which stimulates the turbulent mixing near the pressure surface (shown in circle, near pressure surface - Figure 5.5c). At the same time fluid ejecting out of the purge slot near suction surface accelerates along the suction surface just downstream of blade leading edge (shown in circle, near suction surface Figure 5.5c). In MW configuration significant TKE reduction is observed at the upstream of the blade passage (shown in circle) due to the interaction of high momentum mainstream with cylinder wakes (Figure 5.5d). At the merging point of pressure side leg with suction side of horseshoe vortex, an enhancement of turbulent kinetic energy is observed. This enhancement is not very prominent in the PSW configuration due to the flow acceleration generated by the cylinder wakes (Figure 5.5e). In STW configuration the cylinder wakes (Vc) along the pressure surface, dominates the migration of pressure side leg towards suction side, reduces the TKE distribution along the pressure side-endwall junction which is evident from the limiting streamlines (Figure 5.5f). This results in the overall reduction of turbulent kinetic energy distribution over endwall.

FCE distribution over the endwall at velocity ratio of 0.6 for different cylinder locations are shown in Figure 5.6a. Considering upstream wakes, cylinder positions have much influence over the endwall FCE distribution. As explained earlier purge flow from upstream slot can effectively protect fore part of the blade passage. Purge flow ejected from the upstream slot is swept towards suction side by secondary vortices, leaving most of the rear passage unprotected. This cross flow phenomena is encouraged by the additional vortices generated by purge flow (Vp). However the cylinder vortex (Vc) generated in STW configuration provide high flow acceleration inside the blade passage and it keeps the flow more attached to the pressure surface. As a result coolant entrained by the cylinder vortex spread more towards pressure surface endwall junction and provides better cooling effectiveness at rear passage. This is more evident from the endwall surface streamlines explained in Figure 5.5f. Addition of upstream wakes has increased secondary losses within the blade passage. $\overline{\overline{C_{po}}}$ distribution within the blade passage for different cylinder positions are shown in Figure 5.6b. The slope of

(a) Base case

(b) 45 deg purge

(c) Suction side wake

(d) Midpassage wake

(e) Pressure side wake

(f) Stagnation wake
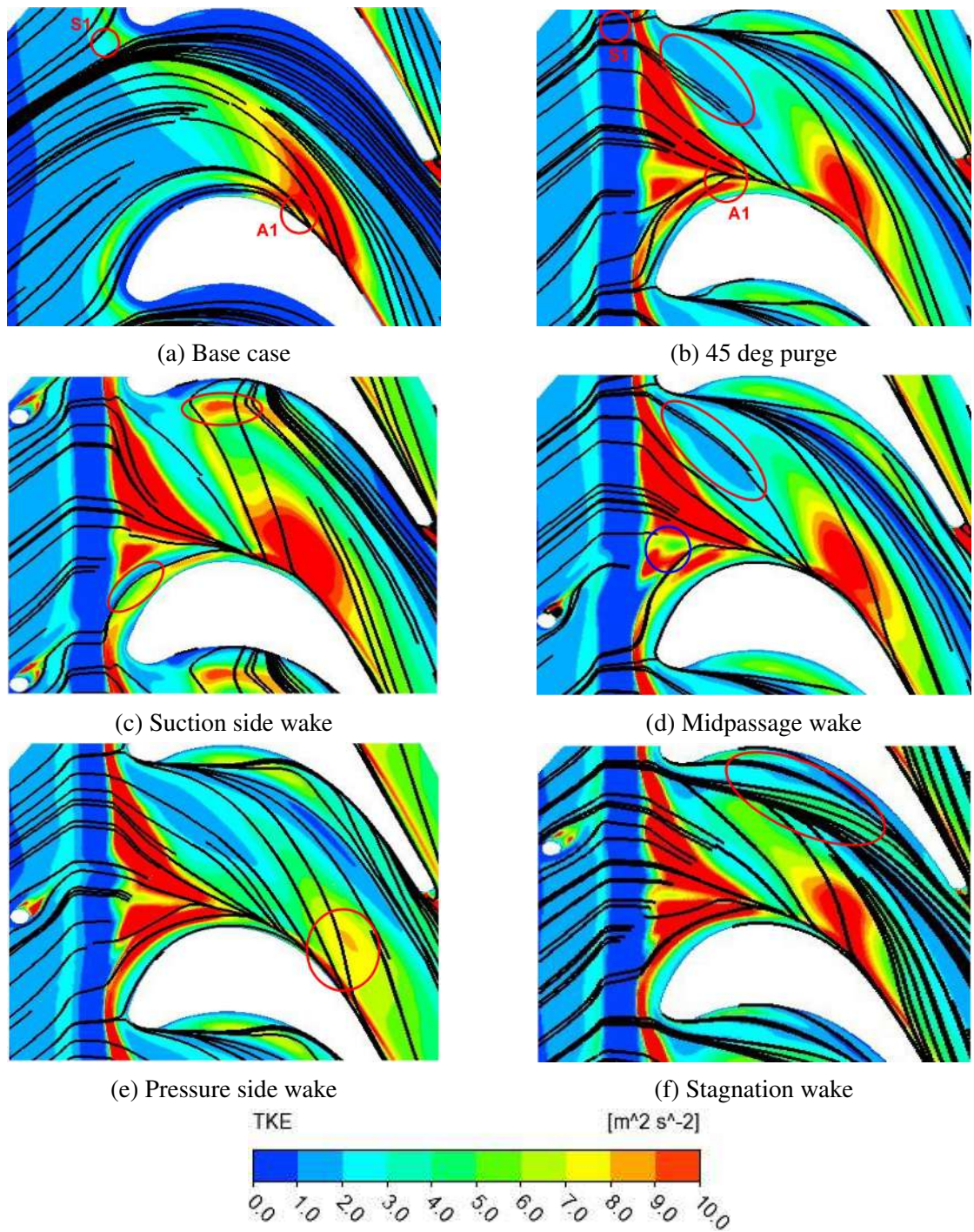
Figure 5.5: Turbulent kinetic energy distribution on endwall for various configurations.

each curve has a constant rate of increase upto 90% C_{ax}. Beyond 90% C_{ax} all configurations are exhibiting a gradual increment in the steepness due to the mixing of blade

wake region with passage secondary vortices. Compared to base case, the steepness of base case with purge (BCp) configuration seems to be diverging due to the enlargement of passage vortex while progressing towards the blade trailing edge. STW configuration shows higher losses all throughout the domain except at leading edge. In all other three cylinder configurations, the cylinder vortices do not directly interfere with the blade profile boundary layer. However in STW configuration, direct interaction of cylinder vortices with the blade surfaces generates higher secondary losses. At the leading edge horseshoe vortex developed at cylinder ends is not free to enlarge since it is kept upstream of leading edge. However it is more stronger than SSW and MW configuration at leading edge. Profound variations are observed for $\overline{C_{po}}$ distribution at 120% C_{ax} for different cylinder positions (Figure 5.6c). BCp and SSW configurations exhibits lower losses at the endwall. At the endwall, momentum of coolant ejecting out of the purge slot is strong enough to shatter the cylinder vortices. These results indicate that the relative position of cylinder with leading edge is of great importance. More details could be obtained through transient analysis.

5.5 Transient analysis of vortex formations at different cylinder locations

The transient analysis gives clear and more accurate information about the evolution and propagation of cylinder vortices, purge vortices and their interaction with the passage vortices. Figure 5.7 & 5.8 shows the unsteady vortex evolution inside the flow passage for two different time instances (τ = 0.0 & 0.5). Q-criterion along with streamwise vorticity has been calculated and plotted for two different configurations viz. STW and MW.

For STW configurations (Figure 5.7a) the upstream cylinder vortices are near to the leading edge and hence the back pressure from the leading edge, splits these cylinder vortices (Vc) into different small filaments. These filaments exhibit distinct dynamic behaviors inside the blade passage. The filaments which approaches the blade leading
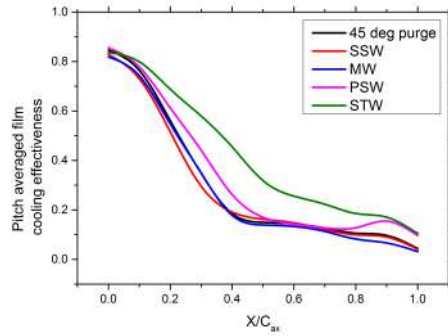
(a) FCE distribution
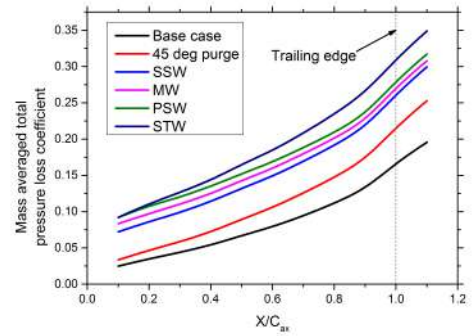
(b) Mass averaged C_{po} distribution
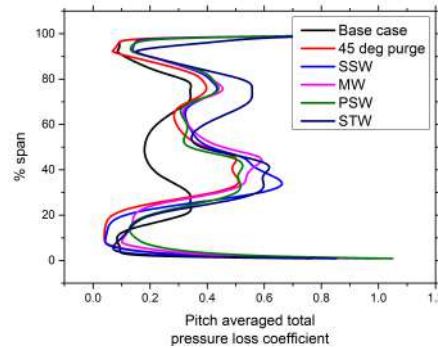
(c) Pitch averaged C_{po} distribution at 120% C_{ax}

Figure 5.6: Film cooling effectiveness (FCE) and total pressure loss coefficient (C_{po}) distribution for different cylinder positions.

edge, again splits into smaller vortices and move along the suction surface and pressure surface. These smaller filaments interacts with the low momentum fluid near the pressure surface boundary layer and generates more intense pressure surface vortices (PSv) that propagates to the downstream. The PSv exist as pairs of vortices having opposite rotational direction. As this PSv accumulates on the pressure surface, at first, pressure side leg of horseshoe vortex (PSL) is skewed and later bend near the pressure surface. At $\tau = 0.5$, more pressure surface vortices are observed which are merged together thereby increasing the complexity of passage flow aerodynamics at the exit. Apart from this vortex filaments, at endwall, the cylinder itself generates horseshoe vortex, which interacts with the PSL and leads to the alternate rolling of PSL from leading edge to trailing edge. The pressure surface vortices (PSv) having positive vorticity tends to
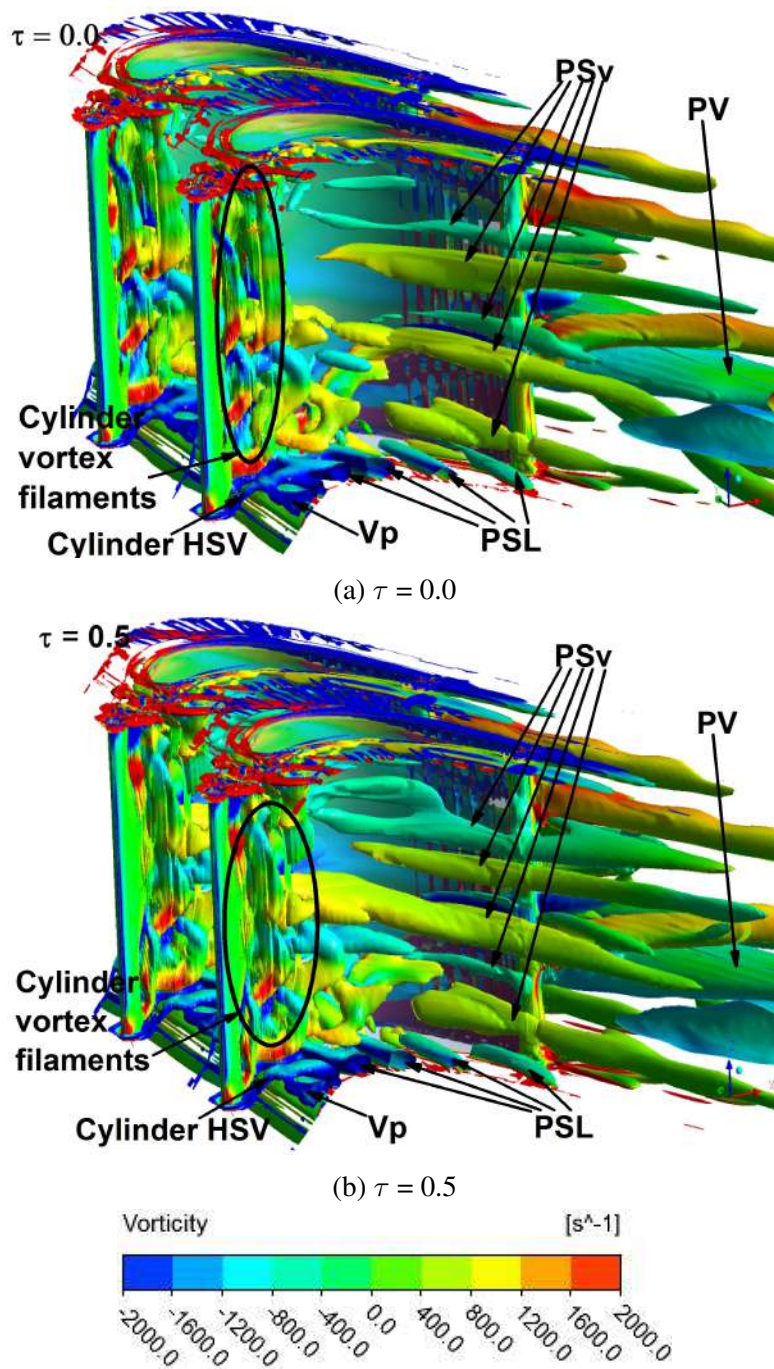
Figure 5.7: Q-criterion showing streamwise vorticity for Stagnation wake (STW) configuration at $\tau = 0.0$ & 0.5.

drag the PSL towards the pressure surface. As a result, tail of the PSL gets skewed and elongated compared to MW configuration. This accelerates the merging of pressure

surface corner vortex (PScv) with PSv.

On the contrary, the generations of these pressure surface vortices are limited near to the endwall for MW configuration (Figure 5.8). As the upstream wake moves to the midpassage region their interaction with the purge flow is quite notable in the MW configuration. The kinetic energy of the purge flow is less near the blade leading edge due to the upstream back pressure from the blade leading edge. This gives an added momentum to the purge flow at the midpassage region and it enters into the mainstream with high kinetic energy. As a result, it creates a blockade to the incoming cylinder vortices near the endwall for MW configuration. This causes the upper portion of the cylinder vortices to propagate faster than the lower portion and create a shearing action for the cylinder vortices along the streamwise direction. In MW configuration, apart from the Karman vortices, the horseshoe vortex generated by the cylinder are broken by the purge flow and both moves towards the suction surface under the influence of the pitchwise pressure gradient.

Secondary vortex interactions along the spanwise direction are explained using streamwise vorticity in Figure 5.9. In MW configuration, at midspan region, the Karman vortex street from the upstream cylinder propagates downstream keeping their opposite sense of rotation intact till they dissipate (shown as arrow line). The transport mechanisms exhibited by the alternate vortices are different and there is no direct interaction between them. However, in the region where they interact with the passage vortex, they get stretched and move towards the downstream direction (dashed circle-50% span). On the other hand, closer to the endwall, the Karman vortices are almost engulfed by the horseshoe vortex of the blade leading edge. The positive vortex is swallowed by the suction side leg of horseshoe vortex (SSL) and eventually moved towards the blade suction side. The negative cylinder vortex combines with the purge vortex, well inside the blade passage slightly away from the suction side. These vortex formations leads to the enhancement of passage vortex having negative vorticity at the blade exit.
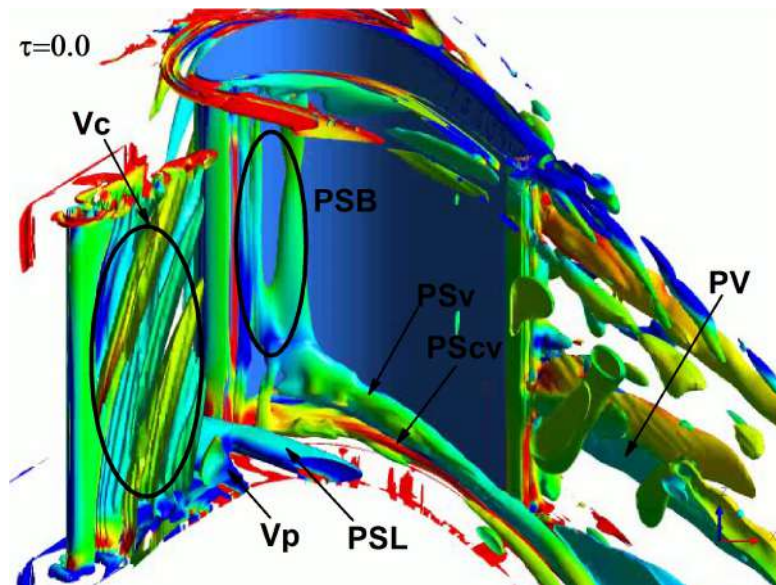
(a) $\tau = 0.0$
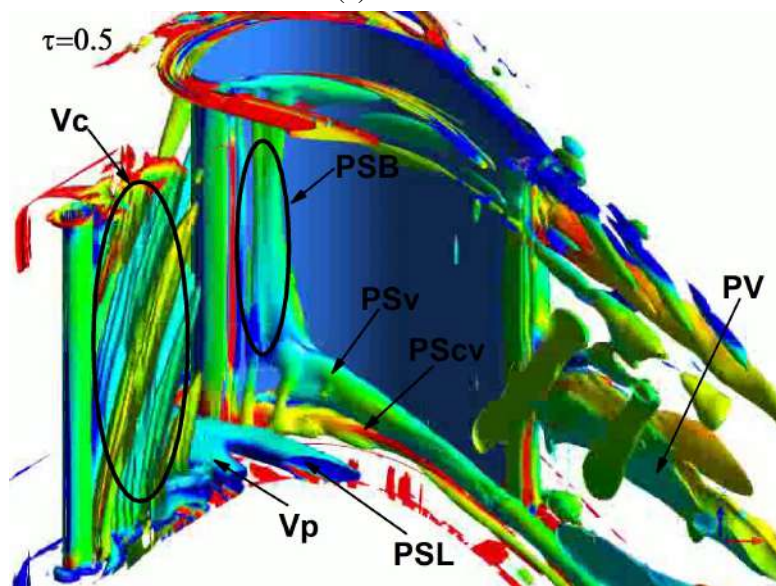
(b) $\tau = 0.5$
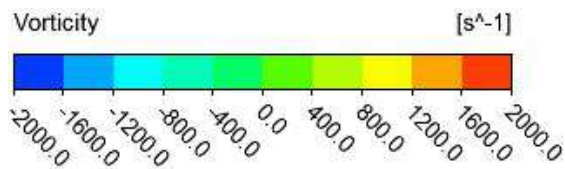
Figure 5.8: Q-criterion with streamwise vorticity for Midpassage wake (MW) configuration at $\tau = 0.0$ & 0.5.
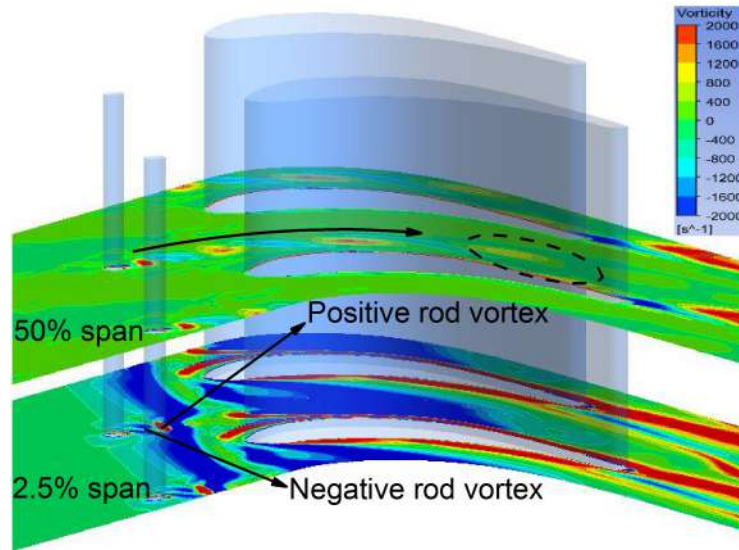
Figure 5.9: Spanwise planes vorticity contours for Midpassage wake (MW) configuration at $\tau = 0.0$.

The effect of unsteady vortices on the flow field aerodynamics characterized by total pressure loss coefficient (C_{po}) at different streamwise planes (10%, 45%, 80% & 120% C_{ax}) are shown in Figure 5.10 & 5.11 for two upstream cylinder positions. Frames at three instances are selected ($\tau = 0.0$, 0.8 and 1.5) for understanding the effect of unsteady vortex structures on the loss coefficient for STW configuration. Each total pressure loss core regions comprises of a pair of pressure surface vortices of opposite sense of rotation as explained in Figure 5.7.

At initial time step ($\tau = 0$), near to hub endwall, cylinder vortex filament (Figure 5.10a, below 40% span, at 10%, 45%, 80% C_{ax}) drags the tail of pressure side leg into it and rolls upwards forming endwall pressure surface vortex. Similarly towards midspan, after interacting with the blade leading edge, the cylinder vortices alone will cause the formation of midspan pressure surface vortex (Figure 5.10a, 10%, 45%, 80% C_{ax}). These vortices are detached from the pressure surface at different time-steps and it enhances the intensity of trailing edge vortices at the downstream. At the exit plane (120% C_{ax}) the pressure surface vortices interacts with endwall loss regions and trailing edge wake regions. The loss core regions corresponding to pressure surface vortices are highlighted at different spanwise locations. The frequency of formation of endwall
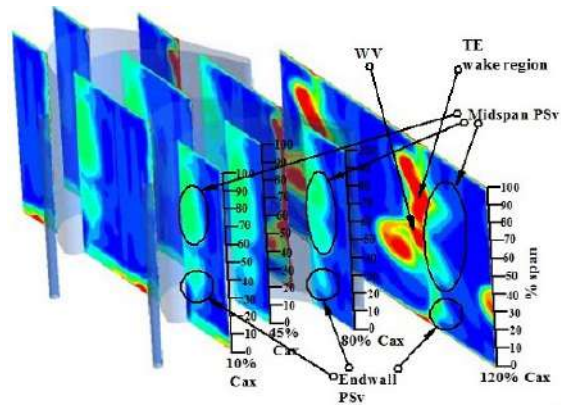
(a) $\tau = 0.0$
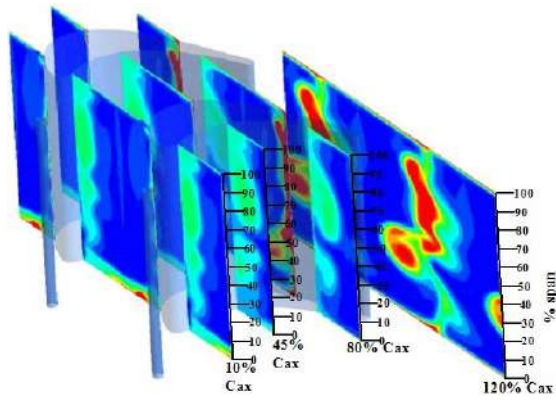
(b) $\tau = 0.8$
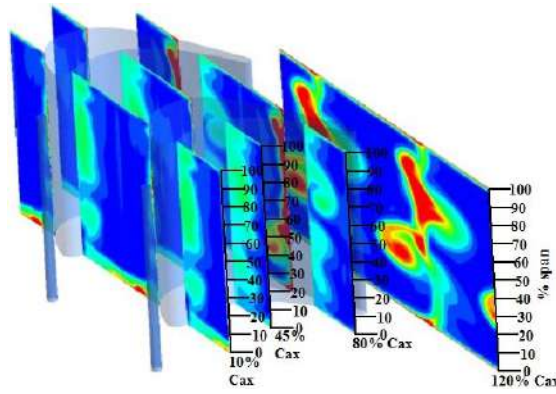
(c) $\tau = 1.5$
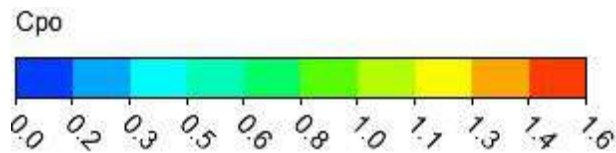
Figure 5.10: Total pressure loss coefficient (C_{po}) distribution at different streamwise planes for Stagnation wake (STW) configuration.

pressure surface vortices is higher than midspan pressure surface vortices. Endwall PSv separates from the pressure side (80% C_{ax} and 25% span) at $\tau = 0.8$ (Figure 5.10b), while midspan PSv will enlarge in size and shift spanwise direction and detach from pressure surface (80% C_{ax} and 70% span) at $\tau = 1.5$ (Figure 5.10c). At 120% C_{ax}, detached, endwall and midspan PSv from pressure surface merges with trailing edge wall vortex (WV) and trailing edge wake regions respectively (Figure 5.10c). This interaction increases the overall loss coefficient inside the blade passage and blade exit region.

The unsteady vortex evolution for MW configuration is obtained from two frames ($\tau = 0.0$ & 0.45) shown in Figure 5.11. In MW configurations, $\tau = 0.0$, the endwall portion of the cylinder vortices are dragged into the passage vortex by the boundary layer cross flow. As a result rather than trailing edge wake regions, the passage vortex loss core regions are much more intense in this case. The loss core region marked by black circle (Figure 5.11a a, 10% C_{ax}) shows the presence of cylinder vortex (Vc). It passes the blade passage independently not interfering with the blade surfaces except at endwall. This can be observed from planes located at 80% and 120% C_{ax} (18% and 30% span respectively). At $\tau = 0.45$, near to the hub region intervention of cylinder vortex with the passage vortex results in the squeezing of the same in spanwise direction by 3% at 80% C_{ax} and 5% at 120% C_{ax} (Figure 5.11b). Also the small loss core region appears strong but confined at the hub represents the pressure surface vortex residuals. Present numerical investigation confirms that rotational direction and lateral position of cylinder vortices plays a crucial role in the evolution of secondary flow within the blade passage and blade exit region for a low aspect ratio turbine blade.

5.6 Summary

To investigate the effects of upstream wakes, four cylinder configurations have been considered.

- Compared to base case, blockage effect caused by the purge flow has shifted the
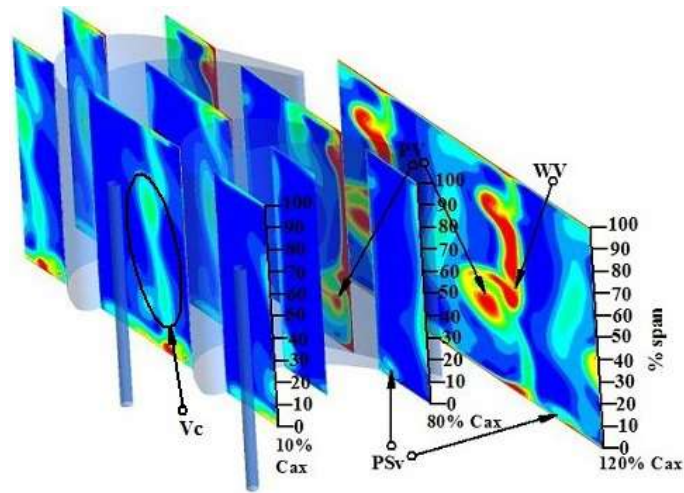
(a) $\tau = 0.0$
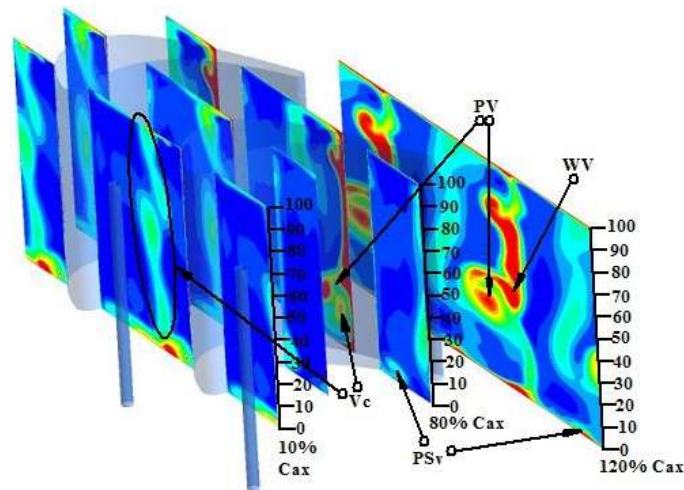
(b) $\tau = 0.45$
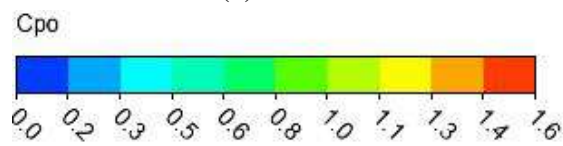
Figure 5.11: Total pressure loss coefficient (C_{po}) distribution at different streamwise planes for Midpassage wake (MW) configuration.

saddle point more towards blade suction side and the merging point of both legs of horseshoe vortex more upstream of the blade passage.

• For STW configuration, the splitting of cylinder vortices at blade leading edge and its interaction with blade pressure surface and suction surface has experienced slight reduction in the blade loading coefficient compared to other cylinder configurations.

- In all other configurations, the cylinder vortices are dragged towards the suction surface under the action of cross passage pressure gradient. This entrainment phenomena leads to high turbulent kinetic energy distribution at the merging point of both legs of horseshoe vortex near suction surface.

- In SSW configuration, partial entrainment of endwall boundary layer into the purge slot has instigated high turbulent mixing over the endwall region close to the pressure surface.

- Transient analysis reveals that, in STW configuration, the filament type vortices interacts with the pressure surface boundary layer fluid and generate pressure surface vortices (PSv). The PSv exist as pair of vortices having opposite sense of rotation.

- In STW configuration, frequency of formation of endwall pressure surface vortices are higher compared to midspan pressure surface vortices.

- The blockage effect generated by the purge flow caused the cylinder vortices in MW configuration to bend forward while progressing within the blade passage.

- In MW configuration, only the endwall region of the cylinder vortices is dragged into the passage vortex by the cross passage pressure gradient. The rest of the part propagates without interfering with the blade surfaces.

CHAPTER 6

EFFECT OF ENDWALL CONTOURING ON SECONDARY VORTEX FORMATION

6.1 Overview

The analysis made in this chapter aims to obtain a better understanding of secondary vortex formations within the blade passage in the presence of non-axisymmetric contoured endwalls. In the former part of this chapter, a detailed investigation of contoured endwalls in the absence of upstream purge flow has been conducted. By the introduction of purge flow, remarkable change in the secondary vortex structures are observed and these changes are explained in the latter part of this chapter. This chapter also covers, in detail, the transient nature of pressure side bubble (PSB) formation and its influence on the endwall boundary layer characteristics.

6.2 Endwall design

Three-dimensional contoured endwall designs are tested and compared with non contoured base configuration. The endwall profiling is implemented between 9% and 94% C_{ax}. The height distribution of contoured endwalls is shown in Figure 6.1. Three design variations are considered, and in all these configurations, a hump region (which locally accelerate the flow) and valley region (which locally decelerate the flow), are included for efficient redirection of the passage cross flow. Three different endwall contours are tested and they are named as EC1, EC2 and EC3 respectively. The first endwall contour (EC1) has a valley region near the pressure side of the blade and hump region near the suction surface. The maximum height of the hump and valley regions is 12mm. In EC2 configuration the location of hump and valley are reversed. The EC3 configuration is

having hump of height 7 mm near to pressure surface and a valley of 4 mm at mid-pitch which gradually decreases to zero at suction surface.

(a) BCp
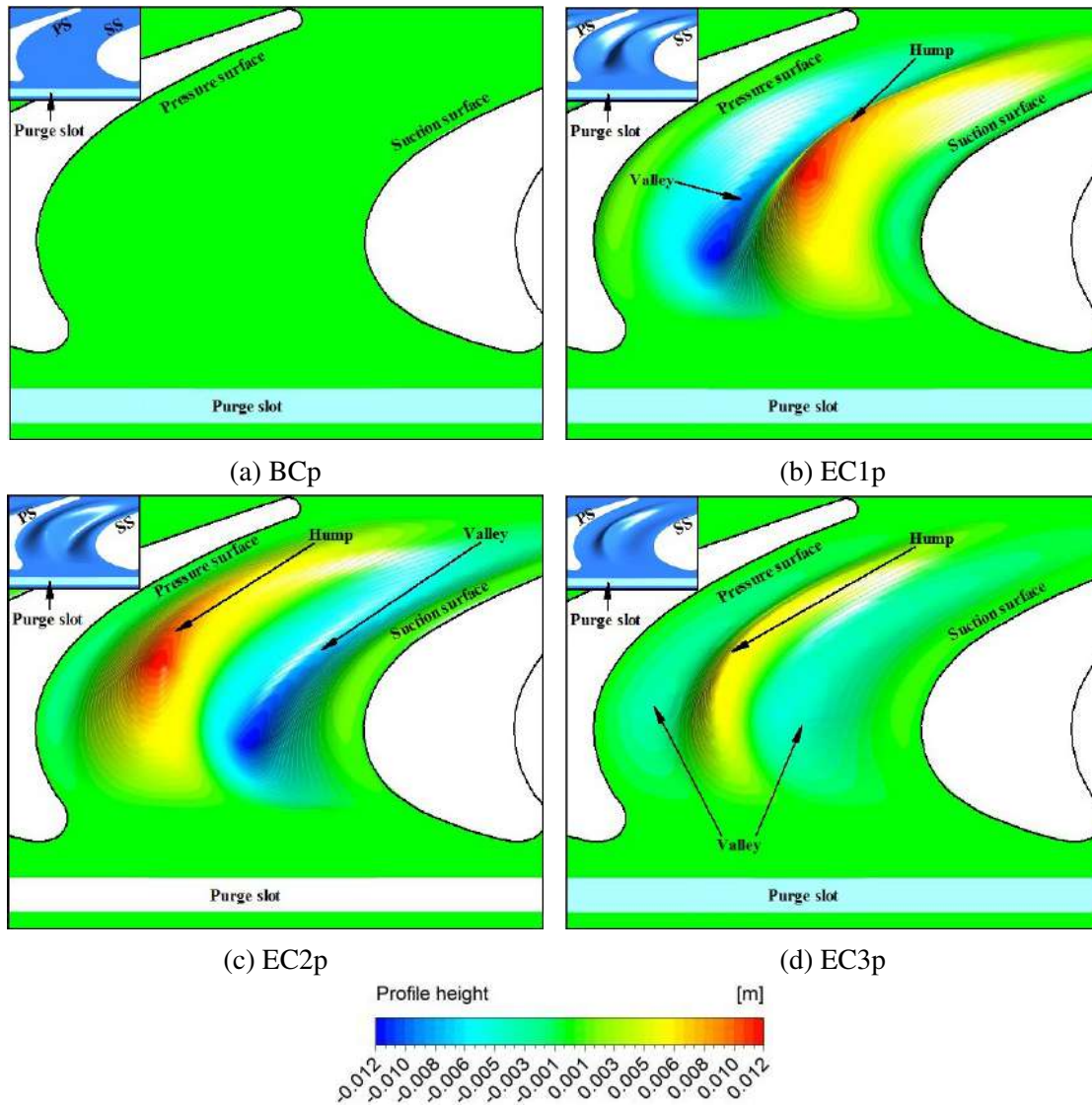
(b) EC1p

(c) EC2p

(d) EC3p

Figure 6.1: Contoured endwall height distribution of a) BCp b) EC1p C) EC2p d) EC3p configurations.

6.3 Effects of contoured endwall without purge flow

In the following sections, a preliminary investigation of contoured endwall has been conducted without purge flow. Aerodynamic behavior of the secondary vortices in rel-

ative to the position of profile hump and valley are explained in this section.

6.3.1 General flow behavior

Secondary vortex formations within the blade passage and at the exit of the blade passage are explained in Figure 6.2 using Q-criterion superimposed with streamwise vorticity. Major secondary vortices identified in the base case (BC) profile (Figure 6.2a) are pressure side leg of horseshoe vortex (PSL), suction side leg of horseshoe vortex (SSL), passage vortex (PV), pressure surface vortex (PSv) and pressure side corner vortex (PScv). Around the leading edge incoming mainstream boundary layer splits into two sections (PSL and SSL) and horseshoe vortex is formed (HSV). As the PSL enters the blade passage, it is influenced by the pitchwise pressure gradient and drifts towards the suction surface where it merges with the suction side leg and forms passage vortex. Two major reasons for the development of pressure surface vortex (PSv) are pressure side bubble (PSB) formation and spanwise pressure gradient. Aerodynamic blade loading near endwall will be less compared to midspan because of the presence of endwall secondary flows. Thus there exists a pressure gradient along the blade height between midspan region and endwall. Due to this pressure gradient low momentum fluid in the pressure side bubble, flow towards the endwall and generates pressure surface vortex (PSv). Along with the PSv, pressure surface corner vortex (PScv) can also be observed in Figure 6.2a and Figure 6.2b. In general, the corner vortices are energized when the surface streamlines meet the suction surface or leave the pressure surface more perpendicular. In Figure 6.2a more vortices can be observed at the blade trailing edge region. They are trailing edge shed vortex (TSV) and trailing edge-endwall corner vortex (TEcv). The vortex originating from the trailing edge just above the passage vortex is known as trailing edge shed vortex (TSV). They are formed as a result of the difference in the magnitude of spanwise velocity component on suction surface and pressure surface as well as change in circulation of mainstream fluid along the spanwise direction (Niewoehner *et al.* 2015; Cui and Tucker 2017). It has the rotational direction opposite to that of passage vortex. The merging of both corner vortices from pressure side and

suction side (PScv and SScv respectively) at trailing edge-endwall corner leads to the formation of TEcv. In contoured endwall configurations, the positions of hump and valley determines the magnitude and direction of additional vortices such as diverted pressure side leg vortex (PSLd) and the vortex induced by the PSLd at the hump tip called PSLi. In Figure 6.2b hump which is close to the suction surface fully diverts the pressure side leg vortex (PSL) and PSLd is generated which follows the curvature of the hump till the end of the blade passage. Moreover in Figure 6.2c and Figure 6.2d the position of hump near to pressure surface leads to the complete elimination of PSv formation. The depth of the valley in both cases determines the strength of passage vortex.

6.3.2   Distribution of streamwise vorticity

Streamwise vorticity distribution on six equidistant axial planes between leading edge and trailing edge (plane 1 to plane 6) and exit plane at 127% C_{ax} (plane 7) is shown in Figure 6.3. All the schematic plots explained in the Figure 6.3 are oriented in such a way that the view is from downstream direction. Reference figure (Figure A.2) is provided in the appendix for better understanding. As already explained in Figure 5.2, red color indicates vortices with positive rotational direction (clockwise) and blue color indicates vortices with negative rotational direction (anticlockwise). In all configurations both pressure side leg vortex (PSL) and passage vortex (PV) have negative sense of rotation and suction side leg vortex (SSL) has positive sense of rotation. Wall vortex (WV) which is induced by passage vortex, originates from the merging point of both legs of horseshoe vortex on suction surface (plane 4, 15% span), possess same rotational sense as that of SSL. The concept of wall vortex was first introduced by Wang *et al.* (1995).

Trailing edge filament vortex (TFV) observed in plane 7 is generated due to the merging of vortex filaments from both pressure and suction surfaces which possess different acceleration (Niewoehner *et al.* (2015)). In Figure 6.3b, the hump of EC1 configuration has restricted the PSL from reaching suction surfaceand as a consequence,

98
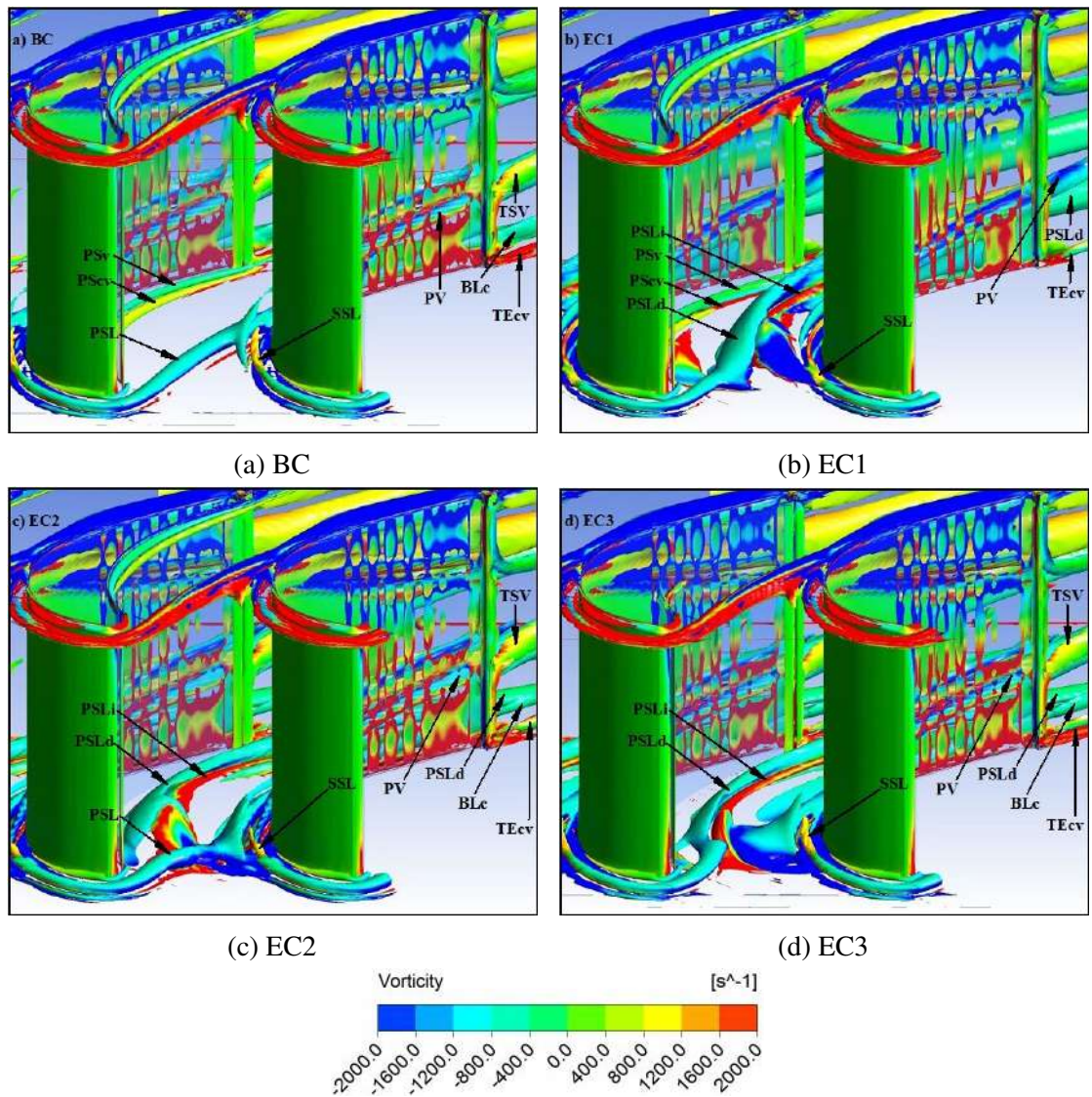
Figure 6.2: Blade passage vortex formations using Q-criterion for a) BC b) EC1 C) EC2 d) EC3 configurations.

PSLd is generated (plane 3). The slope of the contoured endwall from valley to the hump (plane 4) intensifies the vorticity strength of PSLd. The intensified PSLd induces another additional vortex named PSLi which is periodic in nature and can be observed from plane 4 onwards along the curvature of the profile hump. At the blade exit PSLi merges with the suction side corner vortex (SScv) to form trailing edge-endwall corner vortex (TEcv). The position of the pressure surface vortex (PSv) and pressure surface

corner vortex (PScv) remains unaltered till plane 4 and in plane 5 both vortices starts drifting toward the valley as a result of variation in the static pressure distribution over the contoured endwall. In EC2 configuration, the intensification of passage vortex at the valley close to the suction surface is detected from plane 3 onwards. Although the hump near to pressure surface obstructs diverted pressure side leg vortex (PSLd) from traversing towards suction surface, the increased depth and steepness of the valley towards suction surface instigates passage vortex to enlarge, keeping the vortex intensity high at the passage exit. Along with the passage vortex loss core, a 5% spanwise shift, away from the hub endwall can be noticed for WV, TSV and TEcv in exit plane 7. For the EC3 configuration, the passage vortex has the lowest vortex intensity of the three contoured endwall designs investigated. Diverted pressure side leg vortex (PSLd) generated along the contour hump does not merge with the passage vortex at the blade exit in EC3 configuration. Separate trace of PSLd with low vortex intensity can be observed in plane 7. The negative vorticity of passage vortex (PV) and positive vorticity of exit secondary vortices (TSV & TFV) are slightly decreased due to the separation of PSLd but spanwise position remains unaltered. In EC3 configuration, pressure surface vortex (PSv) and pressure surface corner vortex (PScv) are eliminated due to the considerable reduction in the pressure gradient on the endwall surface in pitchwise direction.

6.3.3 Endwall static pressure and surface streamlines

Figure 6.4 represents the static pressure coefficient distribution together with endwall surface streamlines for base case and endwall contoured configurations. The static pressure coefficient (C_{ps}) is defined as the ratio of local static pressure (P_s) to inlet mass averaged dynamic pressure. The obvious high pressure zone near pressure surface and low pressure zone near suction surface can be observed in all figures. This pitchwise pressure gradient serves as the source of endwall boundary layer cross flow. Acceleration of the mainstream flow along the blade passage leads to gradual reduction of C_{ps} distribution from leading edge to trailing edge. In Figure 6.4a, as explained earlier, at midpassage region (45% C_{ax}), close to suction surface, both legs of horseshoe vortex
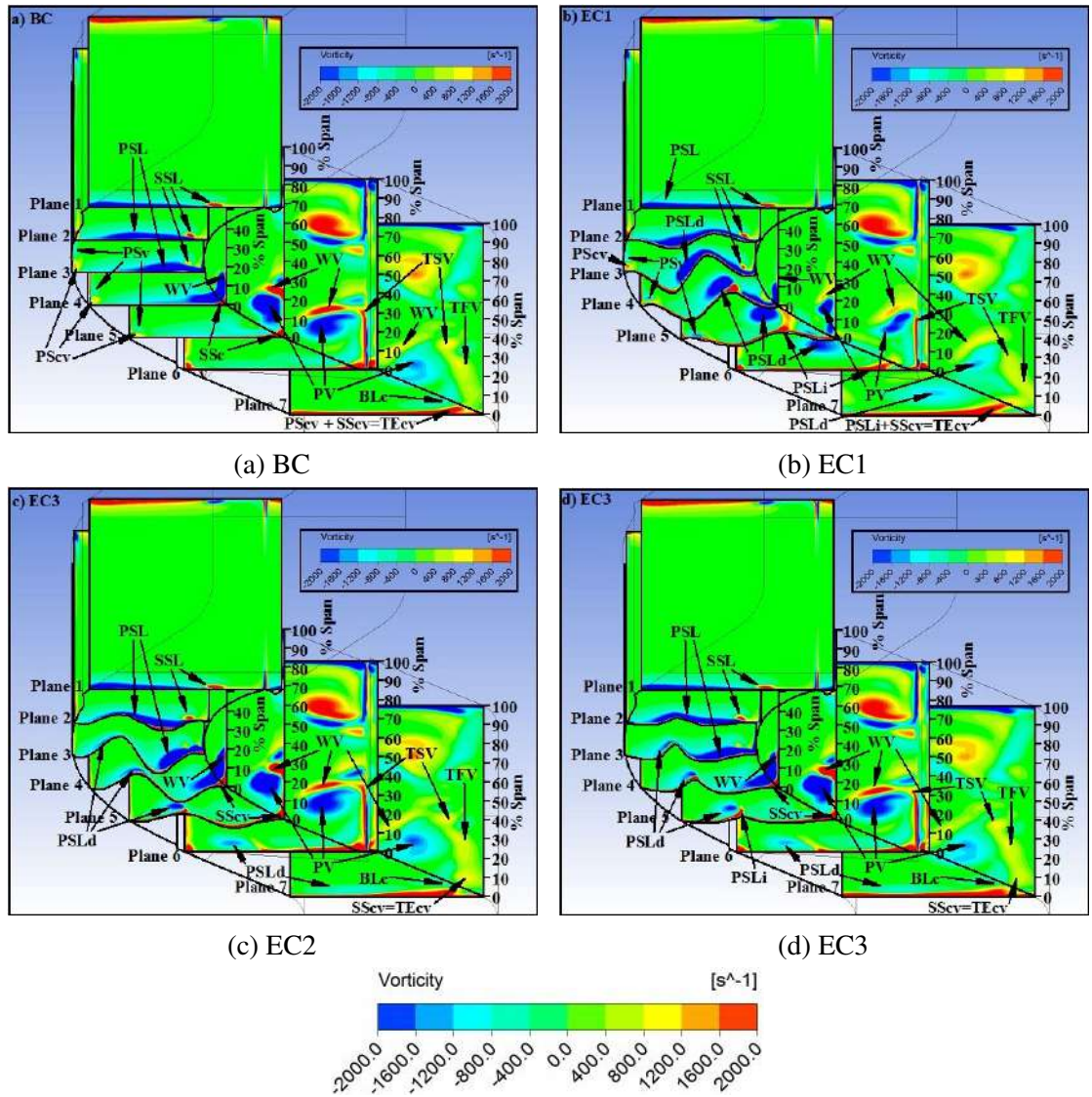
Figure 6.3: Streamwise vorticity at different axial planes for a) BC b) EC1 C) EC2 d) EC3 configurations.

merge together and strong passage vortex is formed. The presence of uneven hump and valley in the contoured endwall configurations has increased the non-uniformity in the endwall C_{ps} distribution especially for EC1 and EC2 configurations. At the maximum depth of the valley in both cases, C_{ps} distribution has increased and a stagnation zone (black dashed circle) has been generated. In EC1 configuration, even though the profile hump has diverted the PSLd from reaching the suction surface, its convex region has

resulted in the greater acceleration of the same at the aft portion of the passage. This is clear from the low pressure contour over the profile profile hump from 50% Cax onwards. At the upstream region of blade passage, both PSL and PSLd have experienced a slight bend (direction shown by dark arrow) due to the presence of stagnation zone within the valley. In EC2 configuration, the valley which is positioned away from the pressure surface generates less intense stagnation zone compared to EC1 configuration. However hump and valley have modified the endwall secondary flow more vigorously. The stagnation zone (black dashed circle) has pushed the pressure side leg vortex (PSL) far upstream which resulted in the entrainment of more incoming boundary layer fluid. The pressure side leg vortex (PSL) has accelerated more before it merges with the suction side leg vortex (SSL) nearly at 30% of C_{ax}. This is evident from the low C_{ps} contour near to suction surface along the trajectory of PSL from 25% C_{ax} onwards. Majority of the endwall cross flow (red dashed line) which surpassed the hump merges with the PV at the aft portion of the blade passage (90% of C_{ax}). The pressure gradient evolved in between stagnation zone and suction surface (SS) has magnified the midpassage cross flow which in turn resulted in the strengthening of passage vortex at the blade exit. On the contrary, in EC3 configuration, the reduction of valley depth has resulted in the complete elimination of above observed stagnation zone. Also the hump has restricted the turning of endwall boundary layer more towards the suction surface due to the reduction of pitchwise pressure gradient throughout the blade passage. The formation of diverted pressure side leg vortex (PSLd) and the effective deceleration of pressure side leg vortex (PSL) have reduced the strength of passage vortex. In EC2 and EC3 configurations, the surface streamlines seems more attached to the pressure surface which denote the elimination of pressure surface vortex (PSv) as well as pressure surface corner vortex (PScv).

6.3.4 Vectorial representation of PSB

The effects of endwall contouring on pressure side bubble (PSB) formation are explained in the Figure 6.5. Dark blue color region close to the pressure surface indicates
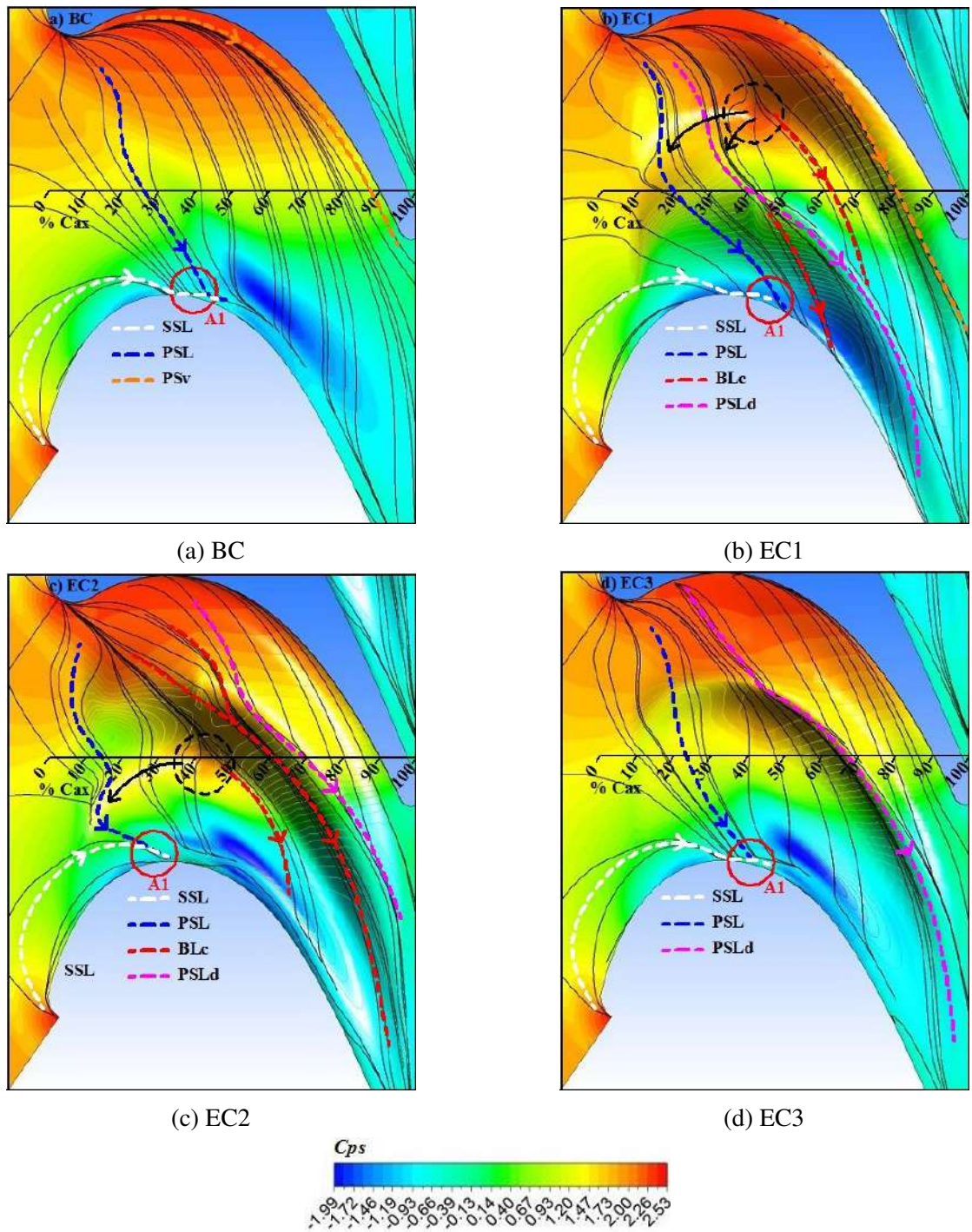
(a) BC   (b) EC1

(c) EC2   (d) EC3

Figure 6.4: Endwall static pressure coefficient (C_{ps}) distribution superimposed with endwall surface streamlines for a) BC b) EC1 C) EC2 d) EC3 configurations.

the negative values of non-dimensionalised axial component of resultant velocity vector which represents the flow reversal. Furthermore the vectorial representation of resultant velocity also provides additional insight to the physical mechanism responsible for the formation of PSB. The location of separation point (S) and reattachment point (R) happening at local maximum static pressure is mentioned in all figures. At design condition, for base case (BC) and EC1 configuration, PSB formation begins from 13% C_{ax}. For EC1 configuration, tail end of the PSB is shifted upstream from 36% to 33% C_{ax} compared to BC configuration, due to the increase in the static pressure ensued from the peak hump located near to suction surface. The shifting of profile hump near to pressure surface (EC2) has reflected in the drastic reduction of PSB size. The shifting of separation point and reattachment point to 15% C_{ax} and 20% C_{ax} has confined the PSB to a small region. As explained in the Figure 6.4c the endwall boundary layer fluid which surpass the upstream portion of profile hump leads to the existence of PSB. However the reconstruction of PSB to PSv at endwall is fully eliminated. However, in Figure 6.5d no more PSB is visible along the pressure surface which means the endwall profile adopted in EC3 configuration has succeeded in eliminating both PSB and PSv formation on the pressure surface by reducing the pitchwise endwall pressure gradient. It is also evident from the Figure 6.4d that the endwall streamlines striking the profile hump does not ride over the hump as observed in EC2 configuration rather it flow downstream along the hump curvature till the passage exit.

6.3.5   Effect on exit yaw angle

Exit yaw angle (β) deviation is an important parameter which can influence the turbine stage aerodynamic performance because outflow angle directly influences the inlet conditions of succeeding blade rows. Figure 6.6 shows the contour plot of exit yaw angle deviation at 127% C_{ax}. As explained in Figure 5.4 the yaw angle has been calculated by following the procedure suggested by Qi *et al.* (2012). Endwall secondary flow vortices lead to overturning (positive yaw angle) towards endwall and underturning (negative yaw angle) towards midspan. Major endwall secondary vortices which contribute to
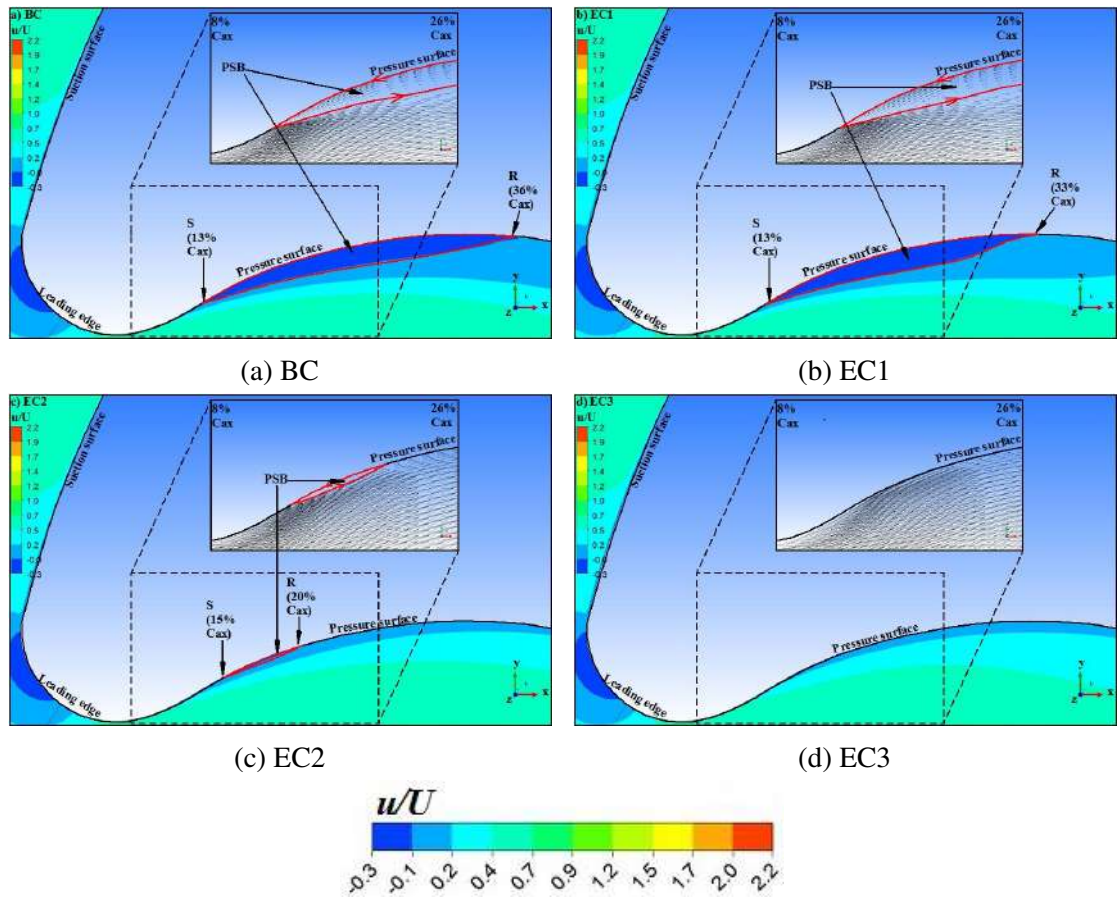
Figure 6.5: Predicted contours of *u/U* around the blade leading edge at 13% span (inset picture shows the velocity vectors near the pressure surface) for a) BC b) EC1 C) EC2 d) EC3 configurations.

exit yaw angle deviation are marked with their rotational direction while viewing in the downstream direction (from inlet to exit). Passage vortex (PV) and trailing shed vortex (TSV) with underturning can be identified towards midspan. Diverted pressure side leg vortex (PSLd), boundary layer cross flow (BLc) and trailing edge corner vortex (TEcv) are observed at near endwall region. Compared to base case the depth of overturning towards the endwall region is increased due to the existence of PSLd in all contoured endwall configurations. This phenomenon is more pronounced in EC1 configuration and the peak value has a significant radial extension towards the span of 7%. However in Figure 6.6b, overturning towards the midspan is reduced due to the presence of weakened passage vortex. In other two contoured endwall configurations (EC2 and EC3) the

overturning peak value towards the endwall is limited to the endwall surface. Comparing both configurations, slightly reduced underturning and overturning of passage vortex can be noticed between the span of 20% and 40%. At the same time, slightly diminished region of overturning near the endwall in EC3 configuration is noticed due to the presence of weakened PSLd. However, comparing all three contoured endwall configurations, EC3 configuration can demand substantial reduction in exit yaw angle deviation and follows the same trend as that of base case, except at endwall.

6.3.6 Spanwise variation of flow quantities

Effect on pitch averaged total pressure loss coefficient

Figure 6.7 shows the predicted pitch averaged total pressure loss coefficient ($\overline{C_{po}}$) at 127% C_{ax}. Near to endwall, maximum loss reduction can be observed for the base case compared to contoured endwall configurations. In EC1 configuration, even though the profile hump guides the diverted pressure side leg vortex (PSLd) more axially, the presence of stagnation zone within the preceding valley strengthened the same with negative vorticity which results in the formation of abrupt $\overline{C_{po}}$ peak value of 0.3 at 13% span. Along with the PSLd, another additional vortex (PSLi) having positive sense of rotation, generated by the profile hump, also caused additional losses at endwall for EC1 configuration. In EC2 and EC3 configuration, upto an average span of 15%, the slope of the $\overline{C_{po}}$ curve increased gradually because of the presence of comparatively weaker PSLd and PSLi. However EC2 configuration exhibits higher losses compared to EC3 case. In EC2 configuration, the higher depth of valley has agitated the passage vortex to climb the suction surface more and the strong suction side corner vortex (SScv) leaving the blade trailing edge causes additional secondary losses at trailing edge-endwall corner region. Further insight into the performance of contoured endwall on secondary loss reduction at blade exit can be sought by analyzing the variation of the peak values of passage vortex (PV) loss core regions and counter vortex loss core regions. For base case, the peak loss core of passage vortex and counter vortex occurs at 26% and 37% of
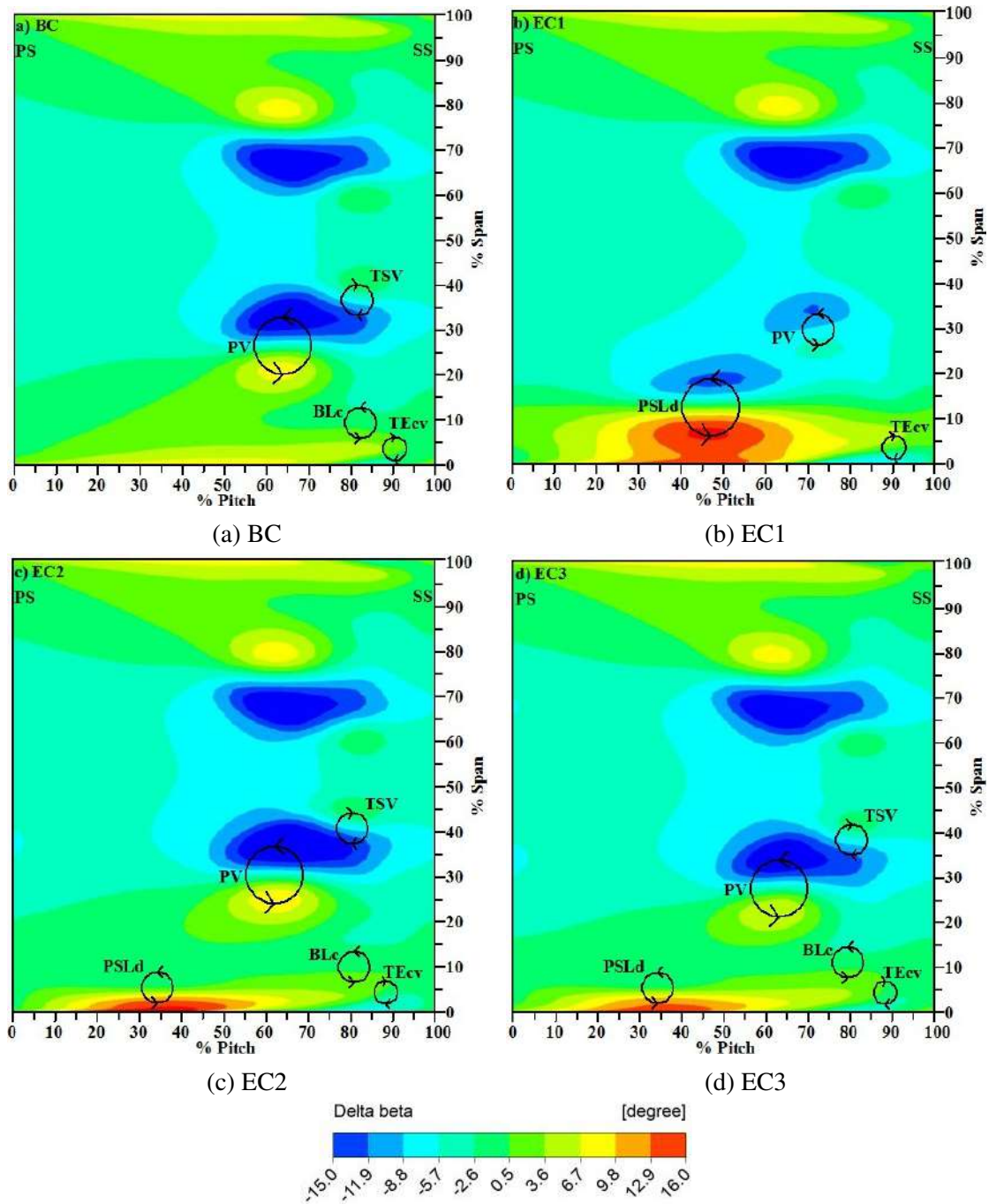
Figure 6.6: Comparison of exit yaw angle deviation at 127% C_{ax} for a) BC, b) EC1, c) EC2, d) EC3 configurations.

span respectively. In general, contouring of hub endwall exhibits reduction in the loss coefficient over a span of 20%$< H <$37% by restricting the peak loss core of passage

vortex well below the base case except for EC2 configuration. The formation of diverted pressure side leg vortex (PSLd) results in the breakdown of passage vortex loss core and as a result, above 16.7% of span, EC1 configuration shows the maximum reduction in the loss coefficient. In this configuration, the peak loss coefficient generated by passage vortex is smaller than that generated by counter vortrices (CV). EC2 configuration has enhanced the passage vortex loss core and counter vortex loss core by shifting the peak values both tangentially and radially. Among the tested cases EC3 configuration has exhibited considerable reduction in the loss core intensities of both passage vortex and counter vortices. Comparing all contoured endwall cases, EC3 configuration follows similar trend as same as base case over the full span except at near endwall regions.
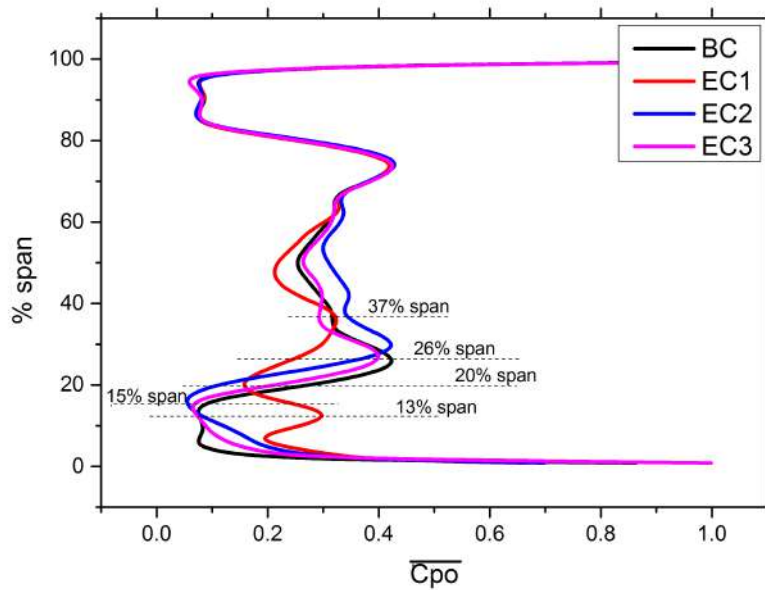
Figure 6.7: Spanwise variation of pitch averaged total pressure loss coefficient ($\overline{C_{po}}$) distribution at 127% C_{ax}.

Effect on pitch averaged CSKE

Figure 6.8 explains pitch averaged CSKE (coefficient of secondary kinetic energy) plotted along the blade span at 127% C_{ax}. The definition of CSKE has been adopted from previous literatures Chen *et al.* (2019, 2020). CSKE is a parameter used to measure

the strength of secondary losses. It measures the quantity of kinetic energy processed by the vortices generated due to viscous effect and potential flow. For convenience the correlation used for calculating CSKE is given below (Eq. 6.1 & 6.2).

$$CSKE = \frac{V_{sec}^2 + w^2}{U^2} \tag{6.1}$$

$$V_{sec} = -u\sin\beta + v\cos\beta \tag{6.2}$$
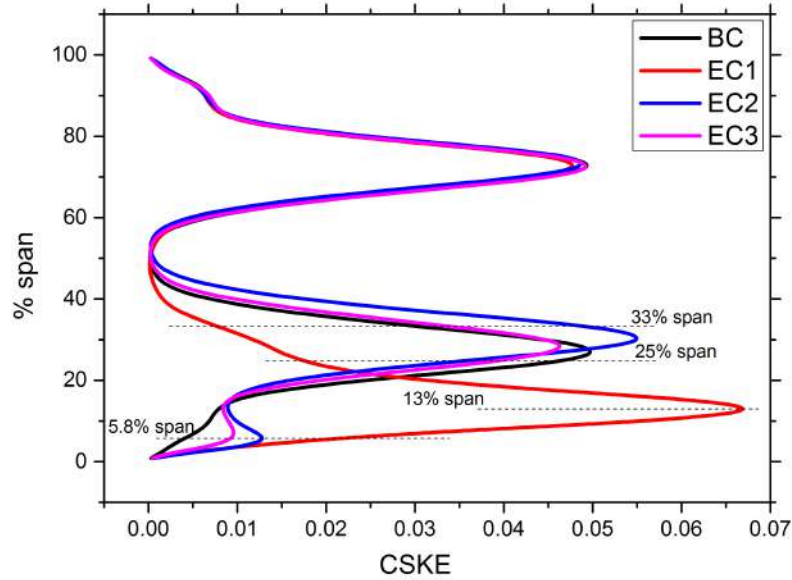
Figure 6.8: Pitch averaged spanwise distribution of CSKE at 127% C_{ax}.

Thus CSKE represents the robustness of endwall cross flow which is responsible for the rolling up of endwall boundary layer to form passage vortex (PV) and related secondary vortices. Analyzing the Figure 6.8, the endwall contouring has magnificent effects on the CSKE distribution below midspan. Near to endwall, at 13% span, EC1 configuration is showing a CSKE peak of 0.067 which constitute the diverted pressure side leg vortex (PSLd) having intense vortex strength gained while accelerating from the upstream valley depth towards the downstream peak hump. For EC2 and EC3 con-

figurations the CSKE peak has too less values compared to EC1 configuration which represents the existence of PSLd at 5.8% span. Towards the midspan, passage vortex strength can be attributed by analyzing the variation in the peak value of CSKE especially between 25% and 33% span. For EC1 configuration, the peak is nowhere visible since the endwall profile has weakened the PV to a large extend. Compared to base case (BC), CSKE peak which represents the PV in EC2 configuration has increased and shifted upwards. The reason for this is the earlier formation of passage vortex and enhanced boundary layer cross flow (BLc) occurring within the contour valley (Figure 6.4c). On the contrary, in EC3 configuration, the same peak which represents passage vortex has reduced but the spanwise location remains unaltered. From the pitch averaged total pressure loss coefficient distribution, EC1 configuration has exhibited maximum loss reduction throughout the span (Figure 6.7). However the secondary kinetic energy related to the diverted pressure side leg vortex in EC1 configuration close to the endwall region is too high compared to EC3 configuration (Figure 6.8, 13% span). Considering both parameters, as primary objective functions for maximum loss reduction, EC3 configuration is considered as a better design.

6.4   Effects of contoured endwall with purge flow

The purge flow leads to the earlier formation of passage vortex. In the following sections, aerodynamic performance and secondary flow modifications associated with three different contoured endwall configurations in the presence of purge flow are analyzed and compared with base case with flat endwall configuration (BCp). For better understanding, suffix p is added to all configurations which includes purge flow.

6.4.1   General flow behavior

Figure 6.9 presents the secondary vortex formation within the blade passage and at the exit of the blade passage using Q-criterion superimposed with streamwise vorticity. In Figure 6.9, purge vortex (Vp), generated by the introduction of purge flow can be ob-

served in all configurations, in addition to the secondary vortices explained in Figure 6.2. In all contoured endwall configurations, as explained in section 6.3.1, direction of the pressure side leg of the horseshoe vortex (PSL) gets diverted and subsequently referred as the diverted pressure side leg vortex (PSLd). The vortex induced by the passage vortex over the hump tip in EC1p configuration is mentioned as PVi. In EC1p configuration (Figure 6.9b) the valley region causes earlier detachment of pressure surface vortices (PSv) from pressure surface and it merges with the diverted pressure side leg vortex (PSLd) at the aft portion of the blade passage. However, diverted pressure side leg vortex (PSLd) merges with the passage vortex at the exit region and as a result, exit secondary loss enhances for the EC1p configuration. In EC2p configuration (Figure 6.9c) detachment of PSv from pressure surface is delayed as the hump is positioned near the pressure surface. Meanwhile the EC3p profile has effectively restricted the pressure side leg vortex (PSL) from reaching suction surface. The diverted pressure side leg vortex (PSLd) follows the hump till the end of the blade passage. Moreover, the formation of pressure surface vortex (PSv) as well as pressure side bubble (PSB) have been completely eliminated by the EC3p configuration.

6.4.2 Distribution of streamwise vorticity

Figure 6.10 shows the axial distribution of streamwise vorticity for contoured endwall configurations in the presence of purge flow. The axial planes within the blade passage (plane 1 to 6) are separated by 20% C_{ax} and the plane 7 at the cascade exit is located at 127% C_{ax}. To avoid complexity, reference figure (Figure A.2) is provided in the appendix. The characteristic features of endwall secondary flow field in the presence of an upstream purge flow are evident in Figure 6.10. Development of passage vortex (PV), the dominant secondary flow structure having negative vorticity, traversing from pressure side to suction side can be observed in all configurations. Interaction of low momentum purge flow with the mainstream endwall boundary layer enhances the cross flow which leads to the earlier formation of passage vortex (PV) (Figure 6.10a). Another clear evidence of enhanced cross passage boundary layer flow in the presence
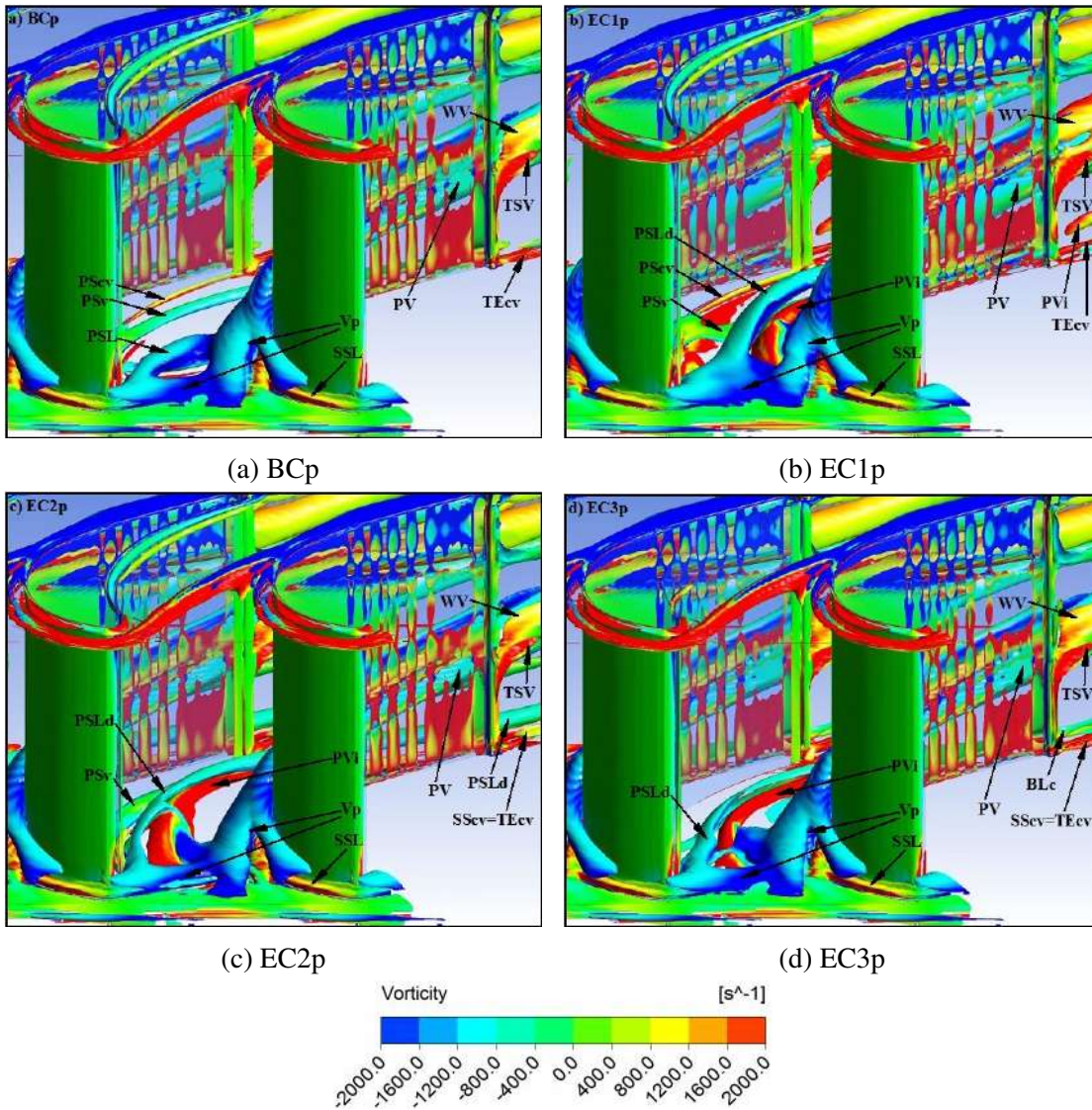
Figure 6.9: Blade passage vortex formations using Q-criterion for a) BCp b) EC1p C) EC2p d) EC3p configurations.

of purge flow is observed in plane 2 to 5 near pressure surface-endwall corner (Figure 6.10a) where pressure surface vortex (PSv) evolved from the pressure side bubble (PSB) slides down from the pressure surface and drift towards the mid passage while progressing downstream over the endwall. In EC1p configuration (Figure 6.10b), although diverted pressure side leg vortex (PSLd) seems separated from passage vortex (PV) (as observed in plane 3), the vortices merge at the passage exit (plane 6). A dif-

fusive effect developed within the valley region between hump and suction surface, instigate the passage vortex (plane 3, 4, 5) to induce a new vortex called PVi (vortex induced by passage vortex) (Figure 6.10b). As PVi climbs up the suction surface, the suction side corner vortex (SScv) is strengthened with the sense of rotation opposite to PVi (Figure 6.10b, plane 6). The merging of both vortices with trailing edge-endwall corner vortex (TEcv) intensified the latter with a spanwise shift of 12% away from end-wall (black circle, plane 7). At the passage exit (plane 6 & 40% span), presence of PVi having positive rotational sense abet both wall vortex (WV) and trailing edge shed vor-tex (TSV) to strengthen against the passage vortex (PV) on the profile boundary layer. The EC2p configuration leads to additional loss generation at downstream region due to the increased static pressure in the valley region. This instigates the passage vortex (PV) to climb the suction surface a bit early (Figure 6.10c, plane 3). Hence rather than decreasing the exit disturbances, the agitated passage vortex causes additional losses. In contrast to the EC2p configuration, the reduced valley depth in the EC3p configuration reduces the strength of passage vortex while climbing the suction surface. This atten-uates the shear between the passage vortex and profile boundary layer and therefore restricts the loss production. The reduced hump height is much effective in guiding the diverted pressure side leg vortex (PSLd) towards the passage exit without any dominant rotational effects. It has succeeded in evenly distributing the endwall static pressure mostly at pressure surface-endwall corner region and thereby successfully eliminating pressure side bubble (PSB) and pressure surface vortex (PSv) formation (detailed ex-planation given in Section 6.4.7). It is to be noted that, the spanwise extend of loss core regions in axial planes remain unchanged with all the configurations. The variation in the loss generation solely depends on the vortex intensity possessed by each secondary vortex.

6.4.3   Endwall static pressure measurement and surface streamlines

Contour of static pressure coefficient (C_{ps}) and surface streamlines over the hub endwall are shown in Figure 6.11. C_{ps} is obtained by non-dimensionalizing static pressure (P_s)
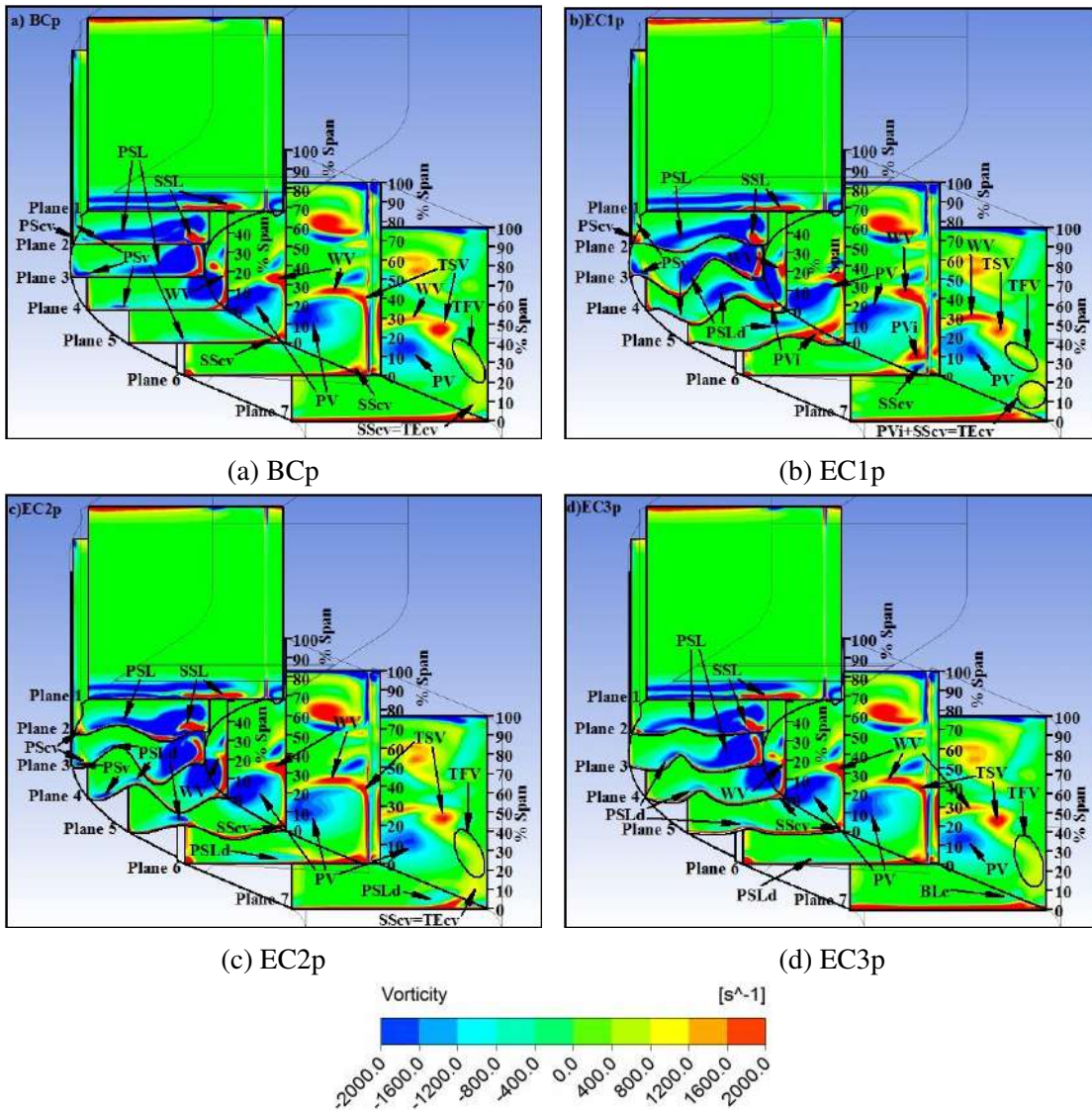
Figure 6.10: Streamwise vorticity at different axial planes for a) BCp b) EC1p C) EC2p d) EC3p configurations.

with inlet dynamic pressure (Eq. 6.3).

$$C_{ps} = \frac{P_s}{0.5\rho_\infty U^2} \tag{6.3}$$

For BCp configuration (Figure 6.11a) the purge vortex (Vp), suction side leg vortex (SSL) and pressure side leg vortex (PSL) merge together between 30% and 40% C_{ax}

and a strong passage vortex is formed. In contoured endwall configurations (Figures 6.11b, 6.11c, 6.11d), variation of endwall flow topology developed from the change of position of hump and valley can be clearly visible from the pattern of surface streamlines. In EC1p configuration (Figure 6.11b), the stagnation zone generated at the valley, near the pressure surface (40% C_{ax}) and the low pressure region visible at the aft portion of the passage above the hump (65% C_{ax}) magnifies the magnitude of endwall pressure gradient and results in strong endwall boundary layer cross flow (BLc). At the beginning of the blade passage, bending and turning of purge vortex (Vp) and pressure side leg vortex (PSL) around the convex surface of upstream hump leads to the earlier merging of both vortices approximately at 20% C_{ax}. Though the hump has separated PSLd from PSL, the former had merged with the passage vortex (PV) nearly at 65% C_{ax} as a result of strong boundary layer cross flow (BLc). This is evident from the low pressure zone developed over the hump at 65% C_{ax}. Also growth of vortex induced by passage vortex (PVi)) can be observed, as the endwall streamlines spreads over the distance between suction surface and profile hump. In this region (40% C_{ax} to 80% C_{ax}) the surface streamlines are directed away from the suction surface rather than accumulating towards suction side - endwall corner. In EC2p configuration (Figure 6.11c), the stagnation zone generated at the valley near the suction surface (40% C_{ax}) is not so strong compared to EC1p configuration. However, it is capable of pushing the pressure side leg vortex (PSL) upstream and it leads to the earlier formation of passage vortex (PV). Even though the hump has directed the diverted pressure side leg vortex (PSLd) more axially, majority of the endwall boundary layer fluid from the pressure side (dashed red line) crosses the hump and joins with the passage vortex (PV) at the aft portion of the blade passage at around 85% C_{ax}. However, EC3p configuration (Figure 6.11d) is capable of providing endwall C_{ps} distribution almost similar to base case with purge (BCp) configuration. The orientation of the surface streamlines shows the effective reduction of boundary layer cross flow (BLc) at both fore and aft part of the blade passage. The presence of hump has effectively reduced the endwall static pressure gradient and completely eliminated the pressure surface vortex (PSv) formation. The

formation of diverted pressure side leg vortex (PSLd) has reduced the strength of passage vortex (PV). The reduction in the depth of the valley has mitigated the progressive growth of passage vortex, compared to other two contoured endwall configurations.

6.4.4 Vectorial representation of PSB

The existence of a pressure side bubble (PSB) and its geometrical variations are explained using axial velocity contours in Figure 6.12. Comparison of different contoured endwall configurations reveals that contoured endwall configurations significantly modifies the pressure side bubble (PSB) formation over pressure surface. To get a better understanding, vector plot of the pressure side bubble (PSB) (location between 8% and 26% C_{ax}) is shown in the inset of each figures. Negative value of non-dimensional axial component of velocity indicates the region of reverse flow. The point of separation (S) and reattachment (R) are marked at appropriate locations. Spanwise and streamwise pressure gradient on the pressure surface characterizes transport and growth of PSB and its conversion to pressure surface vortices. In all configurations, the point of separation of PSB is located at 13% C_{ax}. The first two contoured endwall configurations (EC1p and EC2p) have succeeded in keeping the size of pressure side bubble smaller compared to the BCp configuration and also the reattachment (R) point is shifted upstream to 31% C_{ax}. The additional stagnation zone generated in the valleys of both configurations has accelerated the pitchwise endwall cross flow much higher compared to BCp configuration. The observations suggest that in the presence of purge flow, pressure side bubble (PSB) has the tendency to roll up into pressure side leg vortex (PSL) at the endwall. However small reduction in size of pressure side bubble (PSB) is achieved due to the presence of hump which tried to restrict the pressure side leg vortex (PSL) from traversing in pitchwise direction. On the contrary, the EC3p configuration has succeeded in minimizing the endwall boundary layer cross-flow effectively thereby eliminating the formation of pressure side bubble (PSB) as well as pressure surface vortex (PSv). In EC3p configuration, the improved static pressure distribution on the pressure surface near to endwall region has reduced the spanwise pressure gradient.
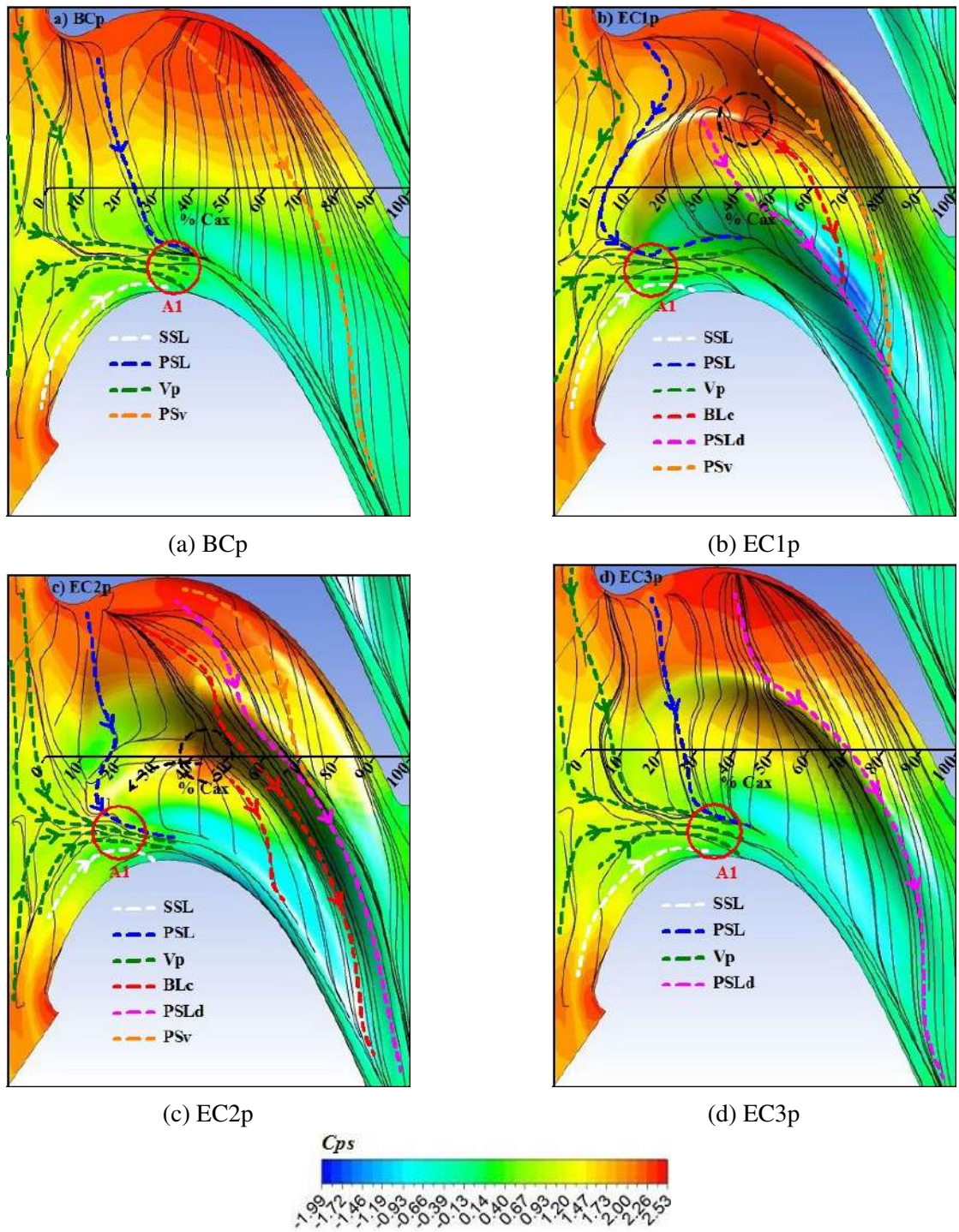
Figure 6.11: Endwall static pressure coefficient (C_{ps}) distribution superimposed with endwall surface streamlines for a) BCp b) EC1p C) EC2p d) EC3p configurations.
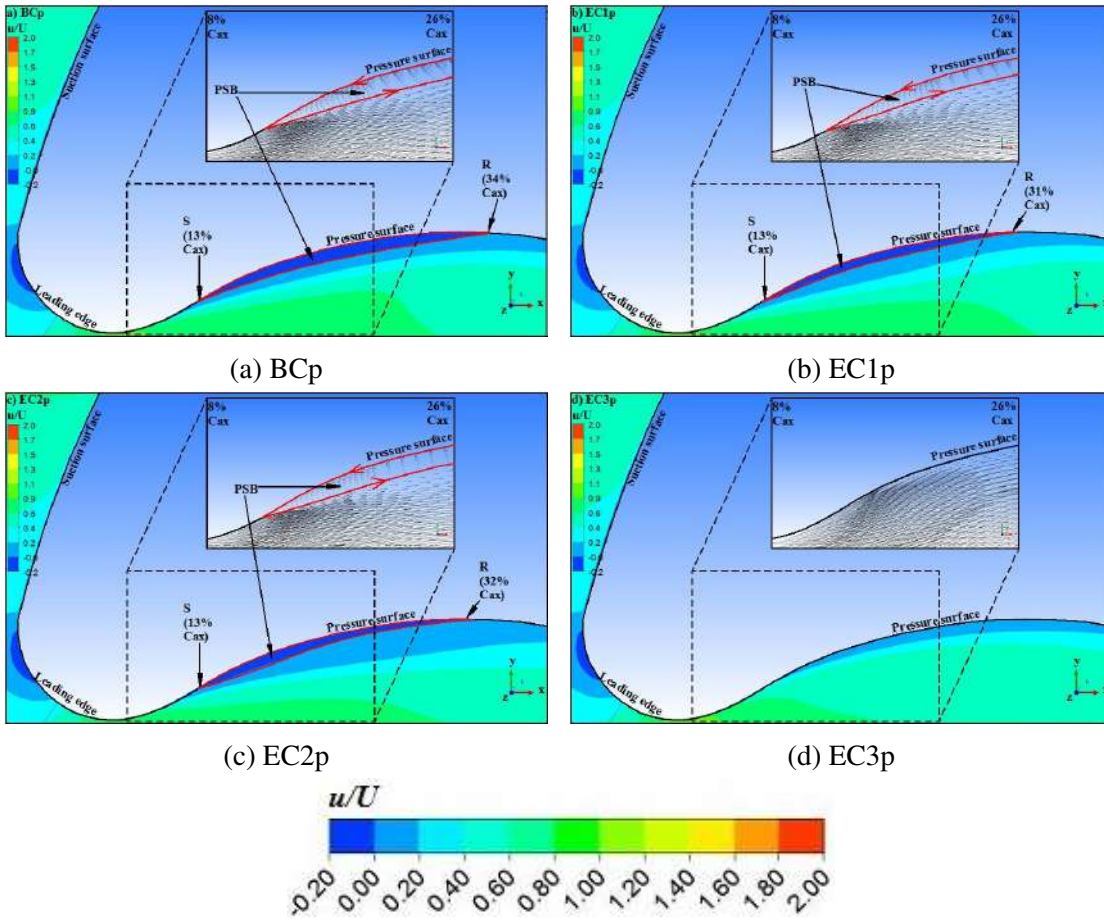
Figure 6.12: Predicted contours of *u/U* around the blade leading edge at 13% span (inset picture shows the velocity vectors near the pressure surface) for a) BCp b) EC1p C) EC2p d) EC3p configurations.

6.4.5 Effect on exit yaw angle

The effect of purge flow on exit yaw angle (β) is investigated at 127% C_{ax} (Figure 6.13). Values larger than zero degree are termed as overturning and values smaller are termed as underturning. In general, towards midspan region, flow is underturned because purge flow enhances the passage vortex and the loss region extends both spanwise and pitch-wise directions. Moreover secondary vortices such as wall vortex (WV) and trailing edge shed vortex (TSV) also contributes the underturning at the midspan region. In EC1p configuration (Figure 6.13b) the delayed separation of wall vortex (WV) from

118

suction surface due to the presence of PVi (vortex induced by passage vortex), keeps wall vortex more close to the trailing edge shed vortex (TSV). However the effects of both these vortices on exit angular deviation remains more or less same for all the tested configurations. Towards the endwall, overturning caused by the passage vortex (PV) starts decreasing upto an average span of 10% and again increases near the endwall surface for all configurations. In contoured endwall configurations, overturning near the endwall surface is administered by the position and vortex intensity of diverted pressure side leg vortex (PSLd). In EC1p configuration, PSLd is not visible, since at the aft portion of the blade passage, it merges with the passage vortex. Instead, strong formation of PVi (vortex induced by passage vortex) and its merging with the suction side corner vortex (SScv) increases the extend of overturning in pitchwise direction. In EC2p configuration (Figure 6.13c) the diverted pressure side leg vortex (PSLd) which remains separated from passage vortex (PV), climbs to a span of 6% from endwall and exhibits slightly higher overturning at the endwall (45% to 75% pitch). Trailing edge - endwall corner vortex (TEcv) having opposite sense of rotation as that of PSLd, is equally energized and exhibits a region of underturning near the suction surface - endwall corner. However this advancement in underturning is too low to compromise for the overturning generated by PSLd. The pitchwise and spanwise extend of overturning and underturning at the endwall observed in EC2p configuration got diminished in EC3p configuration (Figure 6.13d). In other words, EC3p configuration seems effectively working on mitigating the pitchwise endwall pressure gradient thereby reducing the strength of passage vortex (PV) towards midspan and boundary layer cross flow (BLc) near endwall. The effect of reduced hump height and valley depth curtails the vortex strength of PSLd and climbing of passage vortex (PV) over suction surface respectively.

(a) BCp   (b) EC1p
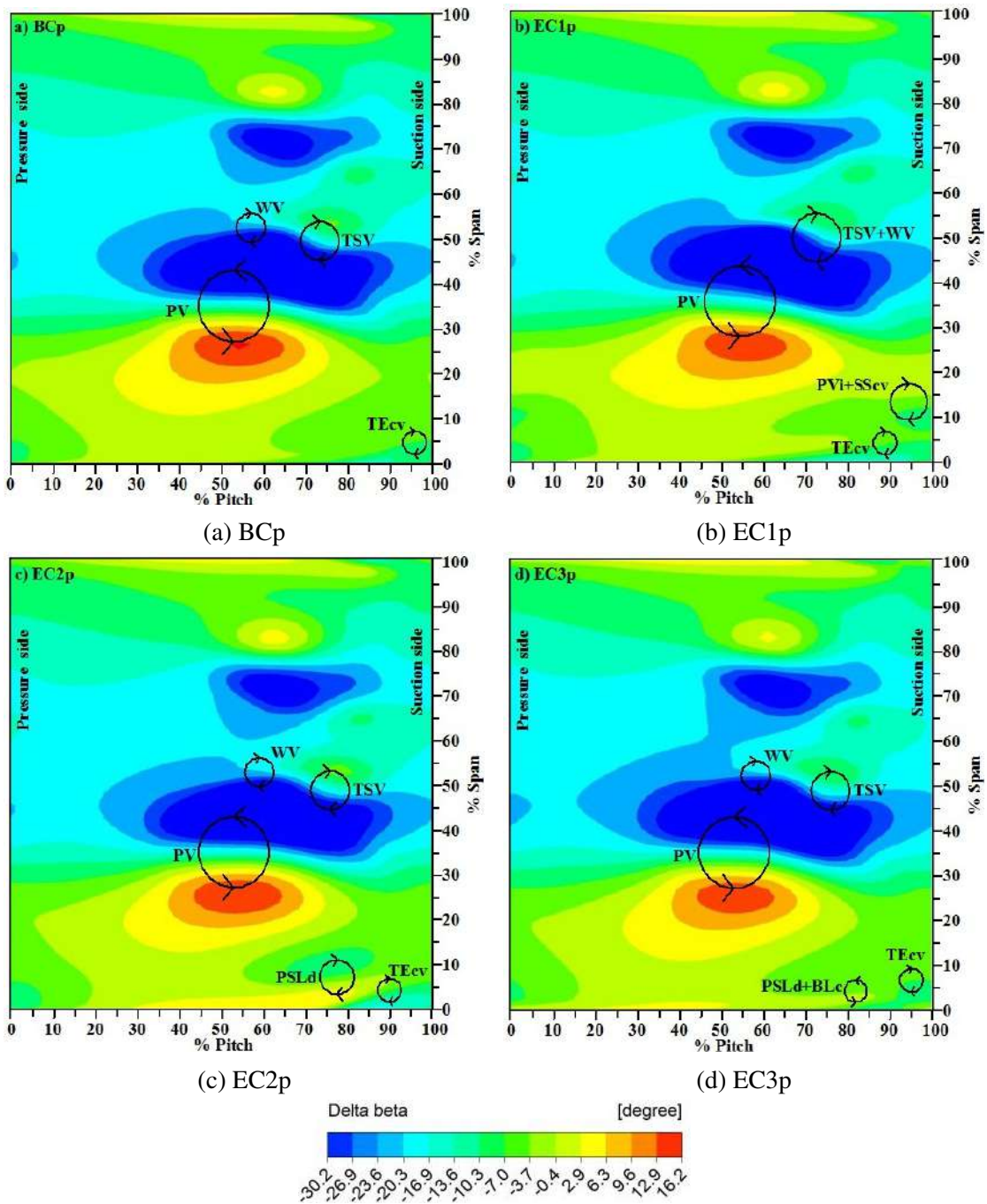
(c) EC2p   (d) EC3p

Figure 6.13: Comparison of exit yaw angle deviation at 127% C_{ax} for a) BCp b) EC1p c) EC2p d) EC3p configurations.

6.4.6 Spanwise variation of flow quantities

Effect on pitch averaged total pressure loss coefficient

In addition to the endwall static pressure coefficient (C_{ps}) and exit yaw angle (β), pitch averaged total pressure loss coefficient (C_{po}) at 127% C_{ax} is analyzed and shown in Figure 6.14. At the midspan region, two major peaks are generated by passage vortex (black dashed ellipse) and counter vortices (black dashed circle). Both passage vortex (PV) and counter vortices (WV&TSV) enlarges in pitchwise direction but the position remains same in spanwise direction. For EC1p configuration the effect of endwall contouring becomes clearly visible. Diverting the pressure side leg has reduced the passage vortex (PV) loss core well below BCp configuration. However diverted pressure side leg vortex formation (PSLd) is not entirely effective in reducing peak value of counter vortices (WV&TSV). The presence of strong PVi (vortex induced by passage vortex) obstructs the washing up of profile boundary layer upwards along with passage vortex. As a result, the separation of wall vortex (WV) from the suction surface happens at the later stage near to trailing edge and this leads to the strong formation of trailing edge shed vortex (TSV), together creates more intensified counter vortex loss core at midspan. Towards the endwall, peak loss regions emerges as a results of interaction between trailing edge shed vortex (TSV), diverted pressure side leg vortex (PSLd) and vortex induced by the passage vortex (PVi). Near the endwall (below 16% of span), the peak loss region exhibited by EC1p and EC2p configurations are higher compared to BCp configuration, but with EC3p configuration the peak value is smaller. The loss peak value observed for EC1p at 14% of span is due to the merging of intensified and enlarged diverted pressure side leg vortex (PSLd) with the suction side corner vortex (SScv) formed at the valley, near suction surface (light grey circle). Towards the endwall region, combined effects of diverted pressure side leg vortex (PSLd) and trailing edge - endwall corner vortex (TEcv) significantly contribute to the peak value observed at 5% (dark green circle) since it entrains hub endwall boundary layer at the aft por-

tion of the blade passage significantly. For EC3p configuration, just above the endwall, absence of pressure surface vortex (PSv) has reduced the C_{po} distribution well below BCp configuration (red circle). Also the location of peak value generated by the trailing edge corner vortex (TEcv) is shifted towards 8.8% span and it remains same as that of BCp configuration (dark grey circle). From 9.3% to 35% of span, EC3p configuration is exhibiting the same trend as that of BCp configuration. The reduced cross passage pressure gradient at hub endwall has pronounced effect at midspan also. Between 35% and 50% of span, EC3p configuration is showing peak loss core reduction of both passage vortex (PV) and counter vortices (WV&TSV) compared to BCp configuration even though the spanwise position remains same.
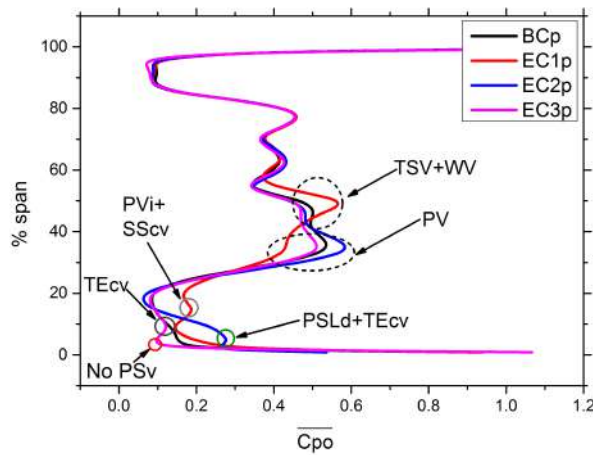
Figure 6.14: Distribution of pitch averaged total pressure loss coefficient ($\overline{C_{po}}$) in the spanwise direction at 127% C_{ax}.

Effect on pitch averaged CSKE

In Figure 6.15 pitch averaged coefficient of secondary kinetic energy (CSKE) measured at 127% C_{ax} is presented. The definition of CSKE has already explained in section 6.3.6. In EC1p configuration, CSKE has relatively increased from 8.3% to 19.1% of span followed by a reduction for rest of the span upto 41.6% due to the strong reduction in the passage vortex (PV) strength. The CSKE peak observed at 13.3% of span corresponds to PVi (vortex induced by passage vortex) rather than diverted pressure

side leg vortex (PSLd) because the latter has merged with the passage vortex (PV) upstream of the trailing edge (explained in Figure 6.10b, between plane 5 and 6). For EC2p configuration distribution of CSKE have two peak values. The peak which is close to the endwall (8.3% span) represents the existence of both trailing edge - endwall corner vortex (TEcv) and diverted pressure side leg vortex (PSLd). The second peak observed below midspan (34.5% span) represents the existence of passage vortex (PV). The maximum increase in the CSKE value towards midspan is observed for EC2p configuration. For EC3p configuration the CSKE distribution remains similar to BCp configration throughout the span. The endwall profile adopted has effectively suppressed the secondary vortices which caused additional secondary losses at near endwall region. Moreover, EC3p configuration exhibits, reduction in the CSKE peak compared to BCp configuration at 34.5% span.
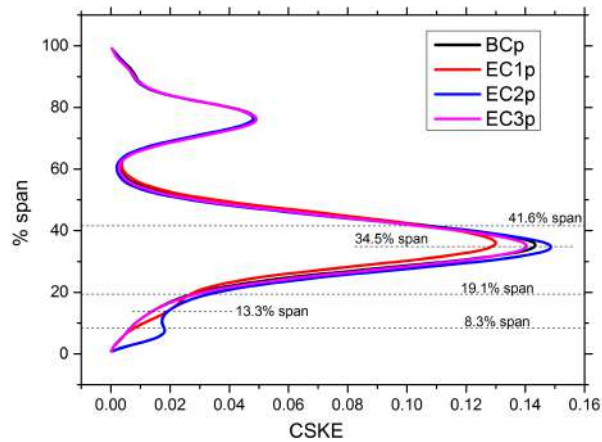
Figure 6.15: Pitch averaged coefficient of secondary kinetic energy (CSKE) in the spanwise direction at 127% C_{ax}.

6.4.7 Transient behaviour of PSB

In low aspect ratio turbine blades, pressure side bubble (PSB) formation causes a major source of unsteadiness. Analysis of pressure side separation and its evolution is crucial for the effective control of the blade passage secondary loss generation. This section

presents the unsteady behaviour of PSB and its interaction with secondary vortices at hub endwall.

Figure 6.16a and Figure 6.16b explains the comparison of mass averaged total pressure coefficient ($\overline{\overline{C_p}}$) fluctuations measured at 5% C_{ax} upstream and 5% C_{ax} downstream of purge slot as a function of time for various contoured endwall configurations. C_p can be defined as the raio of total pressure (P_t) to inlet dynamic pressure (Eq. 6.4).

$$C_p = \frac{P_t}{0.5\rho_\infty U^2} \tag{6.4}$$

In both figures, all endwall configurations other than EC1p configuration, the local minimum and local maximum of pressure fluctuation are occurred at $\tau = 0.0$ and $\tau = 0.39$ respectively where the phase shift observed for EC1p configuration is measured to be 9% of total time step. This phase shift is attributed to the blockage caused by the profile hump near the suction surface where the secondary endwall vortices and purge vortex merges. Compared to the upstream position (Figure 6.16a), the amplitude of the total pressure coefficient (C_p) perturbation curves at downstream position (Figure 6.16b) have been increased as a result of purge flow. The time averaged value of pressure coefficient at the inlet of BCp configuration has been chosen as the reference value (C_p = 2.58). A detailed examination of pressure fluctuation at the upstream region of the purge slot with respect to the reference value chosen (C_p = 2.58), shows that, for BCp and EC2p configurations, 66.4% of one time period is strongly influenced by low pressure values. For EC1p and EC3p configuration the percentage of low pressure regions observed within one time period, calculated are 61.7% and 59.7% respectively. This indicates that, EC3p configuration tries to maintain high pressure region above 40% of one time period which is the maximum compared to other configurations including base profile (BCp). Comparison of total pressure profiles at 5% C_{ax} upstream and 5% C_{ax} downstream position of purge slot at $\tau = 0.5$ is shown in Figure 6.16c. The ejected purge flow pushes the mainstream boundary layer upwards by 4% of span and the difference in the velocity magnitude (region within dark circle) enhances the entrainment

of mainstream boundary layer fluid into the additional roll up vortices generated by the purge flow. The fact that downstream pressure profile is so different from the upstream location below 10% of span reflects the complexities and non-uniformities generated by the introduction of purge flow.

(a)

(b)

(c)
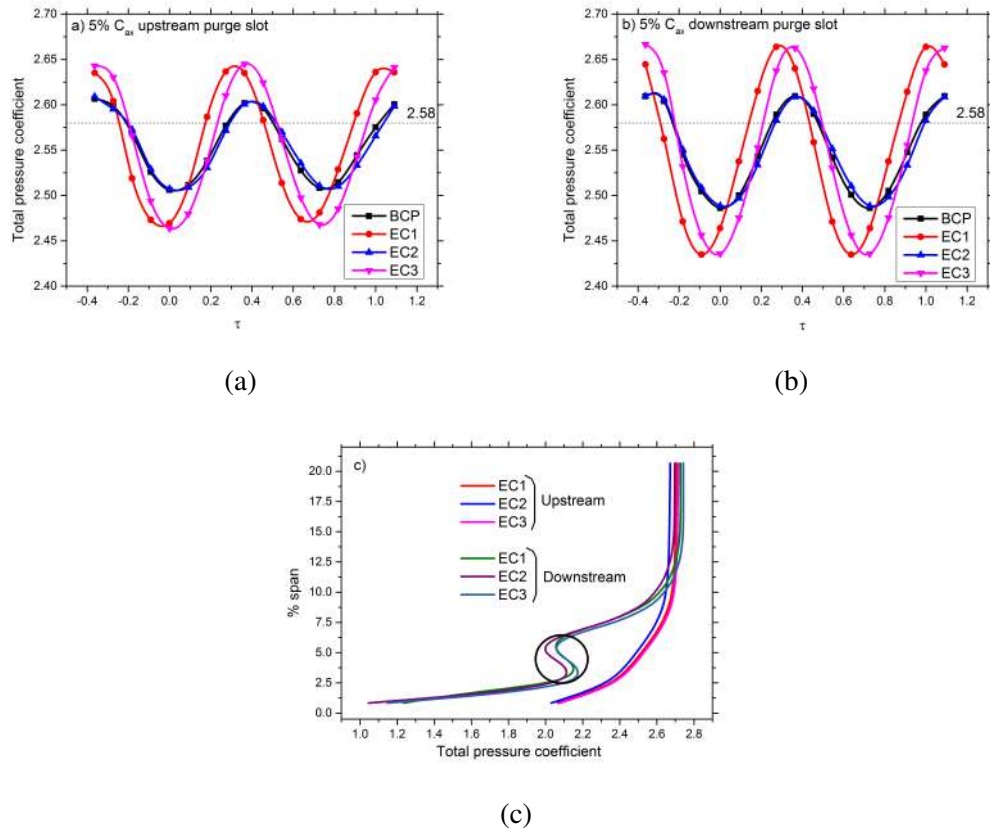
Figure 6.16: a) Mass averaged total pressure coefficient 5% C_{ax} upstream of purge slot b) Mass averaged total pressure coefficient 5% C_{ax} downstream of purge slot c) Combined upstream and downstream pressure profile.

The previous analysis of pressure perturbations upstream and downstream of purge slot have revealed the unsteadiness involved within the mainstream flow approaching the inlet of the blade passage. Figure 6.17 explains the Q-criterion iso-surface to visualize the existence of PSB and PSv on pressure surface and endwall respectively. For better understanding, reference figure (Figure A.3) is provided in the appendix and the view is straight on the upstream region of pressure surface (region inside the rectangle). In Figure 6.17, the separated boundary layer can be observed as a thin layer of vortex

instabilities extending along the span on the pressure surface just downstream of leading edge. As time progresses, the width of the pressure side bubble (PSB) increases until the tail end of this vortex breakdown and convects towards hub endwall. Fluid above the region of split migrates towards shroud. The upward shifting and the reduction of total pressure of mainstream boundary layer at the hub endwall due to the ejection of purge flow are the major reasons related to the asymmetrical nature of pressure side bubble (PSB) migration in the spanwise direction. In BCp configuration, the low momentum fluid within the PSB is convected in the direction of reduced static pressure. The driving force and direction depends on the length, size and shape of the bubble. The changes inside the PSB are characterized by growth, eventual breakdown and migration of vortices. Significant unsteadiness is observed at the reattachment region (R) while the separation region (S) remains unchanged. While migrating towards the endwall, the low momentum fluid inside the pressure side bubble (PSB) extracts energy from the surrounding free stream which leads to more aerodynamic losses at the blade exit region. Similar observations regarding pressure side bubble (PSB) formations are reported by Jenny *et al.* (2011) and Brear *et al.* (2002).

Static pressure coefficient (C_{ps}) contours on the pressure surface of BCp configuration, superimposed with surface streamlines are shown in Figure 6.18. Pressure side bubble (PSB) is generated as a result of adverse pressure gradient between the pressure surface and leading edge. Whereas the formation of pressure surface vortex (PSv) is related to the spanwise pressure gradient existing between midspan and endwall region close to the upstream portion of pressure surface and blade passage respectively. The low pressure zone observed on the leading edge along the span (5% to 20% of span) is related to the splitting and acceleration of incoming secondary vortices around the leading edge. The static pressure coefficient (C_{ps}) has decreased gradually and reaches minimum just above the hub endwall (region between 5% and 20% span) where the incoming mainstream boundary layer, which is pushed upwards by the purge flow, interacts with the leading edge and horseshoe vortex is formed. The unsteady periodic nature associated with the high pressure zone generated over the pressure surface cause
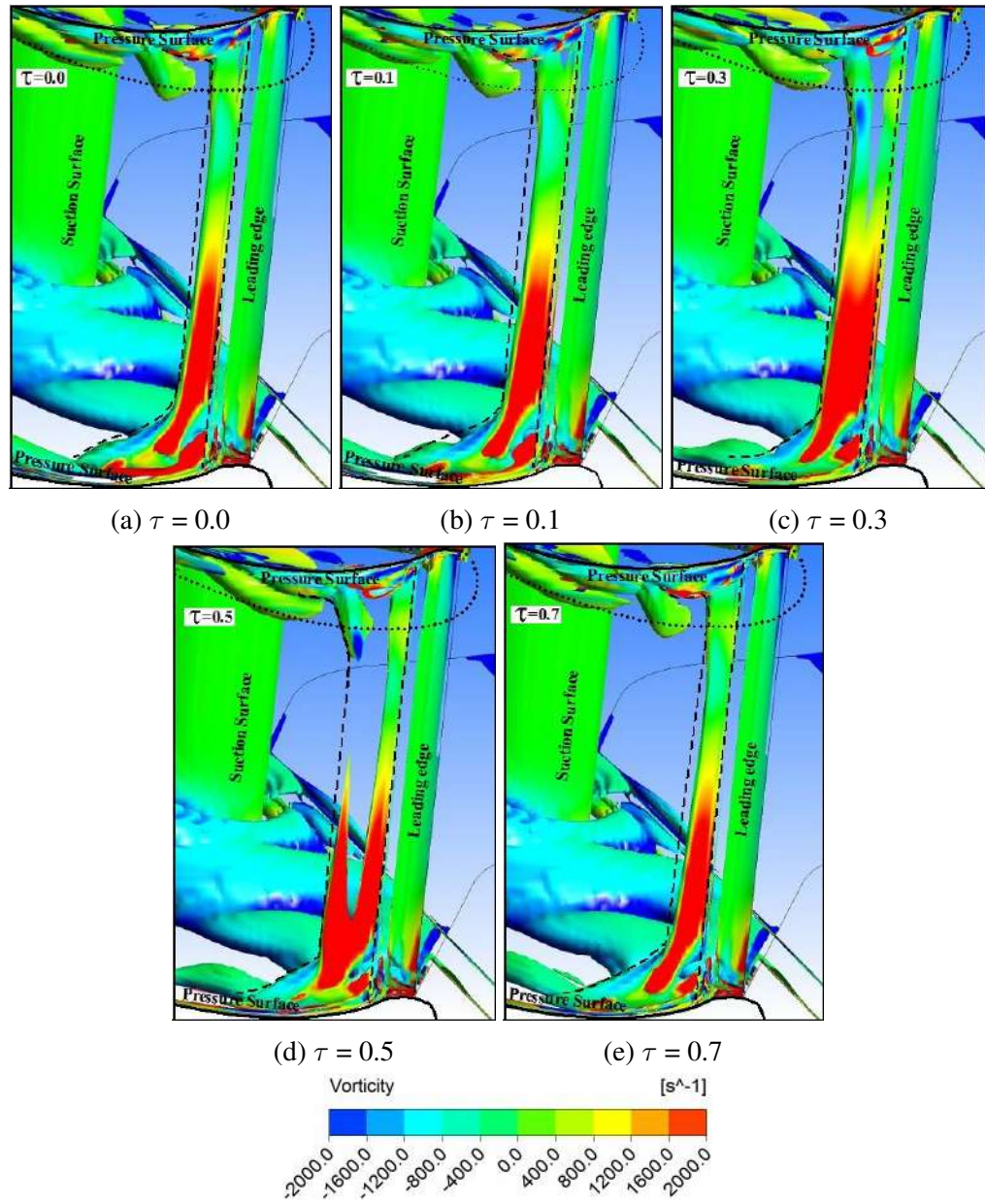
Figure 6.17: Evolution of pressure side bubble (PSB) described using Q-criterion for BCp configuration at a) $\tau = 0.0$ b) $\tau = 0.1$ c) $\tau = 0.3$ d) $\tau = 0.5$ e) $\tau = 0.7$.

the trailing edge of the pressure side bubble (PSB) to break at particular interval of time. The C_{ps} distribution on the pressure surface increases until $\tau = 0.36$ and then decreases up to $\tau = 0.72$. While increasing, the strong streamwise pressure gradient causes the pressure side bubble (PSB) to increase in width. While decreasing, at a particular time

step ($\tau = 0.54$), the presence of C_{ps} local maximum at a span of 70% causes the trailing edge of pressure side bubble (PSB) to reattach first and the reattachment process will continues till $\tau = 0.72$ until the pressure side bubble (PSB) regains the minimum width. In all figures, below 20% span, the width of the pressure side bubble (PSB) increases till 44% C_{ax}. While analyzing the hub endwall, the surface streamlines close to the pressure surface (10% to 40% C_{ax}) reveals the strong entrainment of the fluid within the pressure side bubble (PSB) into the pressure side leg vortex (PSL). The blockage effect generated by the purge flow and the formation of pressure side leg vortex (PSL) within the blade passage has drastically reduced the total pressure near the pressure surface-endwall junction (region within white doted ellipse) which stimulates the pressure side bubble (PSB) fluid from the pressure surface to migrate downwards and merge with the pressure side leg vortex (PSL) over the endwall. The curved streamlines over the endwall (between 15% and 20% C_{ax}) with apex pointing upstream confirms the above observed entrainment phenomenon.

Figure 6.19 presents the near wall flow structures of EC3p configuration using surface streamlines and local C_{ps} contours on pressure surface and hub endwall. For the EC3p configuration the formation and trajectory of purge vortex and pressure side leg of horseshoe vortex (PSL) seems similar to that of BCp configuration. For the contoured endwall, the position of the profile hump has significantly increased C_{ps} distribution over pressure surface and endwall (region within white doted ellipse). Because of the presence of profile hump, the diverted pressure side leg vortex (PSLd) oriented in the axial direction remains more attached to the pressure surface. The impact of increase in the C_{ps} distribution at endwall has reflected all over the pressure surface also. Further analyzing the orientation of streamlines over the pressure surface, it can be observed that, the stretching of the high pressure region till leading edge has kept the streamlines continuous and perfectly attached during entire time-steps. This leads to a significant reduction in the spanwise pressure gradient particularly at the region where pressure side bubble (PSB) has been observed in BCp configuration. Comparison of streamlines and magnitude of C_{ps} distribution on pressure surface of both BCp and EC3p configura-
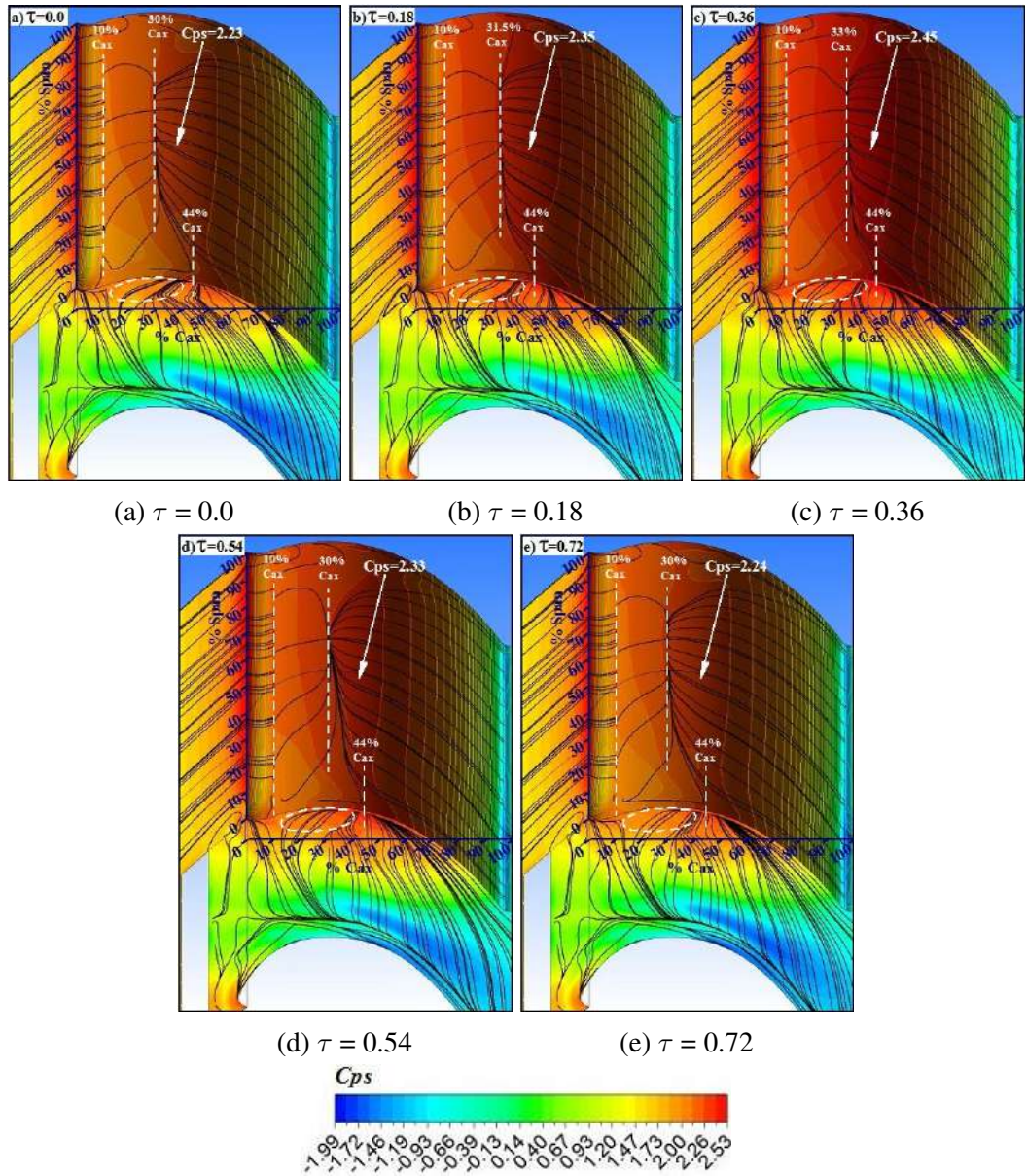
Figure 6.18: Transient variation of static pressure coefficient (C_{ps}) distribution over the endwall and pressure surface superimposed with surface streamlines for BCp configuration at a) $\tau = 0.0$ b) $\tau = 0.18$ c) $\tau = 0.36$ d) $\tau = 0.54$ e) $\tau = 0.72$.

tions reveals that contoured endwall has eliminated the PSB formation significantly. As a result, the streamlines which represent pressure side bubble (PSB) over the endwall in BCp configuration, are directed in the pitchwise direction rather than going backwards. However, in EC3p configuration, due to the formation of PSL, behind the purge vor-

tex, a small region of separation (dotted black circle) on the pressure surface could be observed.

(a) $\tau = 0.0$ (b) $\tau = 0.18$ (c) $\tau = 0.36$
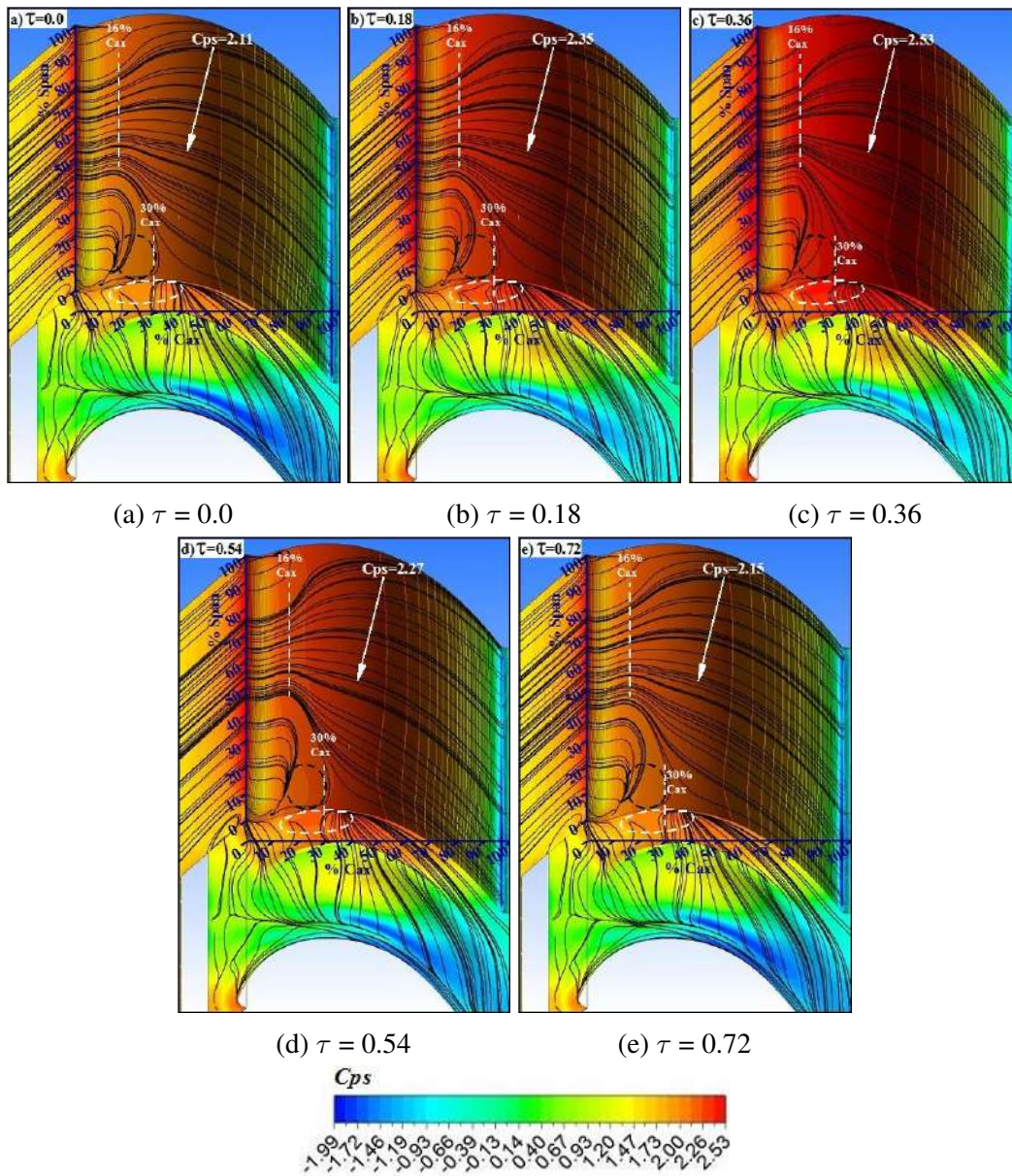
(d) $\tau = 0.54$ (e) $\tau = 0.72$

Figure 6.19: Transient variation of static pressure coefficient (C_{ps}) distribution over the endwall and pressure surface superimposed with surface streamlines for EC3p configuration at a) $\tau = 0.0$ b) $\tau = 0.18$ c) $\tau = 0.36$ d) $\tau = 0.54$ e) $\tau = 0.72$.

Distribution of axial velocity component, non-dimensionalized with mass averaged inlet velocity is presented in Figure 6.20 for three cases: a) base case without purge
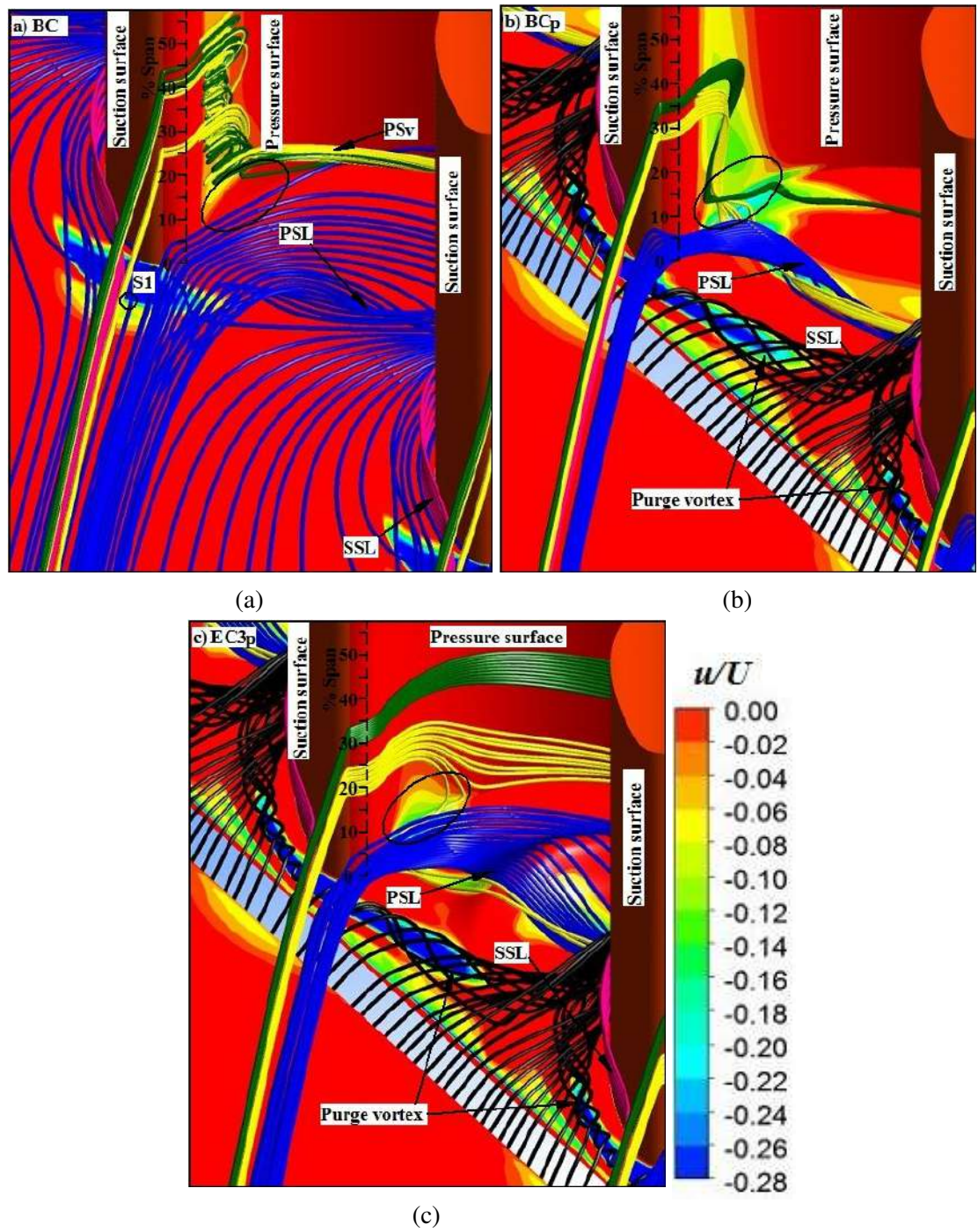
Figure 6.20: Comparison of 3D streamlines superimposed with non-dimensionalized axial velocity contour between a) BC, b) BCp c) EC3p configurations at $\tau = 1.5$.

(BC), b) with purge (BCp) and c) with purge and endwall profile (EC3p). The three dimensional nature of boundary layer fluid over hub endwall and blade surfaces espe-

cially within the pressure side bubble (PSB) and its related flow physics are explained using 3D streamlines. Blue color streamlines indicates endwall boundary layer fluid where yellow and green represents fluid from core portion and trailing edge region of pressure side bubble (PSB) respectively. In Figure 6.20a, the presence of negative velocity over the pressure surface immediately downstream of leading edge, confirms the existence of pressure side separation. At the pressure surface - endwall junction (region within the ellipse), the mainstream endwall streamlines (blue) accelerating along the leading edge (2.5% to 5% span) tries to keep attached to the endwall till pressure surface - endwall corner, all through the passage. However the spanwise pressure gradient existing between the region just above the endwall and midspan causes the low momentum fluid within the PSB to migrate downwards and detaches from the pressure surface as pressure surface vortex (yellow streamlines). In BC configuration the two dimensional pressure side bubble (PSB) does not have any obvious effects on the endwall secondary vortex structures. In BCp configuration, negative u component of velocity distribution (dark blue colored contour region) downstream of the purge slot near to both suction and pressure surfaces represents the rolling up of purge vortex (Fig 6.20b). Due to pitchwise pressure gradient, the region near the pressure surface, enlarge and extents till midst of the blade passage while region near to suction surface diminishes immediately after moving a little away from the suction surface. However both legs merge near the suction surface and form a single vortex. The upward shifting of incoming mainstream boundary layer has caused the pressure side leg vortex (PSL) to originate within the blade passage (region within the ellipse) rather than from upstream of leading edge as in Figure 6.20a. The loss zone of pressure side bubble (PSB) extends till endwall where the pressure side leg vortex (PSL) originates. As fluid within the pressure side bubble (PSB) has low relative momentum, it responds to the endwall cross flow effortlessly. The pressure side leg vortex (PSL) acts as a tunnel like vortical structure which wraps and assists the pressure side bubble (PSB) fluid to travel across the passage. Once it reaches the suction side, it combines with the passage vortex. In general introduction of purge flow has caused the mainstream fluid to do additional

work to accelerate these secondary vortices (PSL and PSB) within the blade passage. However, in EC3p configuration the enhancement of static pressure coefficient at endwall between the profile hump and pressure surface has provided more axial momentum to the endwall boundary layer fluid close to the pressure surface. This is evident from the substantial reduction of negative u component of velocity which resembles adverse pressure gradient on both endwall and pressure surface (Figure 6.20c). Due to this, the pressure side leg vortex (PSL) streamlines (blue) on the endwall, seems scattered over the profile hump in EC3p configuration. This is in contrast with the BCp configuration where the streamlines are concentrated. As a result, in EC3p configuration, elimination of pressure side bubble (PSB) as well as pressure surface vortex (PSv) made the streamlines (green and yellow) trapped inside the pressure side bubble (PSB) in EC1p and EC2p configurations, oriented straight till trailing edge.

6.5   Summary

- In an effort to reduce the secondary losses, three different contoured endwall configurations are investigated with and without purge flow.

- The aim of hump region of the contoured endwall is to locally accelerate and the valley region is to locally decelerate the flow.

- The presence of profile hump has redirected the pressure side leg vortex (PSL) more axially and subsequently referred as diverted pressure side leg vortex (PSLd).

- The stagnation region generated at the valley region of contoured endwall has caused additional aerodynamic penalty.

- Transient analysis revealed the growth, eventual breakdown, migration and conversion of pressure side bubble (PSB) to pressure surface vortex (PSv).

- Periodically varying static pressure distribution on the pressure surface causes the tail end of the pressure side bubble (PSB) to break at particular interval of time.

- Low momentum fluid from the core region of the pressure side bubble (PSB) rolls up into the pressure side leg vortex (PSL) and together migrate across the blade passage.

- In EC3 and EC3p configurations, increased static pressure distribution over the endwall by the hump region has eliminated pressure side bubble (PSB) and pressure surface vortex (PSv) in an effective manner.

CHAPTER 7

CONCLUSIONS AND SUGGESTIONS FOR FUTURE WORK

7.1   CONCLUSIONS

The effect of the purge flow on film cooling and aerodynamic characteristics of the endwall is numerically investigated by using three-dimensional Reynolds-averaged Navier-Stokes equations coupled with the SST turbulence model. The validation of numerical method shows that the numerical results are in good agreement with the experimental data. Coolant ejection can increase the intensity of horseshoe vortex. Interaction between the mainstream flow and purge flow leads to additional vortex formation upstream of blade leading edge. It has strengthened the endwall flow by increasing the penetration depth of the passage vortex and the deviation of the exit flow angle. A study has been carried out on the effect of purge flow ejection angles on loss coefficient and exit yaw angle deviation. Meanwhile reducing the ejection angle has caused significant reduction in the pressure loss coefficient due to the strong flow acceleration of purge flow. The high momentum fluid ejecting out of purge slot has reduced the flow turbulence near to the endwall. The percentage variation of $\overline{\overline{C_{po}}}$ for 90^0 purge with base case at 50% C_{ax} is 88.6%. On other hand percentage variation for 30^0 and 45^0 purges are 23.8% and 35.5% respectively. Comparing all purge cases 30^0 and 45^0 ejection angles shows smaller losses, indicating that the ideal ejection angle may lie between these two purge angles. Generally, lowering the ejection angle minimizes secondary losses. However implementation of lower ejection angles will be a strenuous task for the engine designers and it may shatter the benefits derived from it. All purge flow cases exhibits significant flow deviation in comparison with the base case. Secondary

flow has restricted most of the coolant ejection to suction side, leaving pressure side unprotected. Compared to 90^0, 45^0 purge provides wider coolant coverage and more effectiveness. At lower ejection angle and higher velocity ratio, upstream and middle part of blade passage are fully protected. The increase of pitch averaged FCE at blade leading edge is as high as 55.8% when the purge ejection angle α is reduced from 90^0 to 30^0 for M=0.6. Also reduction of α to 45^0 from 90^0 has increased the FCE by 41.7% for velocity ratio of 0.6.

The interaction of upstream wakes with the purge flow inside a turbine blade cascade has been numerically investigated in the presence of upstream wakes generated from a cylindrical rod. The generation of wake from four pitchwise locations has been analyzed separately and subsequent modifications in the secondary flow has been investigated. It is observed that shifting of upstream cylinder from SSW to STW configuration has a huge influence on the downstream exit flow angle deviation which can definitely alter the flow characteristics of succeeding blade rows. The merging point of suction side leg and pressure side leg of horseshoe vortex shift towards the aft part of blade passage under the influence of cylinder vortices. The unsteady analysis revealed the formation of filament type vortical structures and its propagation inside the blade passage. In STW configuration, these vortical structures splits across blade leading edge into two legs having different rotational directions. The formation of pressure surface vortices (PSv) and its interaction with the blade trailing edge wake regions amplify blade exit unsteadiness and caused additional loss generation compared to MW configuration. Apart from these vortex filaments, at endwall, the cylinder itself generates horseshoe vortex, which interacts with the pressure side leg of horseshoe vortex (PSL) and leads to the alternate rolling of PSL from leading edge to trailing edge. In MW configuration, the horseshoe vortex generated by the cylinder is broken by the purge flow. The obstruction created by the purge flow caused the upper portion of cylinder vortices to bend forward, creating a shearing action along the spanwise direction. The unsteady analysis revealed that, in STW configuration, the frequency of formation of pressure surface vortices at midspan is smaller than near the endwall. Present numeri-

cal investigation confirms that, interaction of upstream wakes with purge flow plays a major role in the evolution of secondary flow within the blade passage and blade exit region for a low aspect ratio turbine blade.

The interaction of the purge flow with the main stream flow causes additional secondary flow losses and to curb this different endwall profiles are tested. Detailed numerical investigations are carried out to understand physical mechanism behind the secondary flow modifications caused by the endwall contouring in a linear turbine cascade with an upstream purge flow. It is found that the application of non-axisymmetric endwall profiles, in a low aspect ratio turbine blade, resulted in less intensified secondary vortex structures. It is observed that the hump region of the endwall profile limits the static pressure through local acceleration and the valley region enhanced local static pressure through flow diffusion. The contouring diverts the pressure side leg vortex (PSL) into axial direction rather than moving towards suction surface thereby reducing the strength of passage vortex. The peak to valley height is found to be a critical parameter in controlling the static pressure gradient over the endwall. In the EC1p configuration a stagnation zone is generated at the valley region, which made the purge vortex to turn around at the convex region of the hump leading to an early formation of passage vortex. Additionally the flow acceleration achieved by the diverted pressure side leg (PSLd) and the formation of strong PVi (vortex induced by passage vortex) enhanced the loss coefficient at the blade exit. Moreover presence of PVi has delayed the detachment of wall vortex from the suction surface at the trailing edge which in turn resulted in the enhancement of trailing edge shed vortex (TSV). The stagnation zone generated within the valley in EC1p and EC2p profiles creates more aerodynamic penalty at the blade exit. Near the endwall (below 16% of span), the peak loss region exhibited by EC1p and EC2p configurations are higher compared to base case configuration. With EC3p profile, reduction in the local static pressure is achieved from the local acceleration gained by the secondary vortices over the convex curvature. The presence of hump near to pressure surface has kept the surface streamlines more attached to the pressure surface which resulted in the reduction of spanwise pressure gradient

thereby eliminating pressure side bubble formation and related pressure surface vortex. It is found that the unsteadiness related to pressure side bubble (PSB) is an important factor which can influence the endwall secondary vortex formations. Fluid from the core region of PSB migrates downwards to the endwall and combines with the pressure side leg of horseshoe vortex (PSL). It is important to note that the trailing edge of pressure side bubble, which breaks periodically causes the formation of pressure surface vortex. The formation and migration of PSB is related to the streamwise and spanwise pressure gradient existing on the pressure surface. It is observed that the migration of pressure side bubble (PSB) towards the endwall and then across the passage along with pressure side leg of horseshoe vortex (PSL) has generated additional aerodynamic penalty. In this scenario, non-axisymmetric endwall contouring which can effectively eliminate pressure side bubble, plays a major role in minimizing the above mentioned aerodynamic penalty to a large extend. The results presented in this work depend on specific turbine geometry and stationary upstream wakes. Hence care should be taken while generalizing the results.

7.2 SUGGESTIONS FOR FUTURE WORK

The present study is undertaken on a linear turbine cascade. As a future prospect the study may be extended to an annular cascade wherein the rotational effects are also present. Further, more complex endwall contours may be examined in future for achieving further loss reduction.

APPENDIX A

ADDITIONAL DETAILS RELATED TO EXPERIMENTAL AND NUMERICAL WORK

A.1   Blowing ratio and Pressure ratio

Blowing ratio can be measured as the product of density ratio (DR) and velocity ratio (M).

Table A.1: Blowing ratio

Velocity ratio	Blowing ratio
0.2	0.18
0.4	0.37
0.6	0.56
0.8	0.74
1.0	0.92

Pressure ratio can be defined as the ratio of coolant inlet total pressure (P_{tc}) to mainstream inlet total pressure $(P_{t\infty})$.

Table A.2: Pressure ratio

Velocity ratio	Pressure ratio
0.2	0.72
0.4	0.77
0.6	0.82
0.8	0.87
1.0	0.93

A.2 Reference figures

A.2.1 Reference figure for underturning and overturning
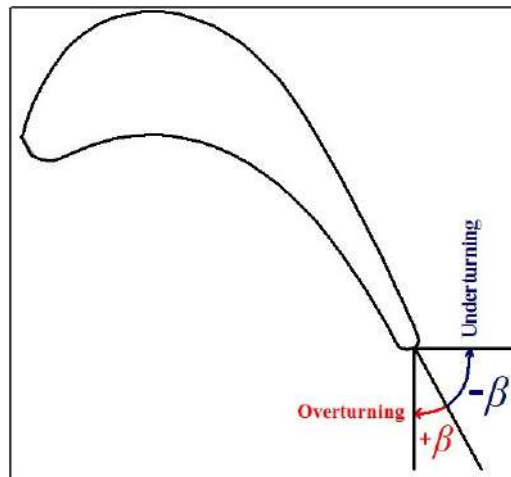
Figure A.1: Orientation of underturning and overturning with respect to exit design angle β.

A.2.2 Reference figure for streamwise vorticity
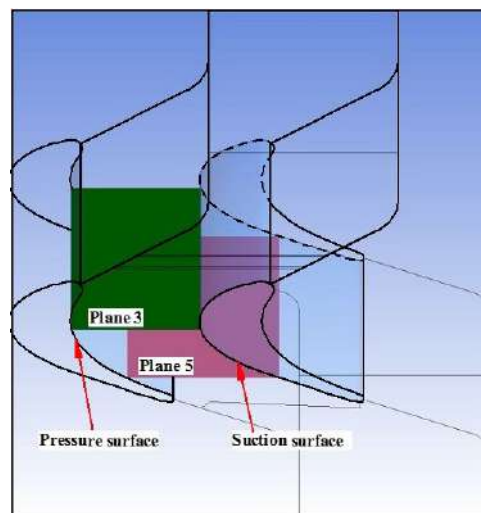
Figure A.2: Orientation of computational domain while explaining streamwise vorticity.

A.2.3 Reference figure for PSB evolution
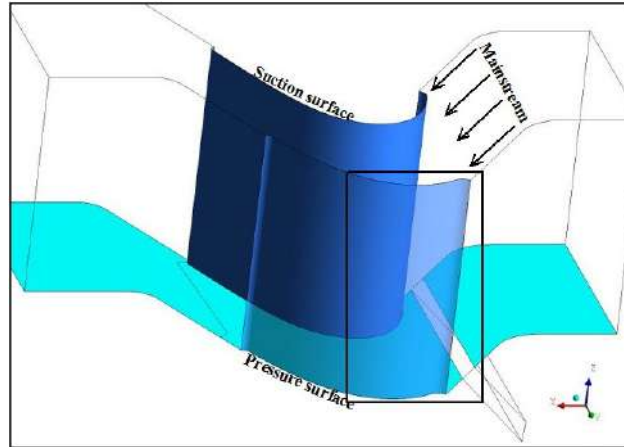
Figure A.3: Orientation of computational domain while explaining pressure side bubble using Q criterion.

A.3 Uncertainties in experimental values

In general its impossible to measure a physical quantity with 100% confidence level. Whenever we repeat the measurement, we will obtain a different value. The difference between the true value and measured value can be referred to as errors. However the error can be minimized by providing extra care while designing the experimental setup and applying more sophisticated and refined measuring instruments. Errors can be classified as systematic errors and random errors. The systematic errors can be related to the accuracy of the measurement. Accuracy can be defined as, how close the measured value to the true value. Systematic errors could not be reduced by repeating the experiment. This type of error is difficult to identify statistically. But once identified it can be reduced by using refined measuring instruments. Improper calibration and poor maintenance of measuring instruments are the major cause of systematic errors. On the other hand, random errors referred to the precision of the measured values. Precision means, how close the measured values are. It can be cross checked with repeating the experiments.

A.3.1 Uncertainty related to total pressure loss coefficient (C_{po})

$$\Delta C_{po}^2 = \left(\frac{\frac{\rho_\infty A_\infty U \rho_c A_c U_c (\overline{\overline{P_{t,\infty}}} - \overline{\overline{P_{t,c}}})}{2(\rho_\infty A_\infty U + \rho_c A_c U_c)^2} - \frac{\overline{\overline{P_{t,\infty}}} \rho_\infty A_\infty U + \overline{\overline{P_{t,c}}} \rho_c A_c U_c}{\rho_\infty A_\infty U + \rho_c A_c U_c} - P_t}{\frac{1}{4}\rho_\infty U^3} * \Delta U \right)^2$$

$$+ \left(\frac{\frac{\rho_c A_c \rho_\infty A_\infty U (\overline{\overline{P_{t,c}}} - \overline{\overline{P_{t,\infty}}})}{(\rho_\infty A_\infty U + \rho_c A_c U_c)^2}}{\frac{1}{2}\rho_\infty U^2} * \Delta U_c \right)^2 + \left(\frac{-2}{\rho_\infty U^2} * \Delta P_t \right)^2 \tag{A.1}$$

A.3.2 Uncertainty related to coefficient of discharge (C_d)

$$\Delta C_d^2 = \left(\frac{A_e(\rho_c(A_i^2 - A_t^2))^{0.5}}{A_i A_t \sqrt{2(P_1 - P_2)}} * \Delta U_c \right)^2$$

$$+ \left(\frac{A_e U_c \sqrt{\rho_c(A_i^2 - A_t^2)} * (P_1 - P_2)^{\frac{-3}{2}}}{2\sqrt{2} A_i A_t} * \Delta(P_1 - P_2) \right)^2 \tag{A.2}$$

Table A.3: Uncertainty in exit velocity (U_e).

P_t	P_s	U_e	ΔU_e	ΔU_e (%)
497.721069	-58.733463	30.857561	0.006948017	0.022516418
491.49646	-55.689529	30.59949355	0.006915279	0.022599326
456.233612	-50.40451	29.44392392	0.006668981	0.022649771
389.306488	-37.013626	27.00938316	0.006193905	0.02293242
301.970276	-14.322056	23.26435873	0.005558973	0.023894803
295.090363	-9.972792	22.84765504	0.005528341	0.024196533
327.731079	-7.113609	23.93693062	0.00585848	0.024474651
393.140717	-7.433685	26.18112781	0.006424966	0.024540447
442.662231	-5.536686	27.69377476	0.006838452	0.024693102
468.356995	7.276001	28.08894092	0.007133909	0.025397572
486.824738	10.789086	28.54082313	0.007298713	0.025572889
494.20755	13.187404	28.68985724	0.007371724	0.02569453
				Continued on next page

Table A.3 – continued from previous page

P_s	P_s	U_e	ΔU_e	ΔU_e (%)
497.774017	9.3198	28.91070524	0.007366873	0.02548147
499.702911	-1.442572	29.28388309	0.007299927	0.02492814
501.824493	-5.493611	29.4636763	0.007286592	0.024730764
500.909027	-10.46829	29.58131556	0.007245523	0.024493578
500.990814	-13.335458	29.66648611	0.007226882	0.024360425
502.506531	-17.183802	29.82078513	0.0072129	0.024187493
500.785675	-18.503344	29.80926884	0.00719168	0.02412565
501.346161	-20.797131	29.89107992	0.007181298	0.024024887
503.510864	-21.30962	29.9676124	0.007194139	0.02400638
502.84314	-21.550251	29.95541627	0.007187687	0.023994616
502.494812	-21.906395	29.95563951	0.007182883	0.023978401
500.663666	-23.293541	29.9429554	0.007160683	0.023914417
499.47757	-22.186611	29.87736296	0.007158718	0.023960342
477.045166	-88.150642	31.09898539	0.006673253	0.021458105
480.334869	-82.290657	31.028192	0.006718971	0.021654407
477.30484	-71.52668	30.64546934	0.006737294	0.021984634
470.61615	-25.955481	29.14994278	0.00691707	0.023729273
442.666718	-7.239685	27.74647656	0.006825911	0.024601001
399.809235	11.582652	25.77444895	0.00663864	0.025756671
404.117889	13.778658	25.84448339	0.00669308	0.02589752
362.027924	4.412809	24.73743622	0.006261136	0.025310369
357.645569	-14.426825	25.23251142	0.006068466	0.024050187
367.678925	-25.200216	25.92843117	0.006080561	0.023451328
392.678497	27.762119	24.9886867	0.006739224	0.0269691
394.139679	-57.025078	27.78525186	0.006131517	0.022067525
431.542938	-56.233974	28.89065407	0.006444014	0.022304839
				Continued on next page

Table A.3 – continued from previous page

P_s	P_s	U_e	ΔU_e	ΔU_e **(%)**
469.346283	-57.741779	30.03228276	0.006735976	0.022429118
481.781006	-54.104897	30.28188603	0.006848914	0.022617199
485.889038	-52.575912	30.35466707	0.006887678	0.022690672
485.972961	-53.742241	30.38988661	0.006882655	0.022647848
494.202881	-13.593098	29.47754989	0.00717483	0.024339981
482.926514	-21.326239	29.37452775	0.007039904	0.023966016
482.045258	-19.766226	29.30333515	0.007043185	0.024035438
485.202148	-22.673077	29.47984991	0.007048628	0.023909987
486.679199	-24.730989	29.58226628	0.00704701	0.023821737
490.282288	-26.751614	29.74447204	0.007061858	0.02374175
494.235046	-28.006147	29.89388205	0.007084038	0.023697283
487.86911	-53.261822	30.42971845	0.006899406	0.022673249
			Max value	0.0269691

Table A.4: Uncertainty in coefficient of discharge (C_d).

Q_{act}	Q_{th}	C_d	ΔC_d	ΔC_d **(%)**
0.001632	0.005840	0.279360	0.004338	1.087247
0.001799	0.006392	0.281420	0.003964	0.986235
0.002128	0.007372	0.288681	0.003437	0.833710
0.002255	0.009125	0.247104	0.002777	0.786916
0.002382	0.008381	0.284161	0.003024	0.745102
0.002686	0.009555	0.281064	0.002652	0.660852
0.002888	0.005311	0.543847	0.004773	0.614545
0.003091	0.010248	0.301604	0.002473	0.574316
				Continued on next page

144

Table A.4 – continued from previous page

Q_{act}	Q_{th}	C_d	ΔC_d	ΔC_d (%)
0.003471	0.011848	0.292958	0.002140	0.511561
0.003648	0.014024	0.260146	0.001808	0.486755
0.003800	0.013085	0.290434	0.001938	0.467337
0.003952	0.014579	0.271092	0.001739	0.449415
0.004104	0.012495	0.328479	0.002029	0.432822
0.004358	0.015372	0.283490	0.001650	0.407745
			Max value	1.087247

Table A.5: Uncertainty in total pressure loss coefficient (C_{po}).

C_{po}	ΔC_{po}	ΔC_{po} (%)
0.444369342	0.00274616	0.617990493
0.613691605	0.002629572	0.428484265
0.869786234	0.002454719	0.282220951
0.792063032	0.002507579	0.316588336
0.45849533	0.002736407	0.596823298
0.30312737	0.002843929	0.938196055
0.299809583	0.002846231	0.94934618
0.432611633	0.002754282	0.636663875
0.633015411	0.002616313	0.413309517
0.880932424	0.002447154	0.277791368
0.627879309	0.002619836	0.417251542
0.434848829	0.002752736	0.633032952
0.308287997	0.002840349	0.921329793
0.427356962	0.002757913	0.645341707
Continued on next page		

145

C_{po}	$\Delta\, C_{po}$	$\Delta\, C_{po}$ **(%)**
0.595602041	0.002641993	0.44358362
0.774234481	0.002519731	0.325448049
0.578690522	0.002653613	0.458554784
0.339764039	0.002818527	0.829554198
0.36564871	0.002800597	0.76592558
0.447109559	0.002744268	0.613779748
0.391277887	0.002782859	0.711223079
0.289924428	0.00285309	0.984080676
0.301542913	0.002845028	0.943490338
0.35007831	0.002811381	0.803071917
0.296818423	0.002848306	0.959612343
0.27600456	0.002862753	1.037212177
0.328524752	0.002826317	0.860305531
0.28094267	0.002859325	1.017760886
0.304984016	0.002842641	0.932062298
0.433720483	0.002753516	0.634859549
0.474221655	0.002725554	0.574742665
0.581494575	0.002651686	0.456012145
0.493392133	0.002712333	0.549731622
0.281881305	0.002858673	1.014140691
0.291432516	0.002852044	0.978629186
0.492751054	0.002712775	0.550536534
0.728005992	0.002551284	0.350448271
0.767766846	0.002524142	0.328764091
0.69099641	0.00257659	0.372880415
0.551127223	0.002672568	0.484927546
		Continued on next page

C_{po}	ΔC_{po}	ΔC_{po} (%)
0.406727936	0.002772172	0.681579073
	Max value	1.037212177

A.4   Q criterion

Q criterion is one of the commonly used vortex visualization method in computational fluid dynamics. It can be defined as the relative difference between the rotation dominated region and straining region within the flow field. Q criterion can be formulated from the definition of velocity gradient tensor $\partial u_i/\partial x_j$ which has two parts

$$\frac{\partial u_i}{\partial x_j} = \frac{1}{2}\left[\left(\frac{\partial u_i}{\partial x_j} + \frac{\partial u_j}{\partial x_i}\right)\right] + \frac{1}{2}\left[\left(\frac{\partial u_i}{\partial x_j} - \frac{\partial u_j}{\partial x_i}\right)\right] \tag{A.3}$$

where the symmetric part will be denoted as S and is known as the strain rate tensor defined by

$$S = \frac{1}{2}\left[\left(\frac{\partial u_i}{\partial x_j} + \frac{\partial u_j}{\partial x_i}\right)\right] \tag{A.4}$$

and the asymmetric part denoted as Ω is known as the rotation rate or vorticity tensor defined by

$$\Omega = \frac{1}{2}\left[\left(\frac{\partial u_i}{\partial x_j} - \frac{\partial u_j}{\partial x_i}\right)\right] \tag{A.5}$$

remembering the expression of the viscous stress tensor

$$\tau = \mu \left[\left(\frac{\partial u_i}{\partial x_j} + \frac{\partial u_j}{\partial x_i} \right) \right] \tag{A.6}$$

it can be inferred that the stress tensors are functions of strain rate only. From this inference Q is then defined as the second invariant of the velocity gradient tensor

$$Q = \frac{1}{2} \left(||\Omega||^2 - ||S||^2 \right) \tag{A.7}$$

Positive values of Q in the above equation indicate locations in the flow field where vorticity dominates, while negative values of Q indicate places where strain rate or viscous stress dominate.

REFERENCES

Abraham, S., K. Panchal, S. V. Ekkad, W. Ng, A. S. Lohaus, and A. Malandra, Effect of endwall contouring on a transonic turbine blade passage: Part 1: Aerodynamic performance. *In Turbo Expo: Power for Land, Sea, and Air* volume44748. American Society of Mechanical Engineers, 2012.

Acharya, S. and G. Mahmood (2006). Turbine blade aerodynamics. *The Gas Turbine Handbook*, 1, 364–380.

Aizon, W. G. W., K.-i. Funazaki, and T. Miura (2013). Purge flow effect on aerodynamics performance in high-pressure turbine cascade. *Journal of Mechanical Science and Technology*, 27(6), 1611–1617.

Asghar, A., W. Allan, M. LaViolette, and R. Woodason, Influence of a novel 3d leading edge geometry on the aerodynamic performance of low pressure turbine blade cascade vanes. *In Turbo Expo: Power for Land, Sea, and Air* volume45622. American Society of Mechanical Engineers, 2014.

Atkins, M. (1987). Secondary losses and end-wall profiling in a turbine cascade. *Institution of Mechanical Engineers*, 87.

Bagshaw, D., G. Ingram, D. Gregory-Smith, and M. Stokes (2005). An experimental study of reverse compound lean in a linear turbine cascade. *Proceedings of the Institution of Mechanical Engineers, Part A: Journal of Power and Energy*, 219(6), 443–449.

Barigozzi, G., G. Benzoni, G. Franchini, and A. Perdichizzi (2006). Fan-shaped hole effects on the aero-thermal performance of a film-cooled endwall. *Journal of Turbomachinery*, 128, 43–52.

Barigozzi, G., G. Franchini, A. Perdichizzi, M. Maritano, and R. Abram (2013). Purge flow and interface gap geometry influence on the aero-thermal performance of a rotor blade cascade. *International Journal of Heat and Fluid flow*, 44, 563–575.

Barigozzi, G., G. Franchini, A. Perdichizzi, M. Maritano, and R. Abram (2014). Influence of purge flow injection angle on the aerothermal performance of a rotor blade cascade. *Journal of Turbomachinery*, 136(4), 041012.

Barigozzi, G., G. Franchini, A. Perdichizzi, and M. Quattrore (2010). Endwall film cooling effects on secondary flows in a contoured endwall nozzle vane. *Journal of Turbomachinery*, 132(4), 955–965.

Barigozzi, G., G. Franchini, A. Perdichizzi, and S. Ravelli (2012*a*). Effects of trenched holes on film cooling of a contoured endwall nozzle vane. *Journal of Turbomachinery*, 134(4).

Barigozzi, G., A. Perdichizzi, and S. Ravelli (2012*b*). Pressure side and cutback trailing edge film cooling in a linear nozzle vane cascade at different mach numbers. *Journal of Turbomachinery*, 134(5).

Becz, S., M. Majewski, and L. Langston, Leading edge modification effects on turbine cascade endwall loss. *In Turbo Expo: Power for Land, Sea, and Air* volume 36894. 2003.

Becz, S., M. S. Majewski, and L. S. Langston, An experimental investigation of contoured leading edges for secondary flow loss reduction. *In Turbo Expo: Power for Land, Sea, and Air* volume 41707. 2004.

Behr, T., A. I. Kalfas, and R. S. Abhari (2008). Control of rotor tip leakage through cooling injection from the casing in a high-work turbine. *Journal of Turbomachinery*, 130(3).

Biesinger, T. E. (1993). *Secondary flow reduction techniques in linear turbine cascades*. Ph.D. thesis, Durham University.

Blair, M., An experimental study of heat transfer and film cooling on large-scale turbine endwalls. *In Turbo Expo: Power for Land, Sea, and Air* volume 79788. American Society of Mechanical Engineers, 1974.

Boyle, R. and J. Haas, Comparison of experimental and analytic performance for contoured endwall stators. *In 18th Joint Propulsion Conference, Cleveland,OH,U.S.A, 21-23 June*. 1982.

Brear, M. J., H. P. Hodson, P. Gonzalez, and N. W. Harvey (2002). Pressure surface separations in low-pressure turbinespart 2: Interactions with the secondary flow. *Journal of Turbomachinery*, 124(3), 402–409.

Brennan, G., N. Harvey, M. Rose, N. Fomison, and M. Taylor, Improving the efficiency of the trent 500 hp turbine using non-axisymmetric end walls: Part 1: Turbine design. *In Turbo Expo: Power for Land, Sea, and Air* volume 78507. American Society of Mechanical Engineers, 2001.

Burd, S. W. and T. W. Simon, Effects of slot bleed injection over a contoured endwall on nozzle guide vane cooling performance: Part i: Flow field measurements. *In ASME Turbo Expo 2000: Power for Land, Sea, and Air*. American Society of Mechanical Engineers, 2000.

Camci, C. and D. H. Rizzo (2002). Secondary flow and forced convection heat transfer near endwall boundary layer fences in a 90 turning duct. *International Journal of Heat and Mass Transfer*, 45(4), 831–843.

Chen, P., M. Alqefl, X. Li, J. Ren, H. Jiang, and T. Simon (2019). Cooling effectiveness and aerodynamic performance in a 2d-contoured endwall passage with different mass flow ratios. *International Journal of Thermal Sciences*, 142, 233–246.

Chen, P., L. Wang, X. Li, J. Ren, and H. Jiang (2020). Effect of axial turbine non-axisymmetric endwall contouring on film cooling at different locations. *International Journal of Heat and Mass Transfer*, 147, 118995.

Choi, S. M., J. S. Park, H. Chung, S. Park, and H. H. Cho (2017). Upstream wake effect on flow and heat transfer characteristics at an endwall of first-stage blade of a gas turbine. *Experimental Thermal and Fluid Science*, 86, 23–36.

Christophel, J., E. Couch, K. A. Thole, and F. Cunha (2005). Measured adiabatic effectiveness and heat transfer for blowing from the tip of a turbine blade. *Journal of Turbomachinery*, 127(2), 251–262.

Chung, J. and T. Simon, Effectiveness of the gas turbine endwall fences in secondary flow control at elevated freestream turbulence levels. *In Turbo Expo: Power for Land, Sea, and Air*volume78880. American Society of Mechanical Engineers, 1993.

Chung, J., T. W. Simon, and J. Buddhavarapu, Three-dimensional flow near the blade/endwall junction of a gas turbine: application of a boundary layer fence. *In Turbo Expo: Power for Land, Sea, and Air*volume79016. American Society of Mechanical Engineers, 1991.

Cui, J. and P. Tucker (2017). Numerical study of purge and secondary flows in a low-pressure turbine. *Journal of Turbomachinery*, 139(2), 021007.

Davis, R., T. Shang, J. Buteau, and R.-H. Ni, Prediction of 3-d unsteady flow in multistage turbomachinery using an implicit dual time-step approach. *In 32nd Joint Propulsion Conference and Exhibit, Lake Buena Vista,FL,U.S.A, 01-03 July*. 1996.

Deich, M., G. Filippov, and L. Y. Lazarev (1965). Atlas of axial turbine blade characteristics. *Part I: Method of profiling and the aerodynamic characteristics of cascades. Moskow, Mashinostroenie Publishing House*.

Denton, J. and L. Xu (1999). Exploitation of 3d flow in turbomachinery. *Turbomachinery Blade Design Systems , VKI Lecture Series*, 2.

DIppolito, G., V. Dossena, and A. Mora (2011). The influence of blade lean on straight and annular turbine cascade flow field. *Journal of Turbomachinery*, 133(1).

Dixon, J. A., A. G. Valencia, D. Coren, D. Eastwood, and C. Long, Main annulus gas path interactions: turbine stator well heat transfer. *In ASME Turbo Expo 2012: Turbine Technical Conference and Exposition*. American Society of Mechanical Engineers, 2012.

Dunn, D. I., G. C. Snedden, and T. Von Backström, Turbulence model comparisons for a low pressure 1.5 stage test turbine. *In 19th Air Breathing Engines International Symposium*. 2009.

Eric Lyall, M., P. I. King, J. P. Clark, and R. Sondergaard (2014). Endwall loss reduction of high lift low pressure turbine airfoils using profile contouringpart i: Airfoil design. *Journal of Turbomachinery*, 136(8).

Gao, Z., D. Narzary, and J.-C. Han (2009). Turbine blade platform film cooling with typical stator-rotor purge flow and discrete-hole film cooling. *Journal of Turbomachinery*, 131(4), 041004.

Georgiou, D. P. and K. F. Milidonis (2014). Fabrication and calibration of a sub-miniature 5-hole probe with embedded pressure sensors for use in extremely confined and complex flow areas in turbomachinery research facilities. *Flow Measurement and Instrumentation*, 39, 54–63.

Germain, T., M. Nagel, I. Raab, P. Schüpbach, R. Abhari, and M. Rose, Improving efficiency of a high work turbine using non-axisymmetric endwalls: Part i: Endwall design and performance. *In Turbo Expo: Power for Land, Sea, and Air*volume43161. 2008.

Giovannini, M., F. Rubechini, M. Marconcini, A. Arnone, and F. Bertini (2019). Reducing secondary flow losses in low-pressure turbines: The snaked blade. *International Journal of Turbomachinery, Propulsion and Power*, 4(3), 28.

Goldstein, R. and R. Spores (1988). Turbulent transport on the endwall in the region between adjacent turbine blades. *Journal of Heat Transfer*, 110(4a), 862–869.

Govardhan, M. and P. K. Maharia (2012). Improvement of turbine performance by streamwise boundary layer fences. *Journal of Applied Fluid Mechanics*, 5(3), 113–118.

Gregory-Smith, D., C. Graves, and J. Walsh (1988). Growth of secondary losses and vorticity in an axial turbine cascade. *Journal of Turbomachinery*, 110(1), 1–8.

Gregory-Smith, D., G. Ingram, P. Jayaraman, N. Harvey, and M. Rose (2001). Non-axisymmetric turbine end wall profiling. *Proceedings of the Institution of Mechanical Engineers, Part A: Journal of Power and Energy*, 215(6), 721–734.

Gündogdu, M. Y. and M. Ö. Çarpinlioglu (1998). A multi-tube pressure probe calibration method for measurements of mean flow parameters in swirling flows. *Flow Measurement and Instrumentation*, 9(4), 243–248.

Hamik, M. and R. Willinger (2007). An innovative passive tip-leakage control method for axial turbines: Basic concept and performance potential. *Journal of Thermal Science*, 16(3), 215–222.

Hammer, F., N. D. Sandham, and R. D. Sandberg (2018). The influence of different wake profiles on losses in a low pressure turbine cascade. *International Journal of Turbomachinery, Propulsion and Power*, 3(2), 10.

Han, W.-j., Q.-h. YANG, H.-y. HUANG, and J. Lin (2002). Topology and vortex structures of turbine cascade with different tip clearances. *Chinese Journal of Aeronautics*, 15(1), 18–26.

Han, X., W. Zeng, and Z. Han (2019). Investigation of the comprehensive performance of turbine stator cascades with heating endwall fences. *Energy*, 174, 1188–1199.

Harrison, S., The influence of blade lean on turbine losses. *In Turbo Expo: Power for Land, Sea, and Air* volume 79047. American Society of Mechanical Engineers, 1990.

Harrison, S. (1992). The influence of blade lean on turbine losses. *Journal of Turbomachinery*, 114(1), 184–190.

Hartland, J. and D. Gregory-Smith, A design method for the profiling of end walls in turbines. *In Turbo Expo: Power for Land, Sea, and Air* volume 3610. 2002.

Hartland, J., D. Gregory-Smith, N. Harvey, and M. Rose (2000). Nonaxisymmetric turbine end wall design: part ii: Experimental validation. *Journal of Turbomachinery*, 122(2), 286–293.

Hartland, J., D. Gregory-Smith, and M. Rose, *Non-axisymmetric endwall profiling in a turbine rotor blade* volume 78620. American Society of Mechanical Engineers, 1998.

Harvey, N., G. Brennan, D. Newman, and M. Rose, Improving turbine efficiency using non-axisymmetric end walls: Validation in the multi-row environment and with low aspect ratio blading. *In Turbo Expo: Power for Land, Sea, and Air* volume 3610. 2002.

Harvey, N. W., M. G. Rose, M. D. Taylor, S. Shahpar, J. Hartland, and D. G. Gregory-Smith (2000). Nonaxisymmetric turbine end wall design: part i: Three-dimensional linear design system. *Journal of Turbomachinery*, 122(2), 278–285.

Hennecke, D. K. and K. Wörrlein (2000). Flugantriebe und gasturbinen. *Skriptum der Technischen Universität Darmstadt, Fachgebiet Gasturbinen und Flugantriebe*, 2.

Hwang, S., C. Son, D. Seo, D.-H. Rhee, and B. Cha (2016). Comparative study on steady and unsteady conjugate heat transfer analysis of a high pressure turbine blade. *Applied Thermal Engineering*, 99, 765–775.

Ingram, G. (2003). Experimental quantification of the benefits of end-wall profiling in a turbine cascade. *16th International Symposium on Air Breathing Engines : August 31 - September 5, Renaissance Cleveland Hotel, Cleveland, Ohio, USA.*.

Ingram, G., D. Gregory-Smith, and N. Harvey (2005). Investigation of a novel secondary flow feature in a turbine cascade with end wall profiling. *Journal of Turbomachinery*, 127(1), 209–214.

Ingram, G., D. Gregory-Smith, M. Rose, N. Harvey, and G. Brennan, The effect of endwall profiling on secondary flow and loss development in a turbine cascade. *In Turbo Expo: Power for Land, Sea, and Air* volume 3610. 2002.

Ingram, G. L., *Endwall profiling for the reduction of secondary flow in turbines*. University of Durham UK, 2004.

Jenny, P., R. Abhari, M. Rose, M. Brettschneider, and J. Gier (2012). A low pressure turbine with profiled endwalls and purge flow operating with a pressure side bubble. *Journal of Turbomachinery*, 134(6), 061038.

Jenny, P., R. S. Abhari, M. G. Rose, M. Brettschneider, and J. Gier, A low pressure turbine with profiled end walls and purge flow operating with a pressure side bubble. *In Turbo Expo: Power for Land, Sea, and Air* volume 54679. 2011.

Kawai, T. (1994). Effect of combined boundary layer fences on turbine secondary flow and losses. *International Journal Series B Fluids and Thermal Engineering*, 37(2), 377–384.

Kiran, K. and S. Anish (2017). An investigation on the effect of pitchwise endwall design in a turbine cascade at different incidence angles. *Aerospace Science and Technology*, 71, 382–391.

Knezevici, D., S. Sjolander, T. Praisner, E. Allen-Bradley, and E. Grover (2010). Measurements of secondary losses in a turbine cascade with the implementation of nonaxisymmetric endwall contouring. *Journal of Turbomachinery*, 132(1).

Kopper, F., R. Milano, and M. Vanco (1981). Experimental investigation of endwall profiling in a turbine vane cascade. *American Institute of Aeronautics and Astronautics*, 19(8), 1033–1040.

Langston, L. (2001). Secondary flows in axial turbines: A review. *Annals of the New York Academy of Sciences*, 934(1), 11–26.

Li, W., W.-Y. Qiao, K.-F. Xu, and H.-L. Luo, Numerical simulation of tip clearance control in axial turbine rotor: part 2: Passive control of five different tip platforms. *In Turbo Expo: Power for Land, Sea, and Air* volume 43161. 2008.

Li, Y., X. Su, and X. Yuan (2019). The effect of mismatching between combustor and hp vanes on the aerodynamics and heat load in a 1-1/2 stages turbine. *Aerospace Science and Technology*, 86, 78–92.

Ligrani, P., G. Potts, and A. Fatemi (2017). Endwall aerodynamic losses from turbine components within gas turbine engines. *Propulsion and Power Research*, 6(1), 1–14.

Ligrani, P., B. Singer, and L. Baun (1989). Miniature five-hole pressure probe for measurement of three mean velocity components in low-speed flows. *Journal of Physics E: Scientific Instruments*, 22(10), 868.

Lynch, S. P., K. A. Thole, A. Kohli, and C. Lehane (2011). Computational predictions of heat transfer and film-cooling for a turbine blade with nonaxisymmetric endwall contouring. *Journal of Turbomachinery*, 133(4).

Mahmood, G., R. Gustafson, and S. Acharya (2005). Experimental investigation of flow structure and nusselt number in a low-speed linear blade passage with and without leading-edge fillets. *Journal of Heat Transfer*, 127(5), 499–512.

Mank, S., L. Duerrwaechter, M. Hilfer, R. Williams, S. Hogg, and G. Ingram, Secondary flows and fillet radii in a linear turbine cascade. *In ASME Turbo Expo 2014: Turbine Technical Conference and Exposition*. American Society of Mechanical Engineers, 2014.

Marini, R. and S. Girgis, The effect of blade leading edge platform shape on upstream disk cavity to mainstream flow interaction of a high-pressure turbine stage. *In Turbo Expo: Power for Land, Sea, and Air* volume 47950. 2007.

McLean, C., C. Camci, and B. Glezer (2001). Mainstream aerodynamic effects due to wheelspace coolant injection in a high-pressure turbine stage: Part : Aerodynamic measurements in the stationary frame. *Journal of Turbomachinery*, 123(4), 687–696.

Mehendale, A. B., J.-C. Han, S. Ou, and C. P. Lee (1994). Unsteady wake over a linear turbine blade cascade with air and co2 film injection: Part ii: Effect on film effectiveness and heat transfer distributions. *Journal of Turbomachinery*, 116(4), 730–737.

Mensch, A. and K. A. Thole (2014). Overall effectiveness of a blade endwall with jet impingement and film cooling. *Journal of Engineering for Gas Turbines and Power*, 136(3).

Mensch, A. and K. A. Thole (2016). Overall effectiveness and flowfield measurements for an endwall with nonaxisymmetric contouring. *Journal of Turbomachinery*, 138(3).

Menter, F. R. (1994). Two-equation eddy-viscosity turbulence models for engineering applications. *American Institute of Aeronautics and Astronautics*, 32(8), 1598–1605.

Mhetras, S. and J.-C. Han, Effect of unsteady wake on full coverage film-cooling effectiveness for a gas turbine blade. *In 9th AIAA/ASME Joint Thermophysics and Heat Transfer Conference*. 2006.

Moon, Y. J. and S.-R. Koh (2001). Counter-rotating streamwise vortex formation in the turbine cascade with endwall fence. *Computers & Fluids*, 30(4), 473–490.

Morris, A. and R. Hoare, Secondary loss measurements in a cascade of turbine blades with meridional wall profiling. *In American Society of Mechanical Engineers, Winter Annual Meeting, Houston, Tex.* 1975.

Moustapha, S. and R. Williamson (1986). Effect of two endwall contours on the performance of an annular nozzle cascade. *American Institute of Aeronautics and Astronautics*, 24(9), 1524–1530.

Nagel, M. G. and R.-D. Baier, Experimentally verified numerical optimisation of a 3d-parametrized turbine vane with non-axisymmetric end walls. *In Turbo Expo: Power for Land, Sea, and Air*volume36894. 2003.

Ni, R.-H. (1982). A multiple-grid scheme for solving the euler equations. *American Institute of Aeronautics and Astronautics*, 20(11), 1565–1571.

NI, R.-H. and J. BOGOIAN, Prediction of 3d multi-stage turbine flow field using a multiple-grid euler solver. *In 27th Aerospace Sciences Meeting*. 1989.

Niewoehner, J., T. Poehler, P. Jeschke, and Y. Guendogdu (2015). Investigation of nonaxisymmetric endwall contouring and three-dimensional airfoil design in a 1.5 stage axial turbinepart ii: Experimental validation. *Journal of Turbomachinery*, 137(8).

Nowack, C. (1970). Improved calibration method for a five-hole spherical pitot probe. *Journal of Physics E: Scientific Instruments*, 3(1), 21.

Obaida, H., A. Rona, and J. P. Gostelow (2019). Loss reduction in a 1.5 stage axial turbine by computer-driven stator hub contouring. *Journal of Turbomachinery*, 141(6).

Okita, Y. and C. Nakamata, Computational predictions of endwall film cooling for a turbine nozzle vane with an asymmetric contoured passage. *In Turbo Expo: Power for Land, Sea, and Air*volume43147. 2008.

Ostowari, C. and W. Wentz (1983). Modified calibration technique of a five-hole probe for high flow angles. *Experiments in Fluids*, 1(3), 166–166.

Ou, S., J.-C. Han, A. B. Mehendale, and C. P. Lee (1994). Unsteady wake over a linear turbine blade cascade with air and co2 film injection: Part i: Effect on heat transfer coefficients. *Journal of Turbomachinery*, 116(4), 721–729.

Panchal, K. V., S. Abraham, S. V. Ekkad, W. Ng, A. S. Lohaus, and M. E. Crawford, Effect of endwall contouring on a transonic turbine blade passage: Part 2: Heat transfer performance. *In Turbo Expo: Power for Land, Sea, and Air*volume44700. American Society of Mechanical Engineers, 2012.

Paniagua, G., R. Denos, and S. Almeida (2004). Effect of the hub endwall cavity flow on the flow-field of a transonic high-pressure turbine. *Journal of Turbomachinery*, 126(4), 578–586.

Papa, F., U. Madanan, and R. J. Goldstein (2017). Modeling and measurements of heat/mass transfer in a linear turbine cascade. *Journal of Turbomachinery*, 139(9).

Papa, M., V. Srinivasan, and R. Goldstein (2012). Film cooling effect of rotor-stator purge flow on endwall heat/mass transfer. *Journal of Turbomachinery*, 134(4), 041014.

Park, J. S., E. Y. Jung, D. H. Lee, K. M. Kim, B. S. Kim, B. M. Chang, *et al.* (2014). Effects of unsteady wake on heat transfer of endwall surface in linear cascade. *Journal of Heat Transfer*, 136(6).

Pisasale, A. and N. Ahmed (2002). A novel method for extending the calibration range of five-hole probe for highly three-dimensional flows. *Flow Measurement and Instrumentation*, 13(1-2), 23–30.

Poehler, T., J. Niewoehner, P. Jeschke, and Y. Guendogdu (2015). Investigation of non-axisymmetric endwall contouring and three-dimensional airfoil design in a 1.5-stage axial turbinepart i: Design and novel numerical analysis method. *Journal of Turbomachinery*, 137(8).

Praisner, T., E. Allen-Bradley, E. Grover, D. Knezevici, and S. Sjolander, Application of non-axisymmetric endwall contouring to conventional and high-lift turbine airfoils. *In Turbo Expo: Power for Land, Sea, and Air* volume47950. 2007.

Qi, L., Z. Zou, P. Wang, T. Cao, and H. Liu (2012). Control of secondary flow loss in turbine cascade by streamwise vortex. *Computers & Fluids*, 54, 45–55.

Qu, X., Y. Zhang, X. Lu, Z. Lei, and J. Zhu (2019). Effect of periodic wakes and a contoured endwall on secondary flow in a high-lift low-pressure turbine cascade at low reynolds numbers. *Computers & Fluids*, 190, 1–14.

Regina, K., A. Kalfas, and R. Abhari (2015). Experimental investigation of purge flow effects on a high pressure turbine stage. *Journal of Turbomachinery*, 137(4), 041006.

Reichert, B. A. and B. J. Wendt (1994). A new algorithm for five-hole probe calibration, data reduction, and uncertainty analysis. *NASA Technical Memorandum 106458*.

Reid, K., J. Denton, G. Pullan, E. Curtis, and J. Longley, The effect of stator-rotor hub sealing flow on the mainstream aerodynamics of a turbine. *In ASME Turbo Expo 2006: Power for Land, Sea, and Air*. American Society of Mechanical Engineers, 2006.

Rezasoltani, M., M. Schobeiri, and J. Han (2014). Experimental investigation of the effect of purge flow on film cooling effectiveness on a rotating turbine with nonaxisymmetric end wall contouring. *Journal of Turbomachinery*, 136(9).

Rose, M., N. Harvey, P. Seaman, D. Newman, and D. McManus, Improving the efficiency of the trent 500 hp turbine using non-axisymmetric end walls: Part ii: Experimental validation. *In Turbo Expo: Power for Land, Sea, and Air* volume78507. American Society of Mechanical Engineers, 2001.

Rose, M. G., Non-axisymmetric endwall profiling in the hp ngvs of an axial flow gas turbine. *In Turbo Expo: Power for Land, Sea, and Air*volume78835. American Society of Mechanical Engineers, 1994.

Roy, A. (2014). *Experimental Study of Gas Turbine Endwall Cooling with Endwall Contouring under Transonic Conditions*. Ph.D. thesis, Virginia Tech.

Roy, R., K. Squires, M. Gerendas, S. Song, W. Howe, and A. Ansari, Flow and heat transfer at the hub endwall of inlet vane passagesexperiments and simulations. *In ASME Turbo Expo 2000: Power for Land, Sea, and Air*. American Society of Mechanical Engineers, 2000.

Rozati, A. and D. K. Tafti, Large eddy simulation of leading edge film cooling: Part ii: Heat transfer and effect of blowing ratio. *In Turbo Expo: Power for Land, Sea, and Air*volume47934. 2007.

Saha, A. K. and S. Acharya (2008). Computations of turbulent flow and heat transfer through a three-dimensional nonaxisymmetric blade passage. *Journal of Turbomachinery*, 130(3).

Sangan, C. M., J. A. Scobie, J. M. Owen, G. D. Lock, K. M. Tham, and V. P. Laurello (2014). Performance of a finned turbine rim seal. *Journal of Turbomachinery*, 136(11), 111008.

Sangston, K., J. Little, M. Eric Lyall, and R. Sondergaard (2017). Effect of blade profile contouring on endwall flow structure in a high-lift low-pressure turbine cascade. *Journal of Turbomachinery*, 139(2).

Sauer, H., R. Mu¨ ller, and K. Vogeler (2001). Reduction of secondary flow losses in turbine cascades by leading edge modifications at the endwall. *Journal of Turbomachinery*, 123(2), 207–213.

Schneider, C., D. Schrack, M. Kuerner, M. Rose, S. Staudacher, Y. Guendogdu, and U. Freygang (2014). On the unsteady formation of secondary flow inside a rotating turbine blade passage. *Journal of Turbomachinery*, 136(6).

Schobeiri, M., K. Lu, and M. Rezasoltani (2015). Effect of non-axisymmetric contouring on performance and film cooling of a rotating turbine endwall subjected to the secondary air purge: A combined numerical and experimental study. *Proceedings of the Institution of Mechanical Engineers, Part A: Journal of Power and Energy*, 229(8), 813–831.

Schrewe, S., H. Werschnik, and H.-P. Schiffer (2013). Experimental analysis of the interaction between rim seal and main annulus flow in a low pressure two stage axial turbine. *Journal of turbomachinery*, 135(5).

Schuepbach, P., R. Abhari, M. Rose, T. Germain, I. Raab, and J. Gier (2010). Effects of suction and injection purge-flow on the secondary flow structures of a high-work turbine. *Journal of Turbomachinery*, 132(2), 021021.

Schuepbach, P., M. Rose, J. Gier, I. Raab, T. Germain, and R. S. Abhari, Non-axisymmetric end wall profiles including fillet radii, in a 1.5 stage axial flow turbine. *In 8th European Conference on Turbomachinery: Fluid Dynamics and Thermodynamics 23-27 March 2009, Graz-Austria.* Verl. der Techn. Univ. Graz, 2009.

Schüpbach, P., R. Abhari, M. Rose, T. Germain, I. Raab, and J. Gier, Improving efficiency of a high work turbine using non-axisymmetric endwalls: Part ii: Time-resolved flow physics. *In Turbo Expo: Power for Land, Sea, and Air* volume43161. 2008.

Schüpbach, P., R. Abhari, M. Rose, and J. Gier (2011). Influence of rim seal purge flow on the performance of an endwall-profiled axial turbine. *Journal of Turbomachinery*, 133(2), 021011.

Sharma, O. and T. Butler (1987). Predictions of endwall losses and secondary flows in axial flow turbine cascades. *Journal of Turbomachinery*, 109(2), 229–236.

Sieverding, C. (1985). Recent progress in the understanding of basic aspects of secondary flows in turbine blade passages. *Journal of Engineering for Gas Turbines and Power*, 107(2), 248–257.

Song, L., P. Zhu, J. Li, and Z. Feng (2017). Effect of purge flow on endwall flow and heat transfer characteristics of a gas turbine blade. *Applied Thermal Engineering*, 110, 504–520.

Sturm, W., H. Scheugenpflug, and L. Fottner (1992). Performance improvements of compressor cascades by controlling the profile and sidewall boundary layers. *Journal of Turbomachinery*, 114(3), 477–486.

Suryanarayanan, A., B. Ozturk, M. Schobeiri, and J. Han (2010). Film-cooling effectiveness on a rotating turbine platform using pressure sensitive paint technique. *Journal of Turbomachinery*, 132(4).

Thole, K. (2006). Airfoil endwall heat transfer. *The Gas Turbine Handbook, National Energy Technology Laboratory, DOE, Morgantown, WV*.

Torre, D., R. Vázquez, E. de la Rosa Blanco, and H. P. Hodson (2011). A new alternative for reduction in secondary flows in low pressure turbines. *Journal of Turbomachinery*, 133(1).

Town, J. and C. Camci, Sub-miniature five-hole probe calibration using a time efficient pitch and yaw mechanism and accuracy improvements. *In Turbo Expo: Power for Land, Sea, and Air* volume54631. 2011.

Treaster, A., T. AL, and Y. AM (1979). The calibration and application of five-hole probes. *24th International Instrumentation Symposium Albuquerque May 1-5*, A79-17576 05-35, 255–266.

Turgut, O. z. H. and C. Camcı, A nonaxisymmetric endwall design methodology for turbine nozzle guide vanes and its computational fluid dynamics evaluation. *In ASME International Mechanical Engineering Congress and Exposition*volume54877. 2011.

Walsh, J. and D. Gregory-Smith, Inlet skew and the growth of secondary losses and vorticity in a turbine cascade. *In ASME 1989 International Gas Turbine and Aeroengine Congress and Exposition*. American Society of Mechanical Engineers, 1989.

Wang, H.-P., S. J. Olson, R. J. Goldstein, and E. R. Eckert, Flow visualization in a linear turbine cascade of high performance turbine blades. *In ASME 1995 International Gas Turbine and Aeroengine Congress and Exposition*. American Society of Mechanical Engineers, 1995.

Warner, R. and M. Tran, Recent developments to improve high-pressure and intermediate-pressure turbine efficiency. *In Institution of Mechanical Engineers Turbo Conference*. 1987.

Wright, L. M., S. A. Blake, and J.-C. Han (2008). Film cooling effectiveness distributions on a turbine blade cascade platform with stator-rotor purge and discrete film hole flows. *Journal of Turbomachinery*, 130(3), 031015.

Wright, L. M., S. A. Blake, D.-H. Rhee, and J.-C. Han (2009). Effect of upstream wake with vortex on turbine blade platform film cooling with simulated stator-rotor purge flow. *Journal of Turbomachinery*, 131(2), 021017.

Yan, J., D. Gregory-Smith, and P. Walker, Secondary flow reduction in a nozzle guide vane cascade by non-axisymmetric end-wall profiling. *In Turbo Expo: Power for Land, Sea, and Air*volume78583. American Society of Mechanical Engineers, 1999.

Zerobin, S., C. Aldrian, A. Peters, F. Heitmeir, and E. Göttlich (2018*a*). Aerodynamic performance of turbine center frames with purge flowspart ii: The influence of individual hub and tip purge flows. *Journal of Turbomachinery*, 140(6).

Zerobin, S., S. Bauinger, A. Marn, A. Peters, F. Heitmeir, and E. Göttlich, The unsteady flow field of a purged high pressure turbine based on mode detection. *In Turbo Expo: Power for Land, Sea, and Air*volume50817. American Society of Mechanical Engineers, 2017.

Zerobin, S., A. Peters, S. Bauinger, A. Bhadravati Ramesh, M. Steiner, F. Heitmeir, and E. Göttlich (2018*b*). Aerodynamic performance of turbine center frames with purge flowspart i: The influence of turbine purge flow rates. *Journal of Turbomachinery*, 140(6).

Zess, G. and K. A. Thole (2002). Computational design and experimental evaluation of using a leading edge fillet on a gas turbine vane. *Journal of Turbomachinery*, 124(2), 167–175.

Zhou, K. and C. Zhou (2018). Unsteady effects of vortex interaction on tip leakage vortex breakdown and its loss mechanism. *Aerospace Science and Technology*, 82, 363–371.

Zimmermann, T. W., O. Curkovic, M. Wirsum, A. Fowler, and K. Patel (2017). Comparison of two-dimensional and three-dimensional turbine airfoils in combination with nonaxisymmetric endwall contouring. *Journal of Turbomachinery*, 139(6).

PUBLICATIONS BASED ON THIS THESIS

Journal Papers

1. Babu, Sushanlal, and S. Anish. "Aerodynamic performance of profiled endwalls with upstream slot purge flow in a linear turbine cascade having pressure side separation." Physics of Fluids 33.1 (2021): 015119..

2. Sushanlal, Babu, and S. Anish. "Transient Analysis of Upstream Wake Inside Turbine Blade Passage with Purge Flow." Aerospace Science and Technology 98 (2020): 105654.

3. Babu, Sushanlal, et al. "Numerical Investigation on Effects of Profiled Endwall over Purge Flow in Linear Turbine Cascade." Recent Asian Research on Thermal and Fluid Sciences. Springer, Singapore, 2020. 161-172.

4. Babu, S., and S. Anish. "Computational Predictions of Velocity Ratio and Ejection Angle on Purge Flow in a Linear Turbine Cascade with Upstream Disturbance." Journal of Applied Fluid Mechanics 13.1 (2020).

5. Kiran, K. N., Babu Sushanlal, and S. Anish. "Computational Investigation on Secondary Flows in a Linear Turbine Cascade with Tapered Dual Fence." Journal of Mechanical Science and Technology 33.2 (2019): 903-912.

6. Babu, Sushanlal, and Surendran Anish. "An Aerothermal Investigation of Purge Flow Behaviour in a Linear Turbine Cascade with Upstream Wakes." Recent Patents on Mechanical Engineering 11.4 (2018): 340-348.

Conference Papers

1. Kiran K N, Sushanlal Babu, Deepak Narayanan and Anish S "Reduction of Secondary Flow Losses in a Linear Turbine Cascade by Variable End Wall Contouring- A CFD Study" Proceedings of the Asian Congress on Gas Turbines, 14-16 November 2016, Indian Institute of Technology Bombay, India.

2. Sushanlal Babu and Anish S "A Computational Investigation of Purge Flow in a Linear Turbine Cascade with Upstream Wakes" The Asian Symposium on Computational Heat Transfer & Fluid Flow, 10-13 December, 2017, Indian Institute of Technology Madras, India.

3. Sushanlal Babu, Tom J K and Anish S "Numerical Study on Interaction between Wake Secondary Flow and Purge Flow in a Linear Turbine Cascade" Proceedings of the 7th International and 45th National Conference on Fluid Mechanics and Fluid Power (FMFP) December 10-12, 2018, Indian Institute of Technology Bombay, Mumbai, India.

4. Sushanlal Babu and Anish S "Numerical Study on the Effect of Upstream Wake on Purge Flow in a Linear Turbine Cascade" Proceedings of the 14th International Symposium on Experimental Computational Aerothermodynamics of Internal Flows, 8-11 July 2019, Gdansk, Poland.

CURRICULUM VITAE

SUSHANLAL BABU
Thiruvathira 'Ushus', Mannanam P O
Ettumanoor, Kottayam, Kerala, India
Pin - 686561
Email: sushanlalbabume@gmail.com
Contact Details: +919496329871

PROFESSIONAL SUMMARY

To work in a healthy, innovative and challenging environment extracting the best out of me, which is conducive to learn and grow at professional as well as personal level thereby directing my future endeavors as an asset to the organization.

ACADEMIC RECORDS

- Doctoral Program: Turbomachinery, National Institute of Technology Karnataka, India, June, 2021 (CGPA 8).

- M.Tech: Thermal Engineering, College of Engineering Adoor, Kerala, India, 2014 (CGPA 9).

- B.Tech: Amrita Viswavidyapetham, Kollam, Kerala, India, 2010 (CGPA 7.6).

- Higher Secondary: St. Ephrems HSS Mannanam, Kottayam, Kerala, India, 2006 (80%).

- Holy Cross HSS, Thellakom, Kottayam, Kerala, India, 2004 (87.67%).

SKILLS

- AUTO CADD, ICEM CFD, CATIA, SOLIDWORKS

- ANSYS

- LATEX, ORIGIN Pro

- Proficient in Numerical Simulations (FVM)

WORKSHOP/PROGRAMS ATTENDED/ORGANISED

- Participated in short term course on "Windtunnel Design and Testing from a Practical Perspective" held on July 03 - 08, 2016, IIT, Kharagpur, India.

- Participated in short term course on "Inverse Heat Transfer" organised by Department of Mechanical Engineering, NITK, Surathkal, during November 7 - 11, 2016.

- Attended workshop on "Biofluid Dynamics and Bioheat Transfer held during 20th to 21st February 2017 at NITK, Surathkal, India.

- Attended workshop on "Recent Advances and Challenges in Solar Thermal Systems" held on 20th March 2017 at NITK, Surathkal, India.

- Attended workshop on "Hot Wire Anemometry: Fundamentals with Demonstration" held on 22nd March 2017 at NITK, Surathkal, India.